



UNIVERSIDAD DE CHILE  
FACULTAD DE CIENCIAS FÍSICAS Y MATEMÁTICAS  
DEPARTAMENTO DE CIENCIAS DE LA COMPUTACIÓN

ANALYSIS AND DEVELOPMENT OF MULTI-FRAME SUPER-RESOLUTION  
ALGORITHMS FOR ASTRONOMICAL IMAGES

TESIS PARA OPTAR AL GRADO DE  
MAGÍSTER EN CIENCIAS, MENCIÓN COMPUTACIÓN

MEMORIA PARA OPTAR AL TÍTULO DE INGENIERO CIVIL EN COMPUTACIÓN

FERNANDO IGNACIO CARO ARIAS

PROFESOR GUÍA:  
NANCY HITSCHFELD KAHLER  
PROFESOR CO-GUÍA:  
GUILLERMO CABRERA VIVES

MIEMBROS DE LA COMISIÓN:  
PABLO GUERRERO PÉREZ  
PATRICIO INOSTROZA FAJARDIN  
ANDREA RODRÍGUEZ TASTETS

Este trabajo ha sido parcialmente financiado por CONICYT-PCHA Magíster Nacional 2013-22131747 y por el Centro de Modelamiento Matemático (CMM) de la Universidad de Chile a través del Proyecto Basal PFB 03 de CONICYT

SANTIAGO DE CHILE

2016

# Resumen

En esta tesis se aborda el problema de analizar el rendimiento de cuatro algoritmos de super-resolución multi-imagen cuando éstos son usados para recuperar imágenes astronómicas de alta resolución. Super-resolución multi-imagen es el nombre dado a los procesos que usan un conjunto de imágenes de baja resolución de una misma escena para obtener una nueva imagen con mayor resolución espacial, además de menos desenfoque y ruido, que cualquiera de las imágenes utilizadas como input. Estos algoritmos funcionan mediante la minimización de una función de costo, donde un *prior* es incluido para regularizar el proceso de reconstrucción, usando para ello un procedimiento de optimización basado en el cálculo del gradiente. Cada uno de los cuatro algoritmos desarrollados corresponde a una de las cuatro posibles combinaciones entre dos priors (Laplaciano y gradiente) para la función de costo y dos mecanismos para calcular su gradiente (la expresión analítica de dicho gradiente y la aproximación de Zomet).

El principal objetivo de esta investigación consiste en estudiar el comportamiento del rendimiento de estos algoritmos en función de la Razón Señal-a-Ruido (SNR) de la imágenes de baja resolución empleadas como input en el proceso de reconstrucción. Para lograr este objetivo se requiere hacer uso de simulaciones, ya que se necesitan conjuntos de imágenes de baja resolución caracterizados por distintos valores de SNR para testear el funcionamiento de los cuatro algoritmos. Las imágenes simuladas fueron obtenidas usando dos herramientas de simulación, una basada en la replicación del proceso mediante el cual una imagen es adquirida por un dispositivo y que se conoce como Modelo de Observación de Imágenes (IOM), y otra basada en un enfoque de Monte Carlo y cuyo nombre es PhoSim.

Considerando un rango de siete valores de SNR, muestreados en intervalos regulares entre 1 y 100 con una escala logarítmica, y usando un grupo de 100 templates de alta-resolución, se generaron 700 conjuntos, compuesto cada uno por 10 imágenes simuladas de baja resolución, utilizando para ello las dos herramientas de simulación previamente mencionadas. Luego, cada uno de los cuatro algoritmos fue empleado para reconstruir una imagen de alta resolución usando cada uno de estos conjuntos como input. El experimento descrito se llevó a cabo en dos instancias, primero usando registro afín para alinear las imágenes de baja resolución contenidas en cada conjunto utilizado como input, y luego utilizando registro cuadrático para cumplir dicha tarea. El rendimiento de los algoritmos fue evaluado, luego de realizar estos experimentos, usando como métricas el Peak de la Razón Señal-a-Ruido (PSNR) y el  $\chi^2$  reducido.

De acuerdo a los resultados obtenidos, para cada uno de los algoritmos el PSNR aumenta a medida que la SNR crece, mientras que el  $\chi^2$  reducido se mantiene relativamente constante independientemente de la SNR. Los resultados correspondientes al PSNR sugieren que para valores pequeños de la SNR la aproximación de Zomet y el prior Laplaciano representan la

mejor opción, mientras que para valores altos de la SNR la expresión analítica del gradiente junto al prior gradiente son la mejor opción, aunque, en este caso, por un margen estrecho. La magnitud de la disminución de rendimiento que se observa cuando los parámetros de registro y desenfoque son estimados es mayor cuando se usa PhoSim que cuando se usa el IOM. La utilización de diferentes procedimientos de registro no implicó variaciones significativas en el rendimiento de los cuatro algoritmos de super-resolución multi-imagen.

# Abstract

In this thesis we address the problem of analyzing the performance of four multi-frame super-resolution algorithms when they are used to recover astronomical high-resolution images. Multi-frame super-resolution algorithm is the name given to any procedure that uses a set of low-resolution images of the same scene to obtain a new image with more spatial resolution, and also less blur and noise, than any of the low-resolution images used as input. These algorithms work by minimizing a cost function, where a prior term is included in order to regularize the reconstruction process, using a gradient-based procedure. Each one of the four developed algorithms corresponds to one of the four possible combinations between two prior terms (Laplacian and gradient) for the cost function and two mechanisms for computing its gradient (the analytical expression of such gradient and Zomet's approximation).

The main goal of this research consists in studying the behavior of the performance of these algorithms as function of the Signal-to-Noise Ratio (SNR) of the low-resolution images employed as input in the reconstruction process. To accomplish this goal, the use of simulations was required, since sets of low-resolution images characterized by different SNR values are needed to test the operation of the four algorithms. The simulated images were obtained using two simulations tools, one based on the replication of the process by which an image is acquired by a device and that is known as Image Observation Model (IOM), and other based on a Monte Carlo approach and that is known as PhoSim.

Considering a range of seven SNR values, sampled in regular intervals between 1 and 100 for a logarithmic scale, and using a group of 100 high-resolution templates, 700 sets made up of 10 simulated low-resolution images each were generated using the two previously mentioned simulation tools. Each one of the four algorithms was then employed to reconstruct a high-resolution image using each one of these sets as input. The described experiment was performed twice, first using affine registration for the alignment of the low-resolution images contained in each input set, and then using quadratic registration to accomplish such task. The performance of the algorithms was measured, after performing these experiments, using the Peak Signal-to-Noise Ratio (PSNR) and the reduced  $\chi^2$  as metrics.

According to the results obtained, for each one of the algorithms the PSNR increases as the SNR grows, while the reduced  $\chi^2$  remains relatively stable regardless of the SNR. The PSNR results suggest that, for small SNR values, Zomet's approximation and the Laplacian prior term are the best choice, while, for high SNR values, the analytical expression for computing the gradient and the gradient prior term are the best choice, in this case, by a narrow margin. The magnitude of the performance reduction observed when the registration and blur parameters are estimated is larger when PhoSim is used than when the IOM is employed. The usage of different registration procedures did not lead to significant variations in the performance of the four multi-frame super-resolution algorithms.

*A mi familia*

# Acknowledgements

First and foremost, I would like to express my most sincere gratitude to my advisors, Professors Nancy Hitschfeld and Guillermo Cabrera, for the continuous support and wise advice that they always provided me during the development of this thesis. I really could not have imagined working under the guidance of a better pair of advisors during all this time.

I am greatly thankful to Nancy for the invaluable aid and recommendations that she always gave me about the different methodological aspects related to the process of performing scientific research. I am also completely grateful to Guillermo, especially for his patience, support, good humor and willingness to help me with every problem and doubt. It is mostly because of him that I am involved in research, since he has always been encouraging me to find the answers of many interesting, diverse and challenging scientific questions.

I also wish to convey my appreciation to all the members of the revision committee of this thesis, that was composed by Professors Pablo Guerrero, Patricio Inostroza and Andrea Rodríguez. This work has been greatly improved and enriched with all the feedback that they kindly gave me.

Furthermore, I would like to express my gratitude to all the friends and colleagues with whom I had the chance to share and interact during all these years as a student at the University of Chile. Among all these people I am especially grateful to Francisca Concha, mainly for the fruitful discussions and the constructive criticisms that helped to improve this thesis.

Last but not least, I must mention that none of this would have been possible without the unwavering love, generous support and constant understanding of my family. They have always been my main source of inspiration and strength to overcome many difficulties and undertake new challenges.

Powered@NLHPC: This research/thesis was partially supported by the supercomputing infrastructure of the NLHPC (ECM-02)

# Contents

<b>List of Figures</b>	<b>ix</b>
<b>1 Introduction</b>	<b>1</b>
1.1 How is multi-frame super-resolution possible? . . . . .	2
1.2 Why super-resolution in astronomical images? . . . . .	3
1.3 Development of multi-frame super-resolution algorithms . . . . .	4
1.4 Thesis description . . . . .	6
1.4.1 Research problems and hypotheses . . . . .	6
1.4.2 Goals and objectives . . . . .	8
1.4.3 Methodology . . . . .	9
<b>2 Literature review</b>	<b>11</b>
2.1 Super-resolution methods . . . . .	12
2.1.1 Frequency domain methods . . . . .	12
2.1.2 Spatial domain methods . . . . .	13
2.1.3 Projection onto convex sets . . . . .	14
2.1.4 Formulations of the super-resolution problem . . . . .	15
2.1.5 Modern approaches towards multi-frame super-resolution . . . . .	16
2.2 Super-resolution techniques in astronomy . . . . .	17
2.2.1 Variable-pixel linear reconstruction . . . . .	17
2.2.2 Lucky imaging . . . . .	18
2.3 Image registration and super-resolution . . . . .	19
2.4 Super-resolution software . . . . .	20
<b>3 Super-resolution theory</b>	<b>22</b>
3.1 Image Observation Model (IOM) . . . . .	23
3.1.1 Mathematical formulation . . . . .	23
3.1.2 Parameters of the image observation model . . . . .	24
3.2 Probabilistic framework of super-resolution . . . . .	25
3.2.1 The <i>Maximum Likelihood</i> approach . . . . .	26
3.2.2 The <i>Maximum A Posteriori</i> approach . . . . .	27
3.3 Priors for MAP super-resolution . . . . .	28
3.3.1 Laplacian prior . . . . .	28
3.3.2 Gradient prior . . . . .	29
3.4 Optimization for MAP super-resolution . . . . .	29
3.4.1 Gradient for MAP cost function with Laplacian prior . . . . .	30

3.4.2	Gradient for MAP cost function with gradient prior . . . . .	30
3.4.3	Zomet’s method . . . . .	31
3.5	Image registration . . . . .	32
3.5.1	Registration using sum of squared differences . . . . .	33
3.5.2	Optimization of registration based on SSD . . . . .	33
3.5.3	Registration of affine transformations . . . . .	34
3.5.4	Registration of quadratic transformations . . . . .	35
<b>4</b>	<b>Astronomical images and super-resolution</b>	<b>36</b>
4.1	General description of astronomical images . . . . .	36
4.1.1	Acquisition of astronomical images . . . . .	37
4.1.2	Source characterization . . . . .	38
4.1.3	Noise sources in astronomical images . . . . .	39
4.1.4	Distortions . . . . .	39
4.2	Survey images . . . . .	41
4.3	Relevant characteristics in the context of multi-frame super-resolution . . . . .	41
4.3.1	Point-Spread Function (PSF) . . . . .	42
4.3.2	Signal-to-Noise Ratio (SNR) . . . . .	44
<b>5</b>	<b>Experimental setting</b>	<b>45</b>
5.1	Selected algorithms . . . . .	46
5.2	Image simulation . . . . .	47
5.2.1	Construction of the template set . . . . .	48
5.2.2	Simulations based in the image observation model . . . . .	48
5.2.3	PhoSim simulations . . . . .	49
5.3	Performance metrics . . . . .	50
5.3.1	Peak Signal-to-Noise Ratio (PSNR) . . . . .	50
5.3.2	Reduced $\chi^2$ . . . . .	51
5.4	Experimental frameworks . . . . .	52
5.4.1	First experimental framework (1EF) . . . . .	53
5.4.2	Second experimental framework (2EF) . . . . .	56
5.5	Relevant technical aspects . . . . .	61
5.5.1	Implementation of multi-frame super-resolution algorithms . . . . .	61
5.5.2	Implementation of image registration . . . . .	62
5.5.3	Implementation of the prior terms . . . . .	63
5.5.4	Utilization of the NLHPC’s cluster . . . . .	63
<b>6</b>	<b>Experimental results</b>	<b>65</b>
6.1	Results of the first experimental framework . . . . .	66
6.2	Results of the second experimental framework . . . . .	68
6.2.1	Case 1: PhoSim and affine registration . . . . .	68
6.2.2	Case 2: Image observation model and affine registration . . . . .	70
6.2.3	Case 3: Phosim and quadratic registration . . . . .	72
6.2.4	Case 4: Image observation model and quadratic registration . . . . .	74
6.3	Comparison between results of both frameworks . . . . .	76
6.3.1	Comparison between results of the 1EF and the case 1 of the 2EF . . . . .	77
6.3.2	Comparison between results of the 1EF and the case 2 of the 2EF . . . . .	78

6.3.3	Comparison between results of the 1EF and the case 3 of the 2EF . . .	79
6.3.4	Comparison between results of the 1EF and the case 4 of the 2EF . . .	80
6.4	Comparison between results of the second experimental framework . . . . .	81
6.4.1	Comparison of results with the same simulation scheme . . . . .	81
6.4.2	Comparison of results with the same registration procedure . . . . .	83
6.5	Examples of reconstructed images . . . . .	85
<b>7</b>	<b>Conclusions</b>	<b>91</b>
7.1	Relation between performance and SNR . . . . .	91
7.2	Best algorithms according to SNR values . . . . .	92
7.3	Performance reduction of the algorithms . . . . .	94
7.4	Influence of the registration procedures . . . . .	96
7.5	Future research directions . . . . .	97
7.5.1	Testing new parameters . . . . .	97
7.5.2	ML vs MAP . . . . .	98
7.5.3	Different registration methods . . . . .	98
7.5.4	Influence of optimization methods . . . . .	99
7.5.5	Influence of interpolation methods . . . . .	99
<b>A</b>	<b>Detailed results</b>	<b>100</b>
A.1	Detailed results of the 1EF . . . . .	101
A.2	Detailed results of the 2EF . . . . .	102
A.2.1	Case 1: PhoSim and affine registration . . . . .	102
A.2.2	Case 2: IOM and affine registration . . . . .	103
A.2.3	Case 3: Phosim and quadratic registration . . . . .	104
A.2.4	Case 4: IOM and quadratic registration . . . . .	105
A.3	Detailed results of the comparison between both frameworks . . . . .	106
A.3.1	Comparison between the 1EF and case 1 of the 2EF . . . . .	106
A.3.2	Comparison between the 1EF and case 2 of the 2EF . . . . .	107
A.3.3	Comparison between the 1EF and case 3 of the 2EF . . . . .	108
A.3.4	Comparison between the 1EF and case 4 of the 2EF . . . . .	109
	<b>Bibliography</b>	<b>110</b>

# List of Figures

1.1	Fundamental idea behind multi-frame super-resolution . . . . .	3
2.1	Operation of the variable-pixel linear reconstruction algorithm . . . . .	18
3.1	Image acquisition process . . . . .	23
4.1	CCD detector and its mechanism of operation . . . . .	37
4.2	Simulated example of a LSST survey image . . . . .	41
4.3	FWHM and standard deviation in a Gaussian function. . . . .	43
4.4	Examples of blur degradation for different FWHM values. . . . .	43
4.5	Examples of noise corruption for different SNR values. . . . .	44
5.1	Examples of template and simulated images . . . . .	50
5.2	Flow chart of the First Experimental Framework (1EF) . . . . .	54
5.3	Flow chart of the Second Experimental Framework (2EF) . . . . .	57
5.4	PhoSim image simulations of the observation of a point source . . . . .	59
6.1	Performance results obtained in the 1EF . . . . .	67
6.2	Performance results obtained in case 1 of the 2EF . . . . .	69
6.3	Performance results obtained in case 2 of the 2EF . . . . .	71
6.4	Performance results obtained in case 3 of the 2EF . . . . .	73
6.5	Performance results obtained in case 4 of the 2EF . . . . .	75
6.6	Comparison between results of the 1EF and case 1 of the 2EF . . . . .	77
6.7	Comparison between results of the 1EF and case 2 of the 2EF . . . . .	78
6.8	Comparison between results of the 1EF and case 3 of the 2EF . . . . .	79
6.9	Comparison between results of the 1EF and case 4 of the 2EF . . . . .	80
6.10	Comparison between results of cases 1 and 3 of the 2EF . . . . .	82
6.11	Comparison between results of cases 2 and 4 of the 2EF . . . . .	82
6.12	Comparison between results of cases 2 and 1 of the 2EF . . . . .	83
6.13	Comparison between results of cases 4 and 3 of the 2EF . . . . .	84
6.14	Examples of reconstructed images for a SNR value of 5.37 . . . . .	88
6.15	Examples of reconstructed images for a SNR value of 25.87 . . . . .	89
6.16	Examples of reconstructed images for a SNR value of 96.56 . . . . .	90

# Chapter 1

## Introduction

Multi-frame super-resolution is the name given to any image reconstruction technique whose aim is the generation of one or more high-quality images, using as input a set of noisy low-resolution images of the same scene, acquired under different conditions. These kind of techniques process together the set of low-resolution images in order to reconstruct images with higher resolution and less noise and blur than any of the input images.

The obtention of high-resolution images is usually desired, and even required, in many fields where the use of images is intensive. Medical imaging, microscopy, surveillance video, and remote sensing are classical examples of these fields. The most straightforward manner to obtain high-resolution images would be developing new sensors, with a larger number of pixels of smaller size. In many cases, though, this is not possible, mainly due to technical constraints. Multi-frame super-resolution algorithms provide a different approach for dealing with this limitation where, instead of improving the quality of the imaging devices, image processing techniques and computing power are the key elements.

In astronomy, the situation previously described also occurs. The nature of astronomical work requires the obtention of images with the largest possible resolution. However, due to technical and financial limitations, the construction of new telescopes with bigger mirrors is difficult, very slow, and very expensive. Therefore, the use of super-resolution techniques has a relevant impact by improving the quality of astronomical images using astronomical observations that are already available.

In this thesis we address the problem of analyzing the performance of four multi-frame super-resolution algorithms, when employed to obtain enhanced astronomical images. The performance of these four algorithms, developed considering the combination of two different image models and two different optimization mechanisms, was studied as a function of the quality degree of the astronomical images used as input. This quality degree is measured in terms of the relation between the amount of noise and the amount signal contained in such images.

In order to properly present the research conducted in this thesis and provide the context required to fully understand its scope, in the following sections we discuss the basics behind

multi-frame super-resolution operation, the main motivations for studying the performance of these algorithms considering astronomical images, how we developed the four analyzed algorithms, and finally a description of the work presented in this thesis. The purpose of this description is to present all the elements required to specify the research carried out on this thesis in an adequate manner, such as the hypotheses, the goals or the methodology, among others.

## 1.1 How is multi-frame super-resolution possible?

The reconstruction of high-resolution images using super-resolution techniques is based on the following idea: since each low-resolution image of a common scene is essentially a different degraded version of that scene, due mainly to the motion differences with sub-pixel precision that exist between these low-resolution images, the complementary information contained in each image can be combined in order to generate a new image with higher resolution than any of the originals [48]. The presence of these sub-pixel motion differences is a consequence of controlled and/or uncontrolled displacements between the imaging system and the scene. A simplified diagram describing this fundamental premise of multi-frame super-resolution is presented in Figure 1.1.

From a physical perspective, each pixel in a low-resolution image can be considered as the integral of a group of pixels of the high-resolution image. This means that each low-resolution pixel is the result of a weighted sum of high-resolution pixels, where the scope of the sum is defined in terms of the size relation and the relative positions between the low-resolution and high-resolution pixels, while the weight of each high-resolution pixel is determined by the *Point-Spread Function*<sup>1</sup>(PSF) of the imaging system. From a mathematical perspective, the relation between a low-resolution pixel and its associated high-resolution pixel provides a constraint that can be used to recover the high-resolution image. Due to the presence of the sub-pixel motions, and also to the blur differences between low-resolution images, the total set of constraints will not be redundant and image recovery will be possible to a certain extent. With a larger number of low-resolution images the number of constraints will be increased, yielding an improvement in the quality of the reconstructed high-resolution image.

There is a relevant aspect that arises from this fundamental idea behind the operation of multi-frame super-resolution, which is the critical requirement of estimating, in the most precise way possible, the motion differences between low-resolution images in order to obtain an accurate reconstruction of the high-resolution image. This entails that *registration*, the name given to the process by which these motion differences are computed, represents a critical previous step for multi-frame super-resolution. Thus, the precision reached by the registration process affects the performance achieved by multi-frame super-resolution algorithms, since the quality of the reconstructed high-resolution image will be greater if the degree of error introduced by the registration procedure is small.

Two different registration procedures are reviewed in further chapters. The first one,

---

<sup>1</sup>The *Point-Spread Function* is the function that models the degree of blur contained in the image generated by an imaging system when a point source is observed.

known as *affine registration*, computes the motions that differentiate the low-resolution images by performing an optimization over the parameters of a set of affine transformations that are employed for maximizing (minimizing) a similarity (dissimilarity) measure which is calculated for these images, using one of them as a common reference for all the rest. The second registration procedure, known as *quadratic registration*, operates exactly in the same manner but using quadratic instead of affine transformations. This last registration mechanism is more sophisticated than the first one, since each quadratic transformation is defined by 12 coefficients, while affine transformations are defined using only 6 coefficients. Therefore, the motion model employed by quadratic registration is wider and more flexible than the motion model employed by affine registration.

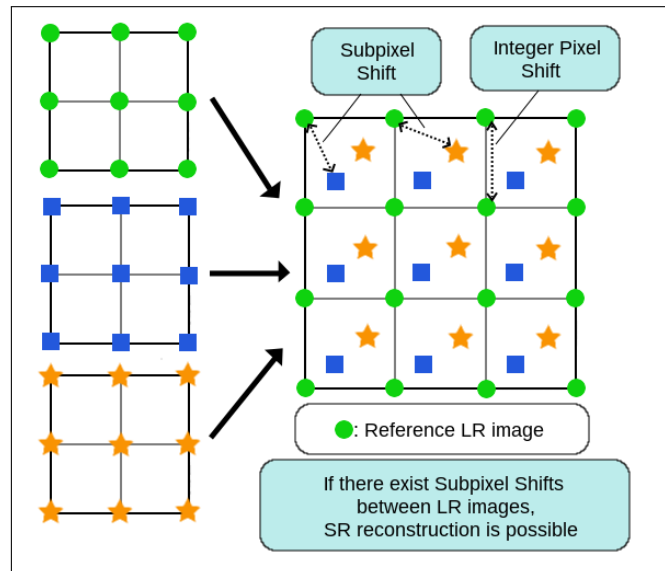


Figure 1.1: Fundamental idea that explains the mechanism used by multi-frame super-resolution algorithms to obtain a high-resolution image.

## 1.2 Why super-resolution in astronomical images?

In the last years, the classical approach in astronomy for observing the sky has changed dramatically. In the past, an astronomer would go to an observatory and use the telescope to observe a specific object of their interest. Now, this observation approach is being progressively replaced by a new system based on surveys. A survey is an automatic observation of different portions of the sky. In this new model, the telescopes of the survey observe different parts of the sky every night, which have been previously defined according to scientific considerations, and the images obtained in the process are immediately uploaded to online databases. These databases are then used by astronomers to gather the images and catalogs<sup>2</sup> required for their scientific tasks.

Some examples of this new trend in astronomical observations are the Sloan Digital Sky

<sup>2</sup>An astronomical catalog is a list of astronomical objects, typically grouped together because they share a common type, morphology, origin, means of detection, or method of discovery.

Survey (SDSS) [17], the Visible and Infrared Survey Telescope for Astronomy (VISTA) [63] and the Large Synoptic Survey Telescope (LSST) [35], a new telescope currently under construction, that is expected to be operational in the year 2022. Projections for LSST indicate that this telescope will take more than 800 panoramic images each night with its 3.2 billion-pixel camera, recording the entire visible sky twice a week. Each patch of sky it images will be observed 1000 times during the operation of this survey. With a light-gathering power equivalent to a 6.7-meter diameter primary mirror, each of its 30-seconds observations will be able to detect objects 10 million times fainter than visible with the human eye.

Multi-frame super-resolution algorithms have a great impact in any discipline where there is an intense utilization of images, as this kind of algorithms allow the obtention of enhanced images that can help to yield improved technical or scientific results. This explains the main motivation to analyze the performance of these algorithms when they are employed with astronomical images, since astronomy is probably the best example of this sort of fields with an intense usage of images and where multi-frame super-resolution techniques can be very useful. Therefore, with this performance analysis we can have an estimation of the degree of improvement associated to the usage of these algorithms for the case of astronomical images.

It is important to notice, considering the ideas exposed above, that the data generated by a survey corresponds to an enormous set of images that can be used to generate new enhanced images with multi-frame super-resolution algorithms. In fact, since there is always some extent of error in the procedure by which some sky portion is pointed by a telescope, the presence of motion differences between each one of the images generated by a survey, for a common sky portion, is something expected and that enables the usage of multi-frame super-resolution algorithms.

Besides, since surveys generate a huge amount of data, the utilization of multi-frame super-resolution algorithms with a large number of astronomical images represents also an appealing challenge from the perspective of big-data. For example, the LSST will be capable of capturing images of the same portion of the sky 1000 times during its operation, making it possible to generate high-resolution images using these 1000 images as the input for one or more multi-frame super-resolution procedures.

Another relevant reason for using multi-frame super-resolution as a tool for processing astronomical images is its flexibility for dealing with other classical problems that arise for this kind of images, such as deconvolution or denoising. Actually, these two problems are two specific cases of the super-resolution problem, which means that super-resolution represents a wide framework for image processing in the context of astronomical images.

### 1.3 Development of multi-frame super-resolution algorithms

Four multi-frame super-resolution algorithms were developed in this thesis in order to study their performances. The operation of these algorithms is based in the Bayesian approach known as *Maximum A Posteriori* (MAP), where the likelihood, which is the probability of

obtaining one reconstructed image in terms of the available data (that corresponds to the set of low-resolution images), is maximized according to an image model previously selected and which is employed to establish some characteristics that should be satisfied by the high-resolution image that is being reconstructed.

In practice, these algorithms obtain a high-resolution image by minimizing a cost function in several iterations. In each iteration this cost function is computed employing the high-resolution image estimate, then its gradient is calculated to improve the high-resolution image estimate and have a lower value for the cost function in the next iteration. Therefore, when the global minimum of the cost function is reached, the best possible image reconstruction is achieved.

The cost function used by each multi-frame super-resolution algorithm is defined by two elements: the first one is the data term, that corresponds to the sum of the differences between each low-resolution image available and the corresponding low-resolution version of the high-resolution image estimate. The second element is given by a prior term that represents the image model previously mentioned. This prior term corresponds to a penalization value computed for the high-resolution image estimate according to the characteristics imposed by the image model, such as smoothness or amplitude constraints.

The four multi-frame super-resolution algorithms were developed with the aim of dispose of useful tools for reconstructing astronomical high-resolution images. Therefore, their development supposed the combination of different tools whose purpose is to deal with the presence of noise in images, since this factor represents the main source of distortion in astronomical images. In fact, each one of these four algorithms corresponds to one of the four possible combinations between two different prior terms and two different gradient computation procedures.

The two prior terms employed in the development of these algorithms, which are known as *gradient* and *Laplacian* priors, introduce smoothness restrictions for the reconstructed image in order to impose the noise remotion during the cost function minimization. On the other hand, the two procedures selected for computing the gradient of the cost function correspond to the standard mechanism, which corresponds to the *analytical computation* of the gradient, and to *Zomet's approximation*, where the data term of the gradient (that corresponds to the derivative of the data term of the cost function) is estimated using a median operator. The purpose of this approximation is to have robustness against the noise presence in the gradient computation procedure.

After reviewing the theoretical aspects of multi-frame super-resolution, these four algorithms will be introduced with more detail. However, we present below the notation that will be employed in this thesis from now on to reference each one of these four multi-frame super-resolution algorithms that are our subject of study:

LA: Laplacian prior in the cost function and utilization of the analytical expression for computing the gradient.

LZ: Laplacian prior in the cost function and utilization of Zomet's approximation for computing the gradient.

GA: Gradient prior in the cost function and utilization of the analytical expression for

computing the gradient.

GZ: Gradient prior in the cost function and utilization of Zomet's approximation for computing the gradient.

## 1.4 Thesis description

In order to provide some context, we have introduced the basics behind multi-frame super-resolution operation as well as the main reasons that motivate the study of this kind of techniques when they are employed with astronomical images. Also, we have described how each one of the four multi-frame super-resolution algorithms, which are studied in this thesis, was developed by combining different tools. Now, using the information and concepts introduced so far, we present all the elements required for properly posing the research that is conducted in this thesis.

### 1.4.1 Research problems and hypotheses

The main aim of the research presented in this thesis is to understand how multi-frame super-resolution algorithms behave when they are employed for recovering a high-resolution image from a set of astronomical low-resolution images. Evidently, this problem is too general and not specific enough to actually be used as a research problem, since its scope is not properly limited and finding a clear answer would not be possible. However, the statement of this general problem is useful to have a first notion of the kind of questions that this work seeks to answer.

A more suitable research problem for structuring this thesis is given by understanding how the performance of each one of the four multi-frame super-resolution algorithms, which were previously introduced, is related to the *Signal-to-Noise Ratio* (SNR) value that describes the images used as input by these algorithms in the reconstruction process. This problem is substantially more concrete than the one presented above, since in this case we only expect to understand how the performance of four specific algorithms behaves as a function of a specific parameter that describes the set of images which are used as input by these algorithms.

For this problem we propose the following hypothesis: the performance of each one of the four multi-frame super-resolution algorithms (that is measured using two metrics which will be later introduced) is proportional to the SNR value, which means that the algorithms' performance improves as the SNR value grows. We expect this behavior because the SNR represents a quality measure for an astronomical image, as its value corresponds to the ratio between the amount of signal and the amount of noise contained in that image. Therefore, if we have an increase in the SNR value then we have an enhancement in the quality of the astronomical low-resolution images and, as a consequence of this situation, we can expect an improvement in the performance of the algorithms.

Another interesting research problem, that is fully related to the one already stated, is

discovering which one of the four multi-frame super-resolution algorithms has the best performance in terms of the SNR. For this research problem we only have a very limited hypothesis, which states that we can expect a better performance of LZ and GZ over LA and GA for small SNR values, and the inverse behavior for large SNR values. This is expected as a consequence of the employment of Zomet’s approximation in LZ and GZ, since this procedure offers a robust mechanism for computing the gradient in presence of noise. Therefore, we can expect a better performance of the algorithms that use this mechanism when a great amount of noise affects the image quality, situation that happens when small SNR values are considered. Moreover, since this mechanism computes the gradient of the cost function using an approximation, we can expect better results with the analytical expression, which is exact and not an approximation, when a low level of noise affects the images employed as input by the algorithms. Thus, LA and GA should have the best performance when large SNR values are considered, since this means that only an small amount of noise is corrupting the low-resolution images.

We can only offer this limited hypothesis because we do not have any notion about the behavior of the gradient and Laplacian prior terms, in the context of noise removal in astronomical images during the minimization of a cost function. Therefore, we are not able to provide an interpretation to compare the performances between algorithms that employ different prior terms.

In third place, we are interested in discovering if there is a significative reduction in the performance results achieved by each one of the algorithms when there are errors in the estimation of the different parameters required for performing super-resolution reconstruction, such as the registration information and the blur. For this research problem we pose as hypothesis that, actually, there is a reduction in the algorithms’ performance as consequence of the non-accurate values calculated for the different parameters required for super-resolution process, which means that the quality of the reconstructed high-resolution image is affected by these errors.

It is important to highlight two relevant points about this third research problem. First, for finding out if this performance reduction exists, we need to compare the performance results obtained by each algorithm when all the parameters required for multi-frame super-resolution are precisely known, with the results obtained when the parameter values are not accurate due to the presence of errors. In second place, we need to consider that the magnitude of this performance reduction, if it exists, will be strongly determined by the metric employed to measure the algorithms’ performance as well as by the mechanisms used for the estimation of the parameters.

The fourth and final research problem is related with a secondary, but still very relevant, input of these algorithms which corresponds to the registration information. The accurate estimation of the motions that differentiate the low-resolution images is crucial for obtaining an adequate reconstruction of the high-resolution image. There are multiple and diverse mechanisms for compute the registration parameters but, in this case, the idea behind this fourth research problem is to find out if the algorithms’ performance improves when the registration parameters are computed using quadratic registration instead of affine registration.

The expected answer for the question posed by this last research problem is positive,

meaning that we expect to find an improvement in the performance of the algorithms when the results obtained employing quadratic registration are compared with the results obtained using affine registration. The main reason to expect this comes from the usage of a more complex motion model in quadratic registration with respect to the one employed in affine registration, since we believe that this higher degree of complexity entails the obtention of more accurate results.

## 1.4.2 Goals and objectives

The goals of this thesis are related to finding the answers for the questions derived from the research problems previously stated. This means that we expect to achieve the following four goals with the work developed in this thesis:

- G1: To find out the relation between the performance results of the four multi-frame super-resolution algorithms and the SNR value that describes the images used as input.
- G2: To determine which one of these four algorithms has the best performance results as a function of the SNR value of the low-resolution images of the input set.
- G3: To analyze if the algorithms' performance decreases with the presence of errors in the values computed for the blur and registration parameters.
- G4: To check if the employment of quadratic registration, instead of affine registration, entails an improvement in the performance results of each one of these four algorithms.

The achievement of these four goals supposes the accomplishment of multiple objectives or specific goals. In most cases, the achievement of one of these objectives is a requirement needed to accomplish more than one goal, which basically means that many of these objectives are shared by different goals. Now we present a list of the main objectives whose achievement structured a great part of the work developed in this thesis:

- O1: To select a template set of astronomical images that can be used for obtaining simulated low-resolution images.
- O2: To simulate low-resolution images from astronomical images, employing them as templates, and considering adjustable values for the pixel size, the PSF, the SNR and the motions between images.
- O3: To implement the four multi-frame super-resolution algorithms whose performance we pretend to study.
- O4: To implement affine and quadratic registration.
- O5: To find and use a mechanism for estimating the PSF of an astronomical image.
- O6: To choose one or more metrics for measuring the performance of these four multi-frame super-resolution algorithms.
- O7: To test these algorithms and computing their performances using sets of simulated low-resolution images generated with predefined parameter values.

### 1.4.3 Methodology

The methodology employed in this thesis to achieve the four posed goals was an experimental one, which means that we performed a group of experiments with the aim of obtaining all the information required to answer the questions related with each one of these goals. This experimental methodology is based on the utilization of simulated astronomical images and the employment of two metrics for measuring the algorithm's performance. The description of this methodology can be confusing due to the close relation that exists between the goals, which entails that some experiments provide information that is useful for more than one goal.

In the multiple experiments conducted for this thesis, we generated different sets of astronomical images considering specific SNR values by using two different simulation schemes. The first simulation scheme is based in the utilization of the *Image Observation Model* (IOM), which is a mathematical representation of the degradation process that affects a high-resolution image and whose result is its corresponding low-resolution version. The second simulation scheme considers the utilization of *PhoSim*, a computational tool that allows the simulation of astronomical images using an approach based on Monte Carlo techniques for sampling photons according to a great number of physical parameters. By degrading each one of the images contained in a template set multiple times, employing the IOM and also PhoSim, we generated the different sets of low-resolution images required for the experiments and which were provided as input for the four multi-frame super-resolution algorithms.

To measure the performance of these algorithms we considered the *Peak Signal-to-Noise Ratio* (PSNR) and the *reduced  $\chi^2$*  as metrics. The first one compares the high-resolution image recovered, by each one of the four multi-frame super-resolution algorithms, with the template image used for simulating the input set provided to these algorithms. On the other hand, the reduced  $\chi^2$  assesses how well the recovered image reflects the information contained in the images used as input for the reconstruction process. With these two metrics, we are measuring the performance of the algorithms in two different and independent ways, since in each case the reconstructed image is compared with distinct elements. Therefore, if the same trend is detected in the results obtained from the experiments using both performance metrics, then we can expect that such trend actually exists and that is not biased by one of these metrics.

The experiments conducted in this thesis are organized in two experimental frameworks that represent different situations. In the *first experimental framework* (1EF), a wide range of SNR values was considered and all the simulation parameters that are required by the algorithms, such as the blur and the registration parameters, were considered known. Since in PhoSim all the parameters can not be explicitly controlled, due to the great complexity of the model and its random elements, we only used the IOM to simulate astronomical low-resolution images in the 1EF.

In the *second experimental framework* (2EF) all the parameters required by the algorithms were estimated and the simulated images were obtained using the IOM and PhoSim considering a common range of SNR values. In this framework, the PSF and the registration information represent all the parameters that need to be estimated. The PSF was estimated

using two astronomical tools developed for that purpose, which are known as *SExtractor* and *PSFEx*, while the registration parameters were estimated using affine and quadratic registration. The parameter values computed by the different mechanisms are never totally accurate, since none of these mechanisms is perfect and their operation is affected by noise and other perturbing elements.

Since we are considering two different simulation schemes, PhoSim and IOM, and two different registration approaches, affine and quadratic registration, we arranged the experiments of the 2EF in four cases. Each one of these cases represents one of the four possible combinations between the two options for simulating astronomical low-resolution images and the two options for performing image registration.

In summary, we have a total number of five experiments that were performed for for this thesis, where the first one is part of the 1EF and the four others are part of the 2EF. With the results obtained from all these experiments we were able to gather the information required to analyze the veracity of the hypotheses posed for the research questions. For example, with the results obtained in each experiment we obtained the information required for characterizing the performance of the four multi-frame super-resolution algorithms as function of the SNR, which allowed us to find answers for the first and the second research problems and achieving the two goals related to these questions. Also, by comparing the results obtained in both experimental frameworks, we were able of studying and measuring the variation in the algorithms' performance in order to achieve the third goal of this thesis. Also, using the results of the four cases of the 2EF, it was possible to analyze the effects associated to the employment of quadratic and affine registration accomplishing, then, the last and fourth goal.

# Chapter 2

## Literature review

Since the pioneering work of Tsai and Huang [71] in 1984, multi-frame super-resolution has been an active research field with an increasing interest through the years. This is closely related to the continuous increase of the available computing power during the last decades, which is the main resource required for employing multi-frame super-resolution techniques in order to obtain enhanced images.

This thesis focuses in multi-frame super-resolution, which is the name given to the techniques that generate one or more high-resolution images using a set of low-resolution images of the same input scene. This super-resolution approach is usually referred as *digital* or *geometrical super-resolution*, and should not be confused with the methods used for transcending the optical diffraction limit and that are grouped under the name of *optical super-resolution* [30, 81]. It is also important not to confuse multi-frame super-resolution with *single-frame super-resolution*, which is likewise used to increase the resolution of a single image using only the information that what is contained within it [36, 25]. In single-frame super-resolution, several assumptions are considered in order to estimate the information between pixels and generate a high-resolution image. This approach differs strongly from the basic idea behind multi-frame super-resolution, where the combination of the information contained in different images is used to generate a high-resolution image.

In this chapter, a review of multi-frame super-resolution techniques is presented, to later discuss the application of these techniques in astronomy. Details concerning registration, the procedure used to align two or more images of the same scene, are also reviewed. Registration is an early step required for multi-frame super-resolution, since an estimation of a motion model that relates the set of low-resolution images is needed to process them together and generate a high-resolution image. In fact, registration is a critical step for super-resolution, because if the error degree is significant in the estimation of the registration parameters, then the quality of the reconstructed image will be severely affected. Finally, a short summary about currently available super-resolution software is presented, and the impossibility of using it for this thesis is discussed.

## 2.1 Super-resolution methods

A comprehensive review covering the wide variety of multi-frame super-resolution techniques was presented by Park *et al.* [48] in 2003. In this article, the basic concepts required to understand the different approaches used by the most classical multi-frame super-resolution algorithms are reviewed. However, it is important to note that since Park *et al.*'s publication, a great deal of new super-resolution techniques have been developed, but they are usually focused on more specific cases and work under more restrictive assumptions for the super-resolution problem.

In the following sections, a summary analyzing the multi-frame super-resolution techniques more widely reviewed in the image processing literature is presented. These techniques can be classified, first, according to the domain where the problem is posed. The first multi-frame super-resolution techniques developed consider the utilization of the frequency domain to process the set of low-resolution images. Later on, the problem was addressed in the spatial domain, which means to use only the pixel values and their coordinates. Besides these two main categories, another type of methods, known as Projection Onto Convex Sets (POCS), are presented, which base their operation on the definition of constraints (that can be established either in the spatial or the frequency domain) for the high-resolution image that is to be reconstructed.

Another relevant characteristic that is employed to classify these algorithms is given by the mathematical formulation used to find a solution of the problem. There are two main categories in regards to this formulation. The first one is known as *Maximum Likelihood* (ML) and groups all the methods that generate a high-resolution image by maximizing the probability of obtaining the set of low-resolution images under an specific model. The second category, in which most algorithms can be included and that is known as *Maximum A Posteriori* (MAP), considers the explicit utilization of prior information about the image that should be reconstructed when the probability is maximized according to the available set of low-resolution images. The classification of the different algorithms into these two categories is also discussed in the following sections.

Finally, an overview about the modern approaches towards multi-frame super-resolution is presented. These approaches are usually mixed versions of the ones already mentioned, but they also use more sophisticated tools to handle the different processes and estimate the parameters involved in multi-frame super-resolution reconstruction, such as machine learning or sparse representations.

### 2.1.1 Frequency domain methods

Tsai and Huang [71] were the first to develop a multi-frame super-resolution method in 1984 by posing the problem in the frequency domain. In their approach, a high resolution image is obtained considering its relation with many low-resolution images as a function of the shifting and aliasing properties of the Continuous and Discrete Fourier Transforms (CFT and DFT). In their formulation only translational motion is included, and the translations are

considered known parameters. In this formulation, a model for the blur and the noise that affect an image when acquired through an imaging device is not considered. This work was later extended by Kim *et al.* [40, 7], precisely by adding spatial blurring and observational noise to the previous model, as well as introducing Tikonov regularization [65] in order to deal with the multi-frame super-resolution problem even when it is ill-posed (which happens when not enough complementary information is available from the set of low-resolution images used as input).

Tom and Katsaggelos [69, 70] apply a two step approach for multi-frame super-resolution. The first step corresponds to denoising, deblurring and registration of the low-resolution images of the input set (the two first procedures are used to improve the quality of each low-resolution image). The second step is given by the inclusion of the low-resolution pixels into a high-resolution grid to then obtain the new image using interpolation. Although most of the problem is posed in the spatial domain, the image reconstructed in the second step is anyway presented as the solution obtained for a frequency domain problem. Nguyen and Milanfar [45] have proposed the use of wavelet models for the super-resolution problem, considering an approach similar to the methods that work in the Fourier space. In their algorithm, they represent each low-resolution image in terms of the coefficients of their wavelet transforms, to then relate these coefficients with the ones of the high-resolution image that is expected to be recovered.

A method based on the Second-Generation Wavelet Transform (SWGTT) is proposed by Bose *et al.* [8], showing good results for images that present high levels of noise corruption. Islam *et al.* [34] have presented a single-image super-resolution method based on regression analysis and Neighborhood Dependent Component Feature Learning (NDCFL). Considering a low-resolution image as input, this method estimates the regression kernel adaptively, using directional Fourier phase feature components, based in the analysis of local covariances to then recover a high-resolution version of the input image.

### 2.1.2 Spatial domain methods

Spatial domain methods have been developed in parallel to the methods that operate in the frequency domain. These methods handle the multi-frame super-resolution problem using the values and coordinates of the pixels, providing a better mechanism to deal with the presence of noise in images and a better treatment of the blurring effects that can not be approximated by a single convolution. One of the first spatial domain methods was proposed by Peleg *et al.* [52] in 1987, where the reconstruction of a high-resolution image is achieved by using the sub-pixel motions that are considered known. The optimization procedure behind this reconstruction mechanism was performed using simulated annealing.

Keren *et al.* [39] propose a registration method that deals with a more sophisticated motion model, which includes translations and rotations in the plane of the images. However, they do not achieve much improvement in terms of the recovery of high-frequency information in the reconstructed high-resolution image. Irani *et al.* [31, 32] based their work on the same registration algorithm used in [39], but developed a more detailed method to recover the high-resolution image based on the utilization of back-projections (which is essentially the

difference between the low-resolution version of the high-resolution image estimate and each low-resolution image used as input). They also consider a procedure to estimate the blur present in the images by analyzing the degradation of features as sharp edges or small points. Later work [33] shifts the focus of their approach to using the registration of rigid objects that are tracked in an image sequence, in order to obtain high-resolution images of these objects. In this case, three different models (with 2, 6 and 8 degrees of freedom) are used to identify, with enough flexibility, the motion of the objects to then obtain a high-resolution image considering a segmentation of the relevant zones of the input images.

Rudin *et al.* [27, 56] and Ur and Gross [72] propose methods using a more complex imaging model, where translations, rotations, warping and resampling of the images are contemplated. Although these methods perform well in general, the treatment of the high frequencies is not good enough to recover sharp edges correctly. Elad and Hel-Or [20] limited the imaging model to develop faster algorithms. Their methods work for shifting motions restricted only to vertical and horizontal integer displacements of the high-resolution pixels, and consider a common noise model, zoom factor and spacially-invariant blur function for each one of the images used as input. With these restrictions, they treat the blur after the interpolation of the high-resolution image, using a deconvolution scheme based in the utilization of a Wiener filter.

### 2.1.3 Projection onto convex sets

A third relevant approach towards multi-frame super-resolution is represented by a group of algorithms that rely in the utilization of a technique know as Projection Onto Convex Sets (POCS). The work of POCS is based on the definition of constraints, in the form of convex sets, that should be satisfied by the pixels of the high-resolution image [48]. Mainly, this constraints are defined as a function of the pixel values contained in each one of the low-resolution images, but other types of restrictions can be also included (such as smoothness) in order to obtain a better solution. Then, an estimate of the high-resolution image is iteratively improved by projecting it sucessively into each one of these convex sets. As more iterations are performed, the estimate converges to the intersection of the convex sets, which means that the reconstructed image will satisfy all the constraints previously defined.

Strictly speaking, the POCS approach is not an independent category respect to the two ones presented above, since the set of restrictions can be established either in the spatial or the frequency domain. However, this approach contemplates a different mechanism to recover a high-resolution image, where all the parameters involved can be included in the super-resolution model with more flexibility. Among the disadvantages of the POCS method we can mention non-uniqueness of the obtained solutions, slow convergence and a high-computational cost [48].

Since the first works by Stark and Oskoui [61] were proposed, which were based on spatial domain methods, many extensions have been applied to the POCS method for multi-frame super-resolution. Eren *et al.* [21] extend early work by Patti *et al.* [50], by using segmentation maps on pre-registered input images. Elad and Feuer [18] propose an hybrid method that combines Machine Learning with POCS methods to optimize the set of convex constraints.

Later work by Elad and Feuer [19] and by Patti *et al.* [51] use Kalman filtering to make the solution more computationally efficient. Patti and Altunbasak [49] consider a scheme where prior knowledge of the high-resolution image is included in the set of constraints, which yields to a regularization of the super-resolution problem under the POCS approach.

Panda *et al.* [47] use adaptative regularization parameters, based on the noise variance of the input images, achieving an stabilization in the operation of previous methods which yields better performances. Shen *et al.* [59] propose a method that combines POCS in both the space and the frequency domains. This method reduces the presence of artifacts and noise in the high-resolution image that is reconstructed.

### 2.1.4 Formulations of the super-resolution problem

All the different methods presented so far can be also classified according to the formulation considered to obtain a solution of the multi-frame super-resolution problem. As was previously mentioned, there are two main categories in terms of formulation. The first one is known as *Maximum Likelihood* (ML) while the second one is known as *Maximum A Posteriori* (MAP).

In the ML approach for multi-frame super-resolution, a high-resolution image is reconstructed by maximizing the probability of obtaining each one of the low-resolution images, used as input of the process, from this reconstructed image according to the different parameters considered, such as the registration information and the blur. On the other hand, in the MAP approach, prior knowledge about the high-resolution image that is expected to be reconstructed is included in the super-resolution model before maximizing the probability of obtaining each low-resolution image from this reconstructed high-resolution image. The mathematical aspects behind these two approaches are dealt with more detail in Chapter 3.

In practice, there is greater prevalence of methods based in the MAP approach over the ones based in the ML approach. This is consequence of a practical situation: usually, the quality or the amount of available low-resolution images is not enough to properly reconstruct a high-resolution image. The use of prior information in the MAP approach is equivalent to regularizing the reconstruction problem, allowing then for the obtention of a solution of the multi-frame super-resolution problem even under these limitations.

The first multi-frame super-resolution methods, such as the ones presented in [39, 31, 32, 40, 7, 61], were developed considering a ML approach, while modern ones tend to consider a MAP formulation of the super-resolution problem. One of the earliest examples of MAP super-resolution belongs to Cheeseman *et al.* [12] with their reconstruction of images of Mars based in a Bayesian scheme, for modelling the likelihood between each low-resolution image and the reconstructed high-resolution, and the utilization of an extremely simple Gaussian prior (that related each high-resolution pixel with its four immediate neighbors) in order to incorporate the prior knowledge required in the reconstruction process.

Woods *et al.* [74] developed an Expectation-Maximization (EM) algorithm for performing joint registration, deconvolution and interpolation under a MAP formulation for the multi-

frame super-resolution problem. All the prior distributions are assumed Gaussian for each one of the three procedures considered. Chantas *et al.* [11] use a locally adaptive edge preserving prior for their MAP version of the multi-frame super-resolution problem. They combine this with an iterative algorithm to perform a simultaneous restoration, registration and interpolation in the Fourier domain. Belekos *et al.* [2] present a multichannel approach for MAP-based super-resolution reconstruction. The multichannel prior incorporates registration information between different frames. This approach has been successfully used in the past for video reconstruction [13]. Lukes *et al.* [43] introduce a high-performance and MAP-based super-resolution method that was developed for the reconstruction of high-resolution microscopy images.

### 2.1.5 Modern approaches towards multi-frame super-resolution

A popular branch of current multi-frame super-resolution algorithms relies on the minimization of cost functions defined in terms of the  $L_1$  norm [77], considering a regularized model based in the utilization of total variation priors. The success of these methods depends on the assumption that good image priors are available. Research on wavelet-based image denoising suggests that the sparsity in wavelet coefficients can be used as a good prior [16]. The idea of finding a sparse prior in the context of multi-frame super-resolution derives from the compressed sensing principle, which states that a high-resolution sparse signal can be recovered from its downsampled version by finding the sparsest solution, known as sparse representation, with respect to a properly chosen dictionary.

The mathematical background behind multi-frame super-resolution algorithms based on sparse representation has been provided by C andes *et al.* [9]. Dong *et al.* [15] have taken advantage of the success of sparse representation and presented image deblurring techniques based on adaptive sparse domain selection. Yang *et al.* [79] deal with the multi-frame super-resolution problem using the compressed sensing approach. They demonstrate that sparsity is an effective prior for regularizing the super-resolution problem. In [80], they show that a high-resolution image, superior in quality than those produced by other super-resolution methods, can be obtained from a set of randomly chosen raw patches from training images.

Machine-learning approaches towards multi-frame super-resolution have also been developed in the last years. Yang *et al.* [78] used machine-learning techniques on their raw-patch developments. They employed a dictionary training method for single image super-resolution. The learned dictionaries use sparse representation to relate the low and high-resolution image patches. Using neural networks, they achieved a substantial minimization of the time required to find the sparse representation employing their dictionary learning algorithms. Wu *et al.* [76] presented a machine-learning approach based on the utilization of a Kernel Partial Least Squares (KPLS) regression model [3], which is employed to relate a high-resolution image with its low-resolution version.

Deep-learning methods are also being developed in the context of super-resolution. For example, Dong *et al.* [14] propose a deep-learning method, based on the utilization of convolutional networks and sparse-representation, for dealing with the problem of single image super-resolution. Using the patches defined by the sparse representation, their method

directly learns an end-to-end mapping between the low-resolution and the high-resolution images.

Although all of these techniques present novel, interesting, and successful approaches to the super-resolution problem, they cannot be used in the context of this thesis, since all of them are based on sparse-representation and the identification of patches within the images. With the techniques mentioned above, the detection of a set of common patches for a set of low-resolution images is not feasible due to the presence of noise. Without a set of common patches is not possible to relate all these low-resolution images with the high-resolution image that is expected to be reconstructed.

## 2.2 Super-resolution techniques in astronomy

In the following sections, two techniques used in astronomy to generate high-resolution images from a set of low-resolution images as input are presented. Their relation with the multi-frame super-resolution problem is also discussed, since both techniques were developed considering restrictions or some strong assumptions for this problem.

### 2.2.1 Variable-pixel linear reconstruction

There is only one clear example of the utilization of multi-frame super-resolution algorithms in astronomy. This example corresponds to the algorithm known as Variable-Pixel Linear Reconstruction, also known as *Drizzle*, which was developed for obtaining the high-resolution image known as *Hubble Deep Field* in 1996 using images obtained by the Hubble Space Telescope. The operation of this algorithm is based on the weighted combination of the pixels of different images as function of their statistical weights [23]. This supposes to project the pixels of the images considered over a new pixel grid with more resolution, where the new pixels have a smaller size than the original ones, in order to establish the value of each one of these new pixels as the weighted average of the original pixels that contain (or overlap) the new set of pixels. The weight is then calculated in terms of the overlap areas of every original pixel and the new ones. It is important to note that the alignment parameters between the images considered should be known beforehand, to project in a proper manner each one of the images into the new grid of pixels.

This rescaling process implies the introduction of a new convolution in the resulting image, which is a function of the new pixel distribution, affecting then the quality of this new image. In order to reduce this effect, before calculating the new pixel values and after projecting the original pixels into the new grid, an artificial reduction in the size of these original pixels is introduced, as means to concentrate the contribution of each original pixel over a small number of new pixels, to diminish the effects of the convolution in the final result. Therefore, this reduction factor in the pixel size should be small enough to minimize the degradation effects in the resulting image, but large enough to totally cover the new grid of pixels and combine enough data (from the original pixels) in each one of the new pixels. A diagram of

the procedure described is presented in Figure 2.1.

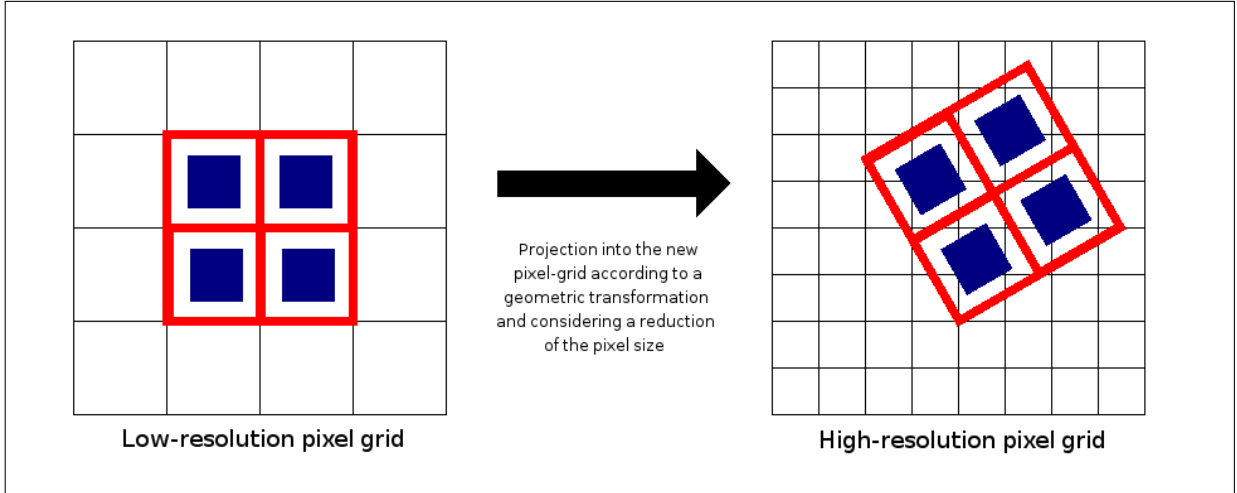


Figure 2.1: Diagram of the operation of the variable-pixel linear reconstruction algorithm.

Improved versions of this algorithm have been developed afterwards, both for astronomical use [64] and for other areas related with image processing [44]. Although this algorithm corresponds to a multi-frame super-resolution technique, its use is limited to very specific cases, due to the lack of a mechanism to deal with the presence of blur (which is a typical problem in astronomical images). In fact, the images obtained by the Hubble Space Telescope represent one of these specific cases where this technique is useful, since there is a minimal presence of blur distortions (because the observations of this telescope, unlike to what happens with observations from ground-based telescopes, are not affected by the presence of the atmosphere).

## 2.2.2 Lucky imaging

Another technique used in astronomy that can be partially related with multi-frame super-resolution is lucky imaging. This technique bases its operation in the utilization of high-speed cameras to obtain a great deal of images of an astronomical object, with small exposure times of about ten milliseconds [60], in order to avoid a decrease in image quality as a consequence of atmospheric turbulence. Degradation of image quality can be relevant even for short exposure times of about 200 milliseconds [1].

After the obtention of the images with the high-speed camera, a subset of these images is constructed by selecting the best of them in terms of a quality measure (such as the Strehl ratio<sup>1</sup>). The portion of images considered in this subset is typically between 5% and 20% of the total images. Later, these images are aligned using the location of the pixel with the highest value, and then they are projected on a common high-resolution grid to finally obtain the final image from the average of these projections.

<sup>1</sup>The Strehl ratio is usually defined as the ratio between the peak intensity value of an aberrated image of a point source and the maximum attainable intensity, using an ideal optical system limited only by diffraction over the aperture of the system. The Strehl ratio is used in situations where optical resolution is compromised due to lens aberrations or due to imaging through a turbulent atmosphere.

Improved versions of this technique have been proposed in the last years. For example, in [24] the lucky imaging procedure is improved by performing the selection of the best images in the Fourier space. Although this technique can be considered as a super-resolution procedure, it works only under strict conditions on the images that are used (very short exposure times), which can only be satisfied with specialized instrumentation (high-speed cameras). Therefore, as in the previous case, this technique is not useful for the problem of multi-frame super resolution that is addressed in this thesis.

## 2.3 Image registration and super-resolution

Image registration represents a crucial early step for multi-frame super-resolution. In this step, a motion model is estimated in order to locate the pixels of the low-resolution images in a common system of coordinates. Since motions with sub-pixel precision should exist to use super-resolution techniques, the registration procedure should be able to estimate the motion parameters with a high level of accuracy (otherwise, the errors in the estimation of the registration parameters will affect the quality of the reconstructed high-resolution image). There are few cases where multi-frame super-resolution algorithms do not use motion changes to define the constraints required to reconstruct a high-resolution image, but instead defocus [55] or zoom variations [37] are used.

Image registration techniques can be classified into two main categories. In the first one, known as *feature-based* registration, the main idea is to find a group of distinctive features contained in two (or more) images. Then, by analyzing the correspondences between these features it is possible to establish a geometric transform that is used to map the pixel coordinates of one image into the other [82, 26]. A popular mechanism to perform registration under this approach is to use block-matching algorithms [58]. On the other hand, *intensity-based* registration works by comparing the pixel values of two or more images using similarity (or dissimilarity) metrics that should be maximized (or minimized) in order to find an estimation of the registration parameters [82, 26]. As examples of these metrics we can mention the Sum of Squared Differences (SSD), Cross Correlation (CC) and Mutual Information (MI). Both approaches can be even used in spaces other than the spatial domain, such as the frequency [73] or the wavelet domains [42].

Although in most cases the registration process is considered as an independent task with respect to multi-frame super-resolution reconstruction, there are some examples where both procedures are performed simultaneously. For example, Hardie *et al.* [28] propose a method, based on a MAP framework, where the registration parameters are iteratively updated with the high-resolution image estimate during the optimization procedure. Also, Woods *et al.* [74, 75] present two methods for a joint estimation of the registration parameters and the high-resolution image, the first one based on an expectation-maximization approach while the second one is based on a MAP formulation of the joint problem.

In the context of astronomical imaging, one can rely only on the use of *intensity-based* registration algorithms. This is due to the fact that features which can be identified in an astronomical image are not usually distinctive enough to be used in order to estimate a

geometrical transform. In astronomical images, stars and galaxies usually have circular or elliptical shapes (which can be severely affected by the multiple disturbing effects involved in the acquisition process of astronomical images), and these shapes are repeated multiple times in the same image, meaning it is not easy to use *feature-based registration* without human-inspection, which would be the only way of obtaining a proper feature selection.

Because of the situation described above, and since registration is not the main concern of this thesis, a simple registration procedure was considered, based on the minimization of the SSD between two or more images. This allowed us to state the problem of image registration as an optimization problem. Also, two motion models were considered with this procedure: the first model uses affine transforms (6 degrees of freedom) to estimate the motion parameters for the set of low-resolution images, while the second model considers quadratic transforms (12 degrees of freedom) to perform this estimation.

## 2.4 Super-resolution software

In simple terms, the problem addressed is to reconstruct a high-resolution image using a set of astronomical images of the same scene as input, where the reconstructed image should not only have a higher resolution, but also less blur and less noise than any of the input images. As far as we know, there is no computational tool that can be used to properly cope with this problem, since most of the multi-frame super-resolution applications do not include a mechanism to deal with the presence of blur (which is a relevant degradation factor in astronomical imaging).

Because of this, the available multi-frame super-resolution tools are not useful for the purposes of this thesis, where the blur is one of the relevant parameters to be considered in the evaluation performance of the multiple parameter algorithms. Besides, the study developed in this thesis contemplates other complex aspects about multi-frame super-resolution, such as different approaches for the optimization procedure, as well as the utilization of different procedures to deal with the presence of noise. Thus, the tools available are not useful since they are not flexible enough to include these relevant aspects that need to be analyzed.

Below, some of the available multi-frame super-resolution tools, which have been developed as an outcome of publications or for astronomical purposes, are listed and described:

1. IRAF: The Image Reduction and Analysis Facility [67, 68], commonly known as IRAF, is a software developed for processing astronomical data. The *dither* package contains a set of routines that allow the obtention of high-resolution images using the variable-pixel linear reconstruction algorithm that was previously introduced. This software performs registration using the astrometric information of the images, which is essentially the location of the observed scene in the sky (this information is stored as meta-data in the image file), this being a non ideal approach since the astrometric information already contains some degree of error.

2. Montage<sup>2</sup>: This software is virtually an improved version (in technical terms) of the multi-frame super-resolution procedure implemented by IRAF, since the reconstruction algorithm and the registration mechanism are almost the same. Montage was developed to process large amounts of images, considering a parallel and scalable design. This tool can be downloaded or used on-line.
  
3. Software related to publications: There are multiple implementations of the algorithms in different publications. In general, these implementations are focused only on the particular case analyzed in the corresponding publication, and not all relevant parameters are considered (at least for the case of astronomical images) or their values are hard-coded. Also, the scope of the study developed in this thesis considers a more complex approach where we also analyze two different mechanisms for the optimization procedure in which multi-frame super-resolution relies, as well as the utilization of some schemes to deal with the presence of noise in the input images. Thus, it is not possible to use these implementations as tools for developing the analysis proposed by this thesis. Some examples of these codes can be found in the following links:

- <http://www.robots.ox.ac.uk/~vgg/software/SR/index.html>
- <http://decsai.ugr.es/pi/superresolution/software.html>
- <http://www.ece.lsu.edu/ip1/Software.html>

---

<sup>2</sup><http://montage.ipac.caltech.edu/>

# Chapter 3

## Super-resolution theory

The purpose of this chapter is to present, in a detailed manner, all the concepts related to multi-frame super-resolution that will be used as part of this thesis. In order to do this, we first present the Image Observation Model (IOM), which is the mathematical basis required to properly state the super-resolution problem. All the parameters involved in this model will be explained and reviewed. Then, different expressions that pose the multi-frame super-resolution as an optimization problem will be derived under several assumptions. Also, the gradients of these expressions will be calculated as they will be required by the optimization procedures for reconstructing high-resolution images.

The expressions obtained here will be employed in following chapters to describe, in a more specific manner, each one of the four multi-frame super-resolution algorithms that are analyzed in this thesis and that were previously introduced. These expressions are given by two cost functions and two different formulas derived for computing the corresponding gradient of each one of these cost functions. The importance of these expressions comes from the fact that they are employed by each one of the multi-frame super-resolution algorithms, since these algorithms are defined as different combinations between a cost function, that must be minimized in order to find a high-resolution image, and a mechanism to compute the gradient of such cost function.

Finally, we present the mathematical basis required to understand how image registration works, since the obtention of an accurate estimate of the registration parameters represents a crucial requirement for the operation of each multi-frame super-resolution algorithm. Image registration is also posed as an optimization problem, where a cost function must be minimized, using its gradient, for obtaining an estimation of the registration parameters. The cost function with its corresponding gradient is derived for the two image registration mechanisms employed in this thesis: affine and quadractic registration.

### 3.1 Image Observation Model (IOM)

The first step required to state the super-resolution problem is to establish a relation between the set of low-resolution images and a high-resolution image, considering that every low-resolution image is a degraded version of this high-resolution image. Such relation is expressed through the IOM [48], which attempts to capture the physical process by which observed data (in this case, the set of low resolution images) is generated by an underlying imaging system.

Since a perfect imaging system does not exist, due mainly to technical limitations and the influence of the atmosphere, the process of acquiring an image is always affected by various kinds of degrading effects. The purpose of the IOM is to represent this process, illustrated by the diagram presented in Figure 3.1, in the most precise and accurate way possible. The input of an imaging system is a continuous scene, whose sampling (at or above the Nyquist rate), affected by atmospheric turbulence, generates a degraded version of the high-resolution image which is expected to be recovered by the super-resolution procedure. Then, this image is affected by some sort of motion between the imaging system and the scene to be captured, generating a different displaced version for every motion considered. This set of images is then affected by blurring effects (such as motion blur and/or optical blur), which means that every image is convolved by a blur kernel. All these blurred images are then downsampled into pixels in the imaging system sensors, to finally be affected by the different kinds of sensor noise. In other words, every low-resolution image of a common scene obtained using an imaging system is a corrupted by the atmosphere, displaced, blurred, decimated, and noisy version of a common high-resolution image.

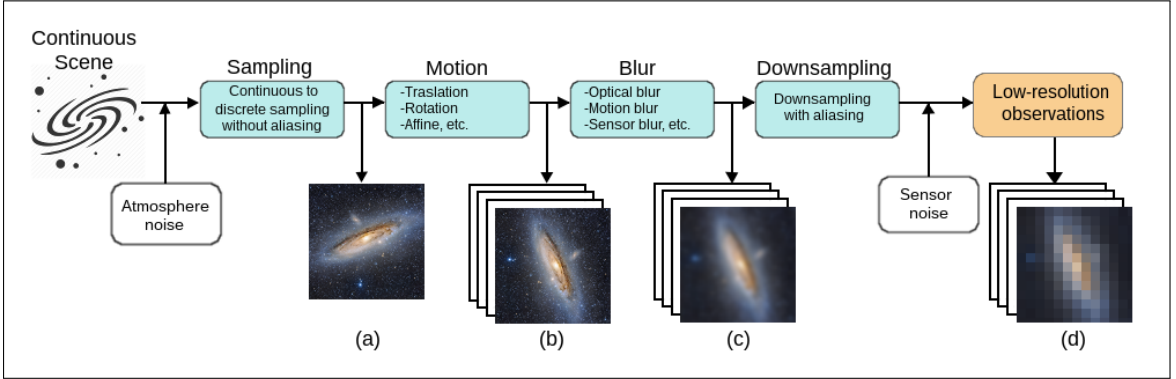


Figure 3.1: Diagram of the image acquisition process

#### 3.1.1 Mathematical formulation

Considering a set of  $N$  low-resolution images, each one represented by the vector  $\mathbf{Y}_k$  (with  $k = 1, \dots, N$ ), and their corresponding high-resolution image, represented by the vector  $\mathbf{X}$ , the IOM expresses the degradation process previously described as the following system of  $N$  matricial linear equations:

$$\mathbf{Y}_k = \mathbf{D}_k \mathbf{B}_k \mathbf{M}_k \mathbf{X} + \mathbf{V}_k ; k = 1, \dots, N \quad (3.1)$$

where  $\mathbf{M}_k$ ,  $\mathbf{B}_k$  and  $\mathbf{D}_k$  are matrices that represent the motion operator, the blur operator and the downsampling operator, respectively, while the vector  $\mathbf{V}_k$  represents the noise term for the  $k$ -th low-resolution image.

In these equations, all the images are represented by vectors considering a lexicographical notation, which means that all the pixels contained in an image are rearranged in a vector but maintain their relative order (every row is transformed in a column and then all these columns are vertically concatenated in an unique new column). Therefore, if the size of the high-resolution image is  $LN_1 \times LN_2$  and the size of each one of the low-resolution images is  $N_1 \times N_2$ , then the size of the vector  $\mathbf{X}$  will be  $L^2N_1N_2$  and the size of the vector  $\mathbf{Y}_k$  will be  $N_1N_2$  (for  $k = 1, \dots, N$ ). The size of the other elements included in Eq. (3.1) will be defined as a function of the sizes of  $\mathbf{X}$  and  $\mathbf{Y}_k$ : the motion matrix  $\mathbf{M}_k$  and the blur matrix  $\mathbf{B}_k$  will have a size of  $L^2N_1N_2 \times L^2N_1N_2$ , the downsampling matrix  $\mathbf{D}_k$  will have a size of  $(N_1N_2)^2 \times L^2N_1N_2$ , while the noise vector  $\mathbf{V}_k$  will have a size of  $N_1N_2$  (for  $k = 1, \dots, N$ ).

A more compact form of expressing the system of matricial linear equations specified in Eq. (3.1), which will be useful for further calculations, is given by:

$$\mathbf{Y}_k = \mathbf{W}_k\mathbf{X} + \mathbf{V}_k ; k = 1, \dots, N \quad (3.2)$$

where the matrix  $\mathbf{W}_k$ , with a size of  $(N_1N_2)^2 \times L^2N_1N_2$ , represents the matricial product of matrices  $\mathbf{D}_k$ ,  $\mathbf{B}_k$  and  $\mathbf{M}_k$  (for  $k = 1, \dots, N$ ). This means that matrix  $\mathbf{W}_k$  contains almost all the information (except for the noise) associated to the degradation process of the  $k$ -th low-resolution image.

The system of  $N$  linear equations specified by the IOM is not easy to solve and is typically ill-posed, since the matrix  $\mathbf{W}_k$  is usually ill-conditioned. In practice, an analytical expression for the matrices  $\mathbf{M}_k$ ,  $\mathbf{B}_k$  and  $\mathbf{D}_k$  does not exist, and their estimates should be obtained from the set of available low-resolution images, which complicates the resolution of the equation system even further. This situation leads to the use of regularization as a key element in order to find a solution for the super-resolution problem.

### 3.1.2 Parameters of the image observation model

The IOM considers the following 4 parameters for representing, in mathematical terms, the physical process of image acquisition in an imaging system:

1. Motion: The matrix  $\mathbf{M}_k$  represents the motion that affected the high-resolution image when the low-resolution image  $\mathbf{Y}_k$  was acquired. This motion is essentially a geometrical transformation such as an affine or a quadratic transform. Since this motion information is generally unknown, but used as a parameter of this model, it is necessary to estimate the motion of the low-resolution images (with respect to one of them used as reference) using a registration procedure.
2. Blur: The blurring that affects the quality of the low-resolution images is the combined

result of three different types of blur: optical blur (which may be a consequence of defocus, aberrations, the diffraction limit, etc), motion blur (relative motion between the imaging system and the observed scene) and the PSF. The combined effect of these three factors in the acquisition of the low-resolution image  $\mathbf{Y}_k$  is represented by the matrix  $\mathbf{B}_k$  in the IOM.

3. Downsampling: This is the process by which low-resolution pixels are obtained as the weighted sum of a group of high-resolution pixels. The weight of each high-resolution pixel in its associated low-resolution pixel will be defined by the relative size between these pixels and by the blur that affects the high-resolution image. The downsampling of the low-resolution image  $\mathbf{Y}_k$  is represented by the matrix  $\mathbf{D}_k$  in the IOM.
4. Noise: The noise contained in a low-resolution image is represented in the IOM by the vector  $\mathbf{V}_k$ . In practice, there are multiples sources of noise (such as shot noise, read noise, dark current, etc) and each one follows an specific distribution. In the context of the IOM, the elements of the noise term must exhibit a Gaussian distribution with zero-mean.

## 3.2 Probabilistic framework of super-resolution

In a probabilistic context, an estimation of the high-resolution image ( $\hat{\mathbf{X}}$ ) can be obtained from the maximization of the conditional probability of the high-resolution image ( $\mathbf{X}$ ) given the set of available low-resolution images ( $\mathbf{Y}_1, \dots, \mathbf{Y}_N$ ):

$$\hat{\mathbf{X}} = \underset{\mathbf{X}}{\text{ArgMax}} \left[ \mathbb{P}(\mathbf{X} \mid \mathbf{Y}_1, \dots, \mathbf{Y}_N) \right] \quad (3.3)$$

Due to Bayes' theorem and considering that  $\mathbb{P}(\mathbf{Y}_1, \dots, \mathbf{Y}_N)$  is constant with respect to  $\mathbf{X}$ , the previous expression can be rewritten as:

$$\hat{\mathbf{X}} = \underset{\mathbf{X}}{\text{ArgMax}} \left[ \mathbb{P}(\mathbf{Y}_1, \dots, \mathbf{Y}_N \mid \mathbf{X}) \mathbb{P}(\mathbf{X}) \right] \quad (3.4)$$

where  $\mathbb{P}(\mathbf{Y}_1, \dots, \mathbf{Y}_N \mid \mathbf{X})$  is the likelihood of the data (low-resolution images) and  $\mathbb{P}(\mathbf{X})$  is the prior term on the expected high-resolution image.

From the expression of the IOM given by Eq. (3.2), and under the assumption of Gaussian distribution with zero mean and standard deviation  $\sigma$  for the elements of the noise vector  $\mathbf{V}_k$  ( $V_{k,i} \sim \mathcal{N}(0, \sigma^2)$ , for  $i = 1, \dots, N_1 N_2$ ), the likelihood of the low-resolution image  $\mathbf{Y}_k$  given the high-resolution image  $\mathbf{X}$  may be written as:

$$\mathbb{P}(\mathbf{Y}_k | \mathbf{X}) = \left( \frac{1}{2\pi\sigma^2} \right)^{\frac{N_1 N_2}{2}} \exp \left( -\frac{1}{2\sigma^2} \|\mathbf{W}_k \mathbf{X} - \mathbf{Y}_k\|_2^2 \right) \quad (3.5)$$

Therefore, considering the independence of the likelihood corresponding to each one of the low-resolution images, the likelihood of the whole set of  $N$  low resolution images, given the high resolution image  $\mathbf{X}$ , can be expressed as:

$$\mathbb{P}(\mathbf{Y}_1, \dots, \mathbf{Y}_N | \mathbf{X}) = \left( \frac{1}{2\pi\sigma^2} \right)^{\frac{NN_1 N_2}{2}} \exp \left( -\frac{1}{2\sigma^2} \sum_{k=1}^N \|\mathbf{W}_k \mathbf{X} - \mathbf{Y}_k\|_2^2 \right) \quad (3.6)$$

With the result obtained above, the selection of the prior term,  $\mathbb{P}(\mathbf{X})$ , is the only pending step required to complete the formulation of the problem as the optimization of a parametrized cost function. The selection of the prior term usually falls into one of two main approaches. The first approach, known as *Maximum Likelihood*, bases its operation in seeking only the high-resolution image that maximizes the conditional probability of the set of available low-resolution images given that same image. The second approach, known as *Maximum a Posteriori*, obtains the high-resolution image using explicit information about it. The details concerning each one of these methods will be reviewed below.

Before continuing, it is important to highlight one relevant and critical assumption considered in this probabilistic formulation of the super-resolution problem: for every low-resolution image  $\mathbf{Y}_k$ , the degradation matrix  $\mathbf{W}_k$  is assumed to be known. This means that the registration, blur, and downsampling parameters should be estimated beforehand, for every low-resolution image, in order to obtain the high-resolution image  $\mathbf{X}$  using super-resolution techniques.

### 3.2.1 The *Maximum Likelihood* approach

The *Maximum Likelihood* (ML) approach is based on the selection of an uniform prior term to obtain the high-resolution image. The only condition that this image should satisfy is the maximization of the likelihood of the complete set of low-resolution images. Therefore, considering that  $\mathbb{P}(\mathbf{X}) = \alpha$  (with  $\alpha$  a positive constant) and using the relation obtained in Eq. (3.6) for the likelihood, it is possible to express Eq. (3.4) for this case as it follows:

$$\begin{aligned} \hat{\mathbf{X}}_{ML} &= \underset{\mathbf{X}}{\text{ArgMax}} \left[ \alpha \mathbb{P}(\mathbf{Y}_1, \dots, \mathbf{Y}_N | \mathbf{X}) \right] \\ &= \underset{\mathbf{X}}{\text{ArgMax}} \left[ \alpha \left( \frac{1}{2\pi\sigma^2} \right)^{\frac{NN_1 N_2}{2}} \exp \left( -\frac{1}{2\sigma^2} \sum_{k=1}^N \|\mathbf{W}_k \mathbf{X} - \mathbf{Y}_k\|_2^2 \right) \right] \end{aligned} \quad (3.7)$$

Since the expression that should be maximized corresponds to a monotonically decreasing function of  $\sum_{k=1}^N \|\mathbf{W}_k \mathbf{X} - \mathbf{Y}_k\|_2^2$ , the super-resolution problem can be equivalently expressed as the following minimization problem:

$$\hat{\mathbf{X}}_{ML} = \underset{\mathbf{X}}{\text{ArgMin}} \left[ \sum_{k=1}^N \|\mathbf{W}_k \mathbf{X} - \mathbf{Y}_k\|_2^2 \right] \quad (3.8)$$

This minimization problem has an analytical pseudoinverse solution which is obtained differentiating Eq. (3.8) with respect to  $X$  and equating this derivative to zero, yielding to:

$$\hat{\mathbf{X}}_{ML} = (\mathbf{W}^T \mathbf{W})^{-1} \mathbf{W}^T \mathbf{Y} \quad (3.9)$$

where  $\mathbf{W}$  is a matrix of size  $N(N_1 N_2)^2 \times L^2 N_1 N_2$ , generated by stacking the  $N$  degradation matrices  $\mathbf{W}_k$ , and the vector  $\mathbf{Y}$ , with a size of  $N N_1 N_2$ , is the stack of the  $N$  low-resolution image vectors  $\mathbf{Y}_k$ . This expression represents a direct solution for obtaining  $\mathbf{X}$  from the set of  $\mathbf{W}_k$  matrices.

In practice, ML multi-frame super-resolution is an ill-posed problem whose solution can be affected by a great deal of elements. For example, if  $\mathbf{W}^T \mathbf{W}$  is a singular matrix, then there is an infinite number of possible solutions. Also, due to the high-dimensionality of this problem, the computation of the inverse matrix of  $\mathbf{W}^T \mathbf{W}$  is computationally prohibitive. However, the main downside of ML multi-frame super-resolution is that it does not include any mechanism for preventing overfitting, which means that the suitability of the recovered images can be compromised by this effect.

### 3.2.2 The *Maximum A Posteriori* approach

In order to deal with the limitations of the ML approach, the selection of a suitable prior term for  $X$  is required for discarding implausible solutions and convenient to avoid overfitting. This is the basic idea behind the functioning of the multi-frame super-resolution methods based in the *Maximum A Posteriori* (MAP) approach.

The prior term is typically defined, in the MAP approach, by the Gibbs distribution:

$$\mathbb{P}(\mathbf{X}) = \frac{1}{Z} \exp(-\beta A(\mathbf{X})) \quad (3.10)$$

where  $A(\mathbf{X})$  is a non-negative potential function (also known as energy function),  $\beta$  is a positive constant and  $Z$  is simply a normalization factor. Then, replacing the prior term in Eq. (3.4) with this definition leads to expressing the super-resolution problem in the MAP approach as it follows:

$$\begin{aligned}
\hat{\mathbf{X}}_{MAP} &= \underset{\mathbf{X}}{\text{ArgMax}} \left[ \mathbb{P}(\mathbf{Y}_1, \dots, \mathbf{Y}_N | \mathbf{X}) \frac{1}{Z} \exp(-\beta A(\mathbf{X})) \right] \\
&= \underset{\mathbf{X}}{\text{ArgMax}} \left[ \frac{1}{Z} \left( \frac{1}{2\pi\sigma^2} \right)^{\frac{NN_1N_2}{2}} \exp \left( -\frac{1}{2\sigma^2} \sum_{k=1}^N \|\mathbf{W}_k \mathbf{X} - \mathbf{Y}_k\|_2^2 - \beta A(\mathbf{X}) \right) \right]
\end{aligned} \tag{3.11}$$

Since the expression that should be maximized corresponds to a monotonically decreasing function of  $\frac{1}{2\sigma^2} \sum_{k=1}^N \|\mathbf{W}_k \mathbf{X} - \mathbf{Y}_k\|_2^2 + \beta A(\mathbf{X})$ , the super-resolution problem can be equivalently expressed as the following minimization problem:

$$\hat{\mathbf{X}}_{MAP} = \underset{\mathbf{X}}{\text{ArgMin}} \left[ \sum_{k=1}^N \|\mathbf{W}_k \mathbf{X} - \mathbf{Y}_k\|_2^2 + \lambda A(\mathbf{X}) \right] \tag{3.12}$$

where the regularization parameter  $\lambda$  absorbs the variance of the noise ( $\sigma^2$ ) and the constant  $\beta$ . With this last expression, which represents the classical formulation of the MAP super-resolution problem, it is evident that the ML approach can be considered as a particular case of the MAP approach, where  $\lambda$  is set to zero. The functional that needs to be minimized in Eq. (3.12), and which will be referred in the successive as cost function, is composed by two elements: the data term (similarity cost) and the prior term  $A(\mathbf{X})$  (regularization cost). The balance between these two elements is established by the regularization parameter  $\lambda$ , which is also known as a Lagrange multiplier in the context of mathematical optimization.

### 3.3 Priors for MAP super-resolution

The main conclusion of the previous section is that the super-resolution problem, considering a MAP approach, can be expressed as the minimization with respect to  $\mathbf{X}$  of the following cost function:

$$F = \sum_{k=1}^N \|\mathbf{W}_k \mathbf{X} - \mathbf{Y}_k\|_2^2 + \lambda A(\mathbf{X}) \tag{3.13}$$

where it is still required to define the prior term  $A(\mathbf{X})$ , also known as regularization cost function, in order to have an explicit expression for  $F$ . In the following sections, two of the most widely referenced priors will be reviewed.

#### 3.3.1 Laplacian prior

The Laplacian prior represents an specific case of the Tikonov cost function [18, 46], which is one of the most referenced regularization techniques in literature. The Laplacian prior is

given by:

$$A_l(\mathbf{X}) = \|\mathbf{\Gamma}_l \mathbf{X}\|_2^2 \quad (3.14)$$

where  $\mathbf{\Gamma}_l$  is a matrix that represents the Laplacian operator. The purpose of selecting a Laplacian operator in this type of priors is to force spatial smoothness, as the noisy and edge pixels will be removed in the regularized minimization process and the resulting image will not contain sharp edges [22].

### 3.3.2 Gradient prior

The total variation (TV) method is one of the most popular image priors, specially for denoising and deblurring problems. In this method, the element penalized by the regularization cost function is the total amount of change in the image. This penalization is calculated as the  $L_1$ -norm of the magnitude of the image gradient. The mathematical expression for this prior is given by:

$$A_g(\mathbf{X}) = \|\nabla \mathbf{X}\|_1 \quad (3.15)$$

where  $\nabla$  is a matrix that represents the gradient operator. One of the advantages of this prior is that it tends to preserve edges in the regularized reconstruction process, as there is not a severe penalization over steep local gradients [57, 10]. Improved versions of this prior have been developed later, considering, for example, an adaptative local calculation for the gradient along the different structures detected in an image [62].

## 3.4 Optimization for MAP super-resolution

Although a solution for the minimization problem presented in Eq. (3.12) could be obtained with the exclusive utilization of the cost function  $F$ , using optimization procedures such as the Powell's conjugate direction method [54], this approach would be extremely inefficient since these kind of methods base their functioning in numerical calculations of the gradient. Due to the high dimensionality of the super-resolution problem, where each high-resolution pixel represents a variable that should be calculated, the utilization of these methods is not feasible.

Therefore, the derivation of an analytical expression for the gradient is a relevant step in order to use super-resolution techniques. In fact, if the gradient of the cost function  $F$  is known, the most straightforward way to obtain a solution of the multi-frame super-resolution problem would be to use a gradient-based optimization procedure. For example, the high-resolution image  $\mathbf{X}$  can be generated, considering a gradient-descendent approach, using the following iterative rule:

$$\mathbf{X}_{n+1} = \mathbf{X}_n + \delta \mathbf{G}(\mathbf{X}_n) \quad (3.16)$$

where  $\mathbf{X}_n$  and  $\mathbf{X}_{n+1}$  are the estimates of the high-resolution image  $\mathbf{X}$  for the iterations  $n$  and  $n+1$  respectively, while  $\mathbf{G}$  is the gradient of the cost function  $F$  and  $\delta$  is a scale factor defining the step size in the direction of the gradient. In fact, the optimization scheme presented in Eq. (3.16) is used in [83] for the obtention of high-resolution images, but only considering a ML formulation of the super-resolution problem.

In the following sections, and due to the importance of having an analytical expression for the gradient of the cost function  $F$ , two expressions of the gradient, each one considering one of the two prior terms previously introduced, will be presented. Also, an alternative method for estimating the data term (corresponding to the gradient of the similarity cost) in both gradients is introduced.

### 3.4.1 Gradient for MAP cost function with Laplacian prior

The MAP cost function with a Laplacian prior ( $F_l$ ) is constructed by replacing the definition of the Laplacian prior  $A_l(\mathbf{X})$  given by Eq. (3.14) into the general expression previously obtained for the cost function  $F$  in Eq. (3.13). The result obtained after this replacement is shown below:

$$F_l = \sum_{k=1}^N \|\mathbf{W}_k \mathbf{X} - \mathbf{Y}_k\|_2^2 + \lambda \|\Gamma_l \mathbf{X}\|_2^2 \quad (3.17)$$

Thus, an expression for the gradient of the MAP cost function with a Laplacian prior ( $\mathbf{G}_l$ ) can be obtained by differentiating  $F_l$  with respect to  $\mathbf{X}$ :

$$\begin{aligned} \mathbf{G}_l &= \frac{\partial F_l}{\partial \mathbf{X}} \\ &= \frac{\partial}{\partial \mathbf{X}} \left( \sum_{k=1}^N \|\mathbf{W}_k \mathbf{X} - \mathbf{Y}_k\|_2^2 + \lambda \|\Gamma_l \mathbf{X}\|_2^2 \right) \\ &= \sum_{k=1}^N \mathbf{W}_k^T (\mathbf{W}_k \mathbf{X} - \mathbf{Y}_k) + \lambda \Gamma_l^T \Gamma_l \mathbf{X} \end{aligned} \quad (3.18)$$

### 3.4.2 Gradient for MAP cost function with gradient prior

The MAP cost function with a gradient prior ( $F_g$ ) is constructed by replacing the definition of the gradient prior  $A_g(\mathbf{X})$  given by Eq. (3.15) into the general expression previously obtained

for the cost function  $F$  in Eq. (3.13). The result obtained after this replacement is shown below:

$$F_g = \sum_{k=1}^N \|\mathbf{W}_k \mathbf{X} - \mathbf{Y}_k\|_2^2 + \lambda \|\nabla \mathbf{X}\|_1 \quad (3.19)$$

Thus, an expression for the gradient of the MAP cost function with a gradient prior ( $\mathbf{G}_g$ ) can be obtained by differentiating  $F_g$  with respect to  $\mathbf{X}$ :

$$\begin{aligned} \mathbf{G}_g &= \frac{\partial F_g}{\partial \mathbf{X}} \\ &= \frac{\partial}{\partial \mathbf{X}} \left( \sum_{k=1}^N \|\mathbf{W}_k \mathbf{X} - \mathbf{Y}_k\|_2^2 + \lambda \|\nabla \mathbf{X}\|_1 \right) \\ &= \sum_{k=1}^N \mathbf{W}_k^T (\mathbf{W}_k \mathbf{X} - \mathbf{Y}_k) + \lambda \nabla^T \text{sign}(\nabla \mathbf{X}) \end{aligned} \quad (3.20)$$

### 3.4.3 Zomet's method

An approximate method for computing the common term of  $\mathbf{G}_l$  and  $\mathbf{G}_g$  is proposed by *Zomet et al.* in [84]. This term, which will be denoted as  $\mathbf{G}_{\text{data}}$ , represents the derivative of the data term of the cost function  $F$  with respect to  $\mathbf{X}$  and is given by:

$$\mathbf{G}_{\text{data}} = \sum_{k=1}^N \mathbf{W}_k^T (\mathbf{W}_k \mathbf{X} - \mathbf{Y}_k) = \sum_{k=1}^N \mathbf{P}_k \quad (3.21)$$

where the notation  $\mathbf{P}_k \equiv \mathbf{W}_k^T (\mathbf{W}_k \mathbf{X} - \mathbf{Y}_k)$  was introduced. In this sum, the term  $(\mathbf{W}_k \mathbf{X} - \mathbf{Y}_k)$ , that represents the difference between the low-resolution version of the high-resolution image estimate ( $\mathbf{W}_k \mathbf{X}$ ) and one of the low-resolution images ( $\mathbf{Y}_k$ ), is back-projected in the high-resolution pixel grid by its multiplication with  $\mathbf{W}_k^T$ . This is the reason why the term  $\mathbf{P}_k$  is usually called back-projected difference image.

In order to introduce robustness in the optimization procedure, this method suggests to compute an estimate of  $\mathbf{G}_{\text{data}}$  as a scaled pixel-wise median of the set of  $N$  back-projected difference images:

$$\mathbf{G}_{\text{data}} \approx N \cdot \text{median}(\mathbf{P}_1, \dots, \mathbf{P}_N) \equiv \mathbf{G}_{\text{data}}^Z \quad (3.22)$$

The fundamental idea behind this method is that the median can approximate the mean quite accurately if a sufficient set of low-resolution images is provided. Therefore, since

the median is much more robust than the mean if distant outliers are present in the set of low-resolution images, the utilization of Zomet’s approximation is useful to obtain accurate results when noise and other distorting effects are present. Based on this approach, two new alternative expressions for the gradients  $\mathbf{G}_l$  and  $\mathbf{G}_g$  can be established as it follows:

$$\mathbf{G}_l^Z = \mathbf{G}_{data}^Z + \lambda \mathbf{\Gamma}_l^T \mathbf{\Gamma}_l \mathbf{X} = N \cdot \text{median}(\mathbf{P}_1, \dots, \mathbf{P}_N) + \lambda \mathbf{\Gamma}_l^T \mathbf{\Gamma}_l \mathbf{X} \quad (3.23)$$

$$\mathbf{G}_g^Z = \mathbf{G}_{data}^Z + \lambda \mathbf{\nabla}^T \text{sign}(\mathbf{\nabla} \mathbf{X}) = N \cdot \text{median}(\mathbf{P}_1, \dots, \mathbf{P}_N) + \lambda \mathbf{\nabla}^T \text{sign}(\mathbf{\nabla} \mathbf{X}) \quad (3.24)$$

### 3.5 Image registration

In the context of multi-frame super-resolution, registration represents a preliminary step required to estimate the relative displacements between each one of the low-resolution images. The basic idea is to find a motion model, represented by a geometric transformation, that relates each low-resolution image to one of the images previously selected as the reference (in order to use its pixel grid as the common coordinate system).

One of the simplest approaches to find an estimation of the registration parameters that describe the motion model relating two images is to minimize the degree of dissimilarity between these two images. This can be performed using the Sum of Squared Differences (SSD) as a dissimilarity measure, in order to quantify how different two images are. Thus, image registration can be posed as another optimization problem (the previous one was multi-frame super-resolution) where a solution can be obtained using any gradient-based minimization scheme.

In this section, the mathematical formulation of the image registration problem is presented, where the minimization of a functional defined by the SSD between two images is required to have an estimation of the registration parameters. Since it is expected to employ this registration procedure using a gradient-based minimization method, the derivation of an expression for the gradient of the SSD with respect to the registration parameters is also presented.

For the motion models, two cases were considered: affine and quadratic transformations (with 6 and 12 degrees of freedom respectively), which are the tools used to describe the motion relations between low-resolution images. The purpose of having two motion models in the context of multi-frame super-resolution is to figure out if the use of a more complex model (represented by the quadratic transformation, in comparison with the affine one) can help dealing with the distortion effects that degrade the quality of the low-resolution images, since these distortions tend to severely affect the results of the image registration procedures.

### 3.5.1 Registration using sum of squared differences

Let  $\mathbf{I}$  and  $\mathbf{T}$  be matrices with a size of  $m \times n$  representing the current image (this is, the image that is expected to be registered) and the reference (or template) image respectively. Let  $x$  and  $y$  be the possible pixel coordinates of these images, meaning that  $(x, y) \in \{1, 2, \dots, m\} \times \{1, 2, \dots, n\}$ . And let  $\omega(\mathbf{p}, x, y)$  be a transformation function (affine, quadratic, etc) defined in terms of the elements of the vector  $\mathbf{p}$  that maps pixel positions  $(x, y)$  from the template to the current image. The pixel with position  $(x, y)$  in the image  $\mathbf{T}$  should have the same value of the pixel with position  $\omega(\mathbf{p}, x, y)$  in the image  $\mathbf{I}$ , which simply means that  $\mathbf{T}(x, y) = \mathbf{I}(\omega(\mathbf{p}, x, y))$ .

Moreover, the SSD between the current and the template image can be expressed, as function of the vector  $\mathbf{p}$  of the transformation  $\omega$ , as follows:

$$\text{SSD}(\mathbf{p}) = \sum_{(x,y)} \left( \mathbf{T}(\omega(\mathbf{p}, x, y)) - \mathbf{I}(x, y) \right)^2 \quad (3.25)$$

where the sum is over all the possible pixel positions  $(x, y)$ . Since the SSD corresponds to a dissimilarity measure, whose value is minimum when the images are as similar as possible, the registration procedure can be formulated as the minimization problem:

$$\hat{\mathbf{p}} = \underset{\mathbf{p}}{\text{ArgMin}} \left[ \sum_{(x,y)} \left( \mathbf{T}(\omega(\mathbf{p}, x, y)) - \mathbf{I}(x, y) \right)^2 \right] \quad (3.26)$$

where  $\hat{\mathbf{p}}$  is the estimate of the vector  $\mathbf{p}$  that defines the transformation  $\omega(\mathbf{p}, x, y)$  that represents the geometric transform expected to be obtained after performing a registration task.

### 3.5.2 Optimization of registration based on SSD

As was mentioned before, if the minimization of a functional is required, the derivation of an analytical expression of its gradient is a fundamental step. Then, in order to find a solution for Eq. (3.26), the gradient of the SSD with respect to  $\mathbf{p}$  ( $\mathbf{G}_{\text{ssd}}$ ) must be calculated as is presented below:

$$\begin{aligned}
\mathbf{G}_{\text{ssd}} &= \frac{\partial \text{SSD}}{\partial \mathbf{p}} \\
&= \frac{\partial}{\partial \mathbf{p}} \left( \sum_{(x,y)} \left( \mathbf{T}(\boldsymbol{\omega}(\mathbf{p}, x, y)) - \mathbf{I}(x, y) \right)^2 \right) \\
&= 2 \sum_{(x,y)} \left( \mathbf{T}(\boldsymbol{\omega}(\mathbf{p}, x, y)) - \mathbf{I}(x, y) \right) \frac{\partial}{\partial \mathbf{p}} \left( \mathbf{T}(\boldsymbol{\omega}(\mathbf{p}, x, y)) \right) \\
&= 2 \sum_{(x,y)} \left( \mathbf{T}(\boldsymbol{\omega}(\mathbf{p}, x, y)) - \mathbf{I}(x, y) \right) \left( \nabla \mathbf{T} \frac{\partial \boldsymbol{\omega}}{\partial \mathbf{p}} \right)^T
\end{aligned} \tag{3.27}$$

where  $\nabla \mathbf{T}$  is the gradient of the image  $\mathbf{T}$  and  $\frac{\partial \boldsymbol{\omega}}{\partial \mathbf{p}}$  is the partial derivative of the transformation  $\boldsymbol{\omega}$  with respect to the vector  $\mathbf{p}$ . Under the assumption that  $\mathbf{p}$  is a vector of  $N$  elements, then term  $\nabla \mathbf{T} \frac{\partial \boldsymbol{\omega}}{\partial \mathbf{p}}$  will be a matrix of size  $1 \times N$  (row vector) and will have the following form:

$$\begin{aligned}
\nabla \mathbf{T} \frac{\partial \boldsymbol{\omega}}{\partial \mathbf{p}} &= \begin{pmatrix} \frac{\partial T}{\partial x} & \frac{\partial T}{\partial y} \end{pmatrix} \begin{pmatrix} \frac{\partial \omega_x}{\partial p_1} & \cdots & \frac{\partial \omega_x}{\partial p_N} \\ \frac{\partial \omega_y}{\partial p_1} & \cdots & \frac{\partial \omega_y}{\partial p_N} \end{pmatrix} \\
&= \begin{pmatrix} \frac{\partial T}{\partial x} \frac{\partial \omega_x}{\partial p_1} + \frac{\partial T}{\partial y} \frac{\partial \omega_y}{\partial p_1} & \cdots & \frac{\partial T}{\partial x} \frac{\partial \omega_x}{\partial p_N} + \frac{\partial T}{\partial y} \frac{\partial \omega_y}{\partial p_N} \end{pmatrix}
\end{aligned} \tag{3.28}$$

### 3.5.3 Registration of affine transformations

In the case of affine transformations, the vector  $\mathbf{p}$  has 6 elements (degrees of freedom) and the transform function  $\boldsymbol{\omega}$  takes the form:

$$\boldsymbol{\omega}_a(x, y) = ( p_1x + p_2y + p_3, p_4x + p_5y + p_6 ) \tag{3.29}$$

which implies that the term  $\nabla \mathbf{T} \frac{\partial \boldsymbol{\omega}}{\partial \mathbf{p}}$  will be given, in this case, by the following expression:

$$\begin{aligned}
\nabla \mathbf{T} \frac{\partial \boldsymbol{\omega}_a}{\partial \mathbf{p}} &= \begin{pmatrix} \frac{\partial T}{\partial x} & \frac{\partial T}{\partial y} \end{pmatrix} \begin{pmatrix} \frac{\partial \omega_{a,x}}{\partial p_1} & \cdots & \frac{\partial \omega_{a,x}}{\partial p_6} \\ \frac{\partial \omega_{a,y}}{\partial p_1} & \cdots & \frac{\partial \omega_{a,y}}{\partial p_6} \end{pmatrix} \\
&= \begin{pmatrix} \frac{\partial T}{\partial x} & \frac{\partial T}{\partial y} \end{pmatrix} \begin{pmatrix} x & y & 1 & 0 & 0 & 0 \\ 0 & 0 & 0 & x & y & 1 \end{pmatrix} \\
&= \begin{pmatrix} \frac{\partial T}{\partial x}x & \frac{\partial T}{\partial x}y & \frac{\partial T}{\partial x} & \frac{\partial T}{\partial y}x & \frac{\partial T}{\partial y}y & \frac{\partial T}{\partial y} \end{pmatrix}
\end{aligned} \tag{3.30}$$

Thus, the replacement of Eq. (3.30) into Eq. (3.27) yields the expression for the gradient of the SSD when an affine transform is considered to represent the motion model in the registration problem.

### 3.5.4 Registration of quadratic transformations

In the case of quadratic transformations, the vector  $\mathbf{p}$  has 12 elements (degrees of freedom) and the transform function  $\omega$  takes the form:

$$\omega_q(x, y) = ( p_1x + p_2y + p_3x^2 + p_4y^2 + p_5xy + p_6, p_7x + p_8y + p_9x^2 + p_{10}y^2 + p_{11}xy + p_{12} ) \quad (3.31)$$

which implies that the term  $\nabla \mathbf{T} \frac{\partial \omega}{\partial \mathbf{p}}$  will be given, in this case, by the following expression:

$$\begin{aligned} \nabla \mathbf{T} \frac{\partial \omega_q}{\partial \mathbf{p}} &= \begin{pmatrix} \frac{\partial T}{\partial x} & \frac{\partial T}{\partial y} \end{pmatrix} \begin{pmatrix} \frac{\partial \omega_{q,x}}{\partial p_1} & \dots & \frac{\partial \omega_{q,x}}{\partial p_{12}} \\ \frac{\partial \omega_{q,y}}{\partial p_1} & \dots & \frac{\partial \omega_{q,y}}{\partial p_{12}} \end{pmatrix} \\ &= \begin{pmatrix} \frac{\partial T}{\partial x} & \frac{\partial T}{\partial y} \end{pmatrix} \begin{pmatrix} x & y & x^2 & y^2 & xy & 1 & 0 & 0 & 0 & 0 & 0 & 0 \\ 0 & 0 & 0 & 0 & 0 & 0 & x & y & x^2 & y^2 & xy & 1 \end{pmatrix} \\ &= \begin{pmatrix} \frac{\partial T}{\partial x}x & \frac{\partial T}{\partial x}y & \frac{\partial T}{\partial x}x^2 & \frac{\partial T}{\partial x}y^2 & \frac{\partial T}{\partial x}xy & \frac{\partial T}{\partial x} & \frac{\partial T}{\partial y}x & \frac{\partial T}{\partial y}y & \frac{\partial T}{\partial y}x^2 & \frac{\partial T}{\partial y}y^2 & \frac{\partial T}{\partial y}xy & \frac{\partial T}{\partial y} \end{pmatrix} \end{aligned} \quad (3.32)$$

Thus, the replacement of Eq. (3.32) into Eq. (3.27) yields the expression for the gradient of the SSD when a quadratic transform is considered to represent the motion model in the registration problem.

# Chapter 4

## Astronomical images and super-resolution

In this chapter, an overview about the aspects of astronomical images that should be considered under the perspective of multi-frame super-resolution is presented. It begins with a brief description of the process by which astronomical images are acquired, to then discuss the content that can be found in these images, considering two simple categories to classify the signals from astronomical sources. The two main types of noise and distortions that affect the quality of astronomical images are also reviewed. Then, a description of survey images based on two particular features that characterize this specific kind of astronomical images is presented.

Finally, we introduce two relevant parameters which are employed to describe, in a broad manner, the quality on an astronomical image: the Point-Spread Function (PSF) and the Signal-to-Noise Ratio (SNR). These two parameters are used to quantify the degree of blur degradation and noise corruption that affect an astronomical image during its acquisition. Both parameters, which can be estimated using astronomical software, play an important role in multi-frame super-resolution, since they represent a quantification of these two degrading effects which are considered in the Image Observation Model (IOM).

### 4.1 General description of astronomical images

In this section, a brief overview about the process of acquisition of astronomical images is presented. A simple classification of the sources that can be found in this type of images is also introduced. Finally, some of the distortion effects and the different kinds of noise that are present in astronomical images are reviewed.

### 4.1.1 Acquisition of astronomical images

The fundamental technology behind astronomical imaging is the Charge-Coupled Device (CCD), which has been the standard device for astronomical image acquisition since the 1980s. A CCD detector consists, basically, of an array of pixels, usually arranged in a square shape, located at the focal plane of an optical instrument such as a telescope. Each pixel is a circuit element covered in silicon, which is very sensitive to light, and which bases its operation on the photoelectric effect<sup>1</sup>.

When a CCD receives light, photons will reach the pixels in the detector and will then be transformed into electronic charge, which will induce a voltage in the circuit (see the diagram presented in Figure 4.1). The Analog-to-Digital (A/D) electronics measure the voltage created by these electrons at the serial output and turn this voltage into an electronic number, which can then be digitally transmitted and saved to a computer. ADU (Analog-to-Digital Unit) is the name given to the A/D electronics output units. Therefore, in an astronomical image, the value of a pixel represents essentially a number of ADU units, and these ADU units represent the amount of photons that reached this specific pixel during the process of image acquisition (which can be very long, in order to capture a suitable number of photons).

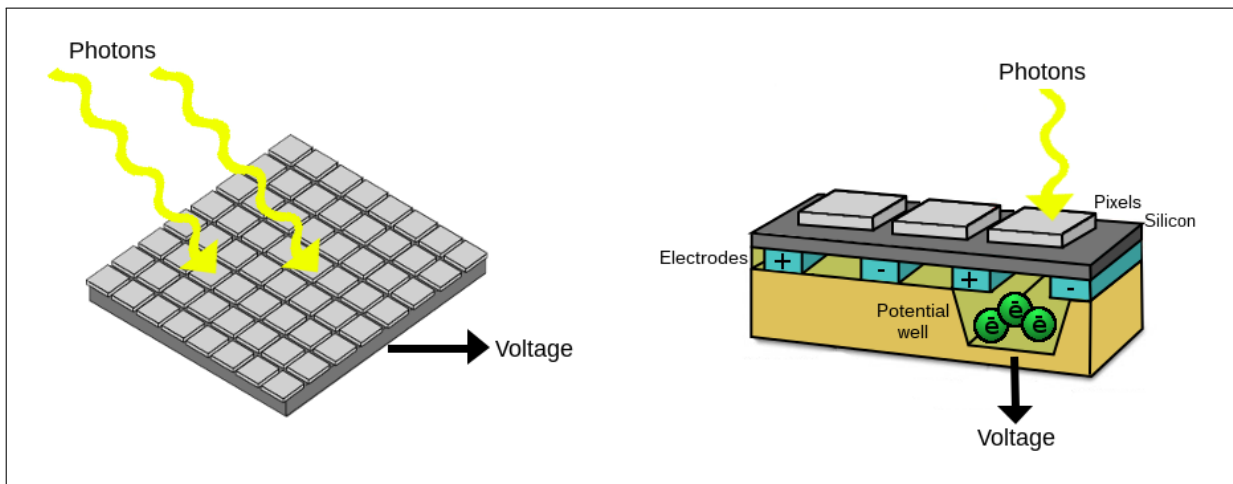


Figure 4.1: CCD detector and its mechanism of operation.

Before performing analyses over them, astronomical images acquired by a CCD detector must be calibrated, following a correction process known as *reduction*. A reduced astronomical image is obtained through the following steps: first, a dark field is subtracted from the original (raw) image. A dark field is a 0-second exposure image, taken on the same CCD that will be used to obtain the astronomical images. This dark field exhibits the dark current of the CCD, which corresponds to the spontaneous electrons generated by thermal excitation on the CCD chip. If the dark current is not removed, voltage corresponding to thermal processes within the CCD will be incorrectly considered as signal from the observed astronomical objects.

<sup>1</sup>The photoelectric effect is the physical observation that many metals emit electrons when light shines upon them. Electrons emitted in this manner are usually called photoelectrons.

The second step in the reduction process corresponds to a division between the image obtained after the subtraction of the dark field from the raw image, and a flat field image. A flat field image is another special kind of image, obtained with the same CCD detector. In this case, an image of an homogeneous light field (which can be generated artificially using a lamp and a backdrop, or naturally with an image of the sky during sunset or sunrise) must be used to account for the different sensitivities to light of the CCD pixels. On an ideal CCD, all pixels would present the same sensitivity to light, and would convert photons to electrons in the same, fixed rate. In reality, this is not the case. Dividing the images for this flat field serves as a normalization of pixel light sensitivity, and also partially corrects optical defects from the imaging device.

### 4.1.2 Source characterization

The content of astronomical images can be characterized in terms of the photon sources, or signals, that are present in them. The two main photon sources, which have an influence over the content of this sort of images, are the background and the astronomical objects.

The background represents the light contribution of the sky in an astronomical image. Usually, the background is reflected in the images as a fixed constant that is present in all the pixels; thus, the background can be estimated and removed by subtracting this constant from all the image pixels. In more complex cases, the background can not be easily removed, since gradients or more complicated behaviors may be influencing it.

Background subtraction makes it possible to easily detect the actual astronomical objects. Typically, photon emissions from astronomical objects are not readily distinguished from the background, thus they can be properly detected only after background subtraction and within an error range. In the most generic definition, two types of astronomical sources can be identified in an image: *point and extended sources*. A brief and simple characterization of each one of these sources in the context of astronomical images is described below.

In an ideal approach, stars would be modeled as point sources due to their far location, and they would appear as a single pixel in the image (in the context of this non-rigorous classification, “star” represents every astronomical object which, due to its far location, does not permit to obtain a notion of its shape). Evidently, this does not happen in practice. Many factors can affect the path of a photon from the astronomical object to the pixels of a CCD detector but, in ground-based telescopes, the influence of the atmosphere is the most relevant one. Since the atmosphere is a turbulent layer that surrounds the Earth, each photon that crosses the atmosphere will be scattered, meaning that the shape of a wave front of photons hitting the CCD will be modified. The atmospheric effects can be regarded as the application of a blur operator over the original, non-perturbed astronomical objects and this is why, in an astronomical image, a star appears as a circle in terms of shape, and as a narrow peak in terms of intensity (high values spanning over a reduced amount of pixels).

On the other hand we have extended sources, which are all the objects whose shape can be noticed by a telescope, such as galaxies, and thus they can not be considered simply as point sources in the sky. Even under ideal assumptions, photons from these extended sources

will reach a group of contiguous pixels on the CCD detector, spanning an area of the image. Atmospheric effects also tend to modify the real shape of this type of objects. In astronomical images, these objects usually show elliptical shapes, while their intensity curves are soft and span over a group of adjacent pixels.

### 4.1.3 Noise sources in astronomical images

Noise is one of the undesirable effects always present in astronomical images, and its diminution is required in order to improve the quality of the images. The two main sources of noise are reviewed below.

1. Shot noise: This type of noise is caused by the arrival of random photons to the CCD pixels. Since the arrival of each photon is an independent event (not determined by any previous arrival), there is no way to accurately predict the arrival of any of these photons. In probabilistic terms, this physical process is modeled by a Poisson distribution. If we consider a large enough image acquisition time, this random photon arrival process can be approximated by a normal distribution, which means that the shot noise effects will be smaller as the image exposure time increases (since more photons are collected). Another mechanism to deal with this type of noise is to combine images, by stacking them in one new image, which is essentially another form of increasing the image exposure time.
2. Read-out noise: CCD electronics do not measure the amount of charge in each packet of electrons perfectly. They add a slight amount of uncertainty, or noise, as they perform the measurement process, due to the different electronic procedures. This sort of noise exhibits a Gaussian distribution and its influence on astronomical images can be reduced by combining frames or using the standard image processing techniques for noise removal.

In a first instance, the main concern in the context of multi-frame super-resolution is the removal of read-out noise, since the Gaussian distribution of this type of noise coincides with the assumptions considered in the image observation model and in the MAP approach. This fact justifies the suitability of multi-frame super-resolution reconstruction techniques for the case of astronomical images. However, the utilization of a set of low-resolution images helps to deal with the presence of shot and read-out noise, since the combination of the information contained in each low-resolution image reduces the presence of both types of noise in the reconstructed image. Besides, the utilization of the Laplacian and the gradient prior terms in the cost function also permits to diminish the noise effects.

### 4.1.4 Distortions

There are many sources of distortion in the process of astronomical image acquisition. Some of them have already been mentioned, but now they will be reviewed in more detail and context. Distortions are mainly a consequence of technical issues with the CCD detector, but sometimes they can be caused by natural and random events that can not be controlled.

Below, four of the main distortion sources that affect astronomical images are listed:

1. Dark current: Dark current is caused by thermally generated electrons which, when the voltage is measured, are confused with electrons generated by actual photon arrivals to the CCD pixels. The rate of dark current aggregation depends on the temperature of the CCD during the image acquisition process; this is why, in telescopes, liquid nitrogen is used to cool down the CCDs and decrease the effects of dark current. Fortunately, as was previously mentioned, the noise introduced to an image by dark current is removed in the image reduction process.
2. Non-uniform sensitivity in pixels: The pixels of a CCD often show different sensitivities to light, which represents a problem in order to acquire an image in the most accurate way possible. Each pixel will have a different conversion rate of photons into electrons. This distortion effect can be reduced, as was previously mentioned, by dividing the astronomical image by a flat-field image, in order to normalize the light sensitivity scale of the pixels.
3. Bad pixels: Sometimes, there are pixels on the CCD that do not work properly; other times, an operative pixel stops working properly due to saturation (after receiving a limit amount of photons, the pixel's behavior stops being linear, which means that the photon value established for that pixel is not reliable). Thus, it is important to accurately detect the location of defective pixels on the CCD, in order to remove them from the final image. Usually, these pixels are replaced considering some sort of interpolation based on the values of the surrounding pixels, such as a mean or a median interpolation.
4. Hot pixels: When a high energy particle hits one pixel in the CCD, it loses its energy by colliding with the atoms of the circuit. In this collision, many electrons are liberated, which causes a high electron count and thus a bright spot on the image (a pixel with a very high intensity value). These high energy particles can be genuine cosmic rays (exotic particle produced by exploding supernovae, black holes, etc), or can be also produced by the decay of some radioactive atoms present in the lenses just above the CCD. Cosmic rays are usually easy to recognize, because they appear much sharper than stars: the high energy particle hits just one or a couple of pixels. The removal of these pixels can be tricky but it is usually based, as the previous case, on interpolation procedures.

In regards to multi-frame super-resolution, dark current and non-uniform sensitivity in pixels are not a problem, since the low-resolution images that are considered in this thesis have already been reduced. Eventually, images with bad or hot pixels can be considered in some cases, but the presence of these outlier pixels is handled by the super-resolution algorithms themselves, due to their regularized approach. If there is an outlier in one of the low-resolution images, its presence is compensated by the correct data contained in the other low-resolution images. In case this is not enough, the penalization introduced by the prior term in the cost function helps to remove the outlier value.

## 4.2 Survey images

As was previously mentioned, survey images represent one of the most interesting set of images where multi-frame super-resolution techniques can be applied. In this specific type of astronomical images, all the descriptions presented above are also valid. Nevertheless, there are characteristics particular to these images which will now be addressed.

Since the main idea of surveys is to observe wide areas of the sky and to not concentrate the observation in one specific astronomical object, in each survey image a great number of astronomical objects can be found. These objects, considering the simple source characterization previously introduced, can mostly have circular and sharp shapes (corresponding mainly to stars, but also to other types of objects located very far), or elliptical and smooth shapes (corresponding mainly to galaxies). Also, since no object has a predominance in this kind of images, there is a large amount of background pixels in each survey image. Then, and due to the background subtraction employed to enable the proper identification of astronomical objects, these background pixels will have an intensity value of zero if the image is properly calibrated. This means that survey images, when understood as matrices, will have a high degree of sparsity.

Figure 4.2 shows an example of the images that are expected to be obtained using the LSST. This image was generated by the LSST team considering all the real circumstances that affect the process of image acquisition. Also, in this image, two main characteristics of survey images that were mentioned above can be noted: the presence of a big number of objects, with both sharp circle and smooth elliptical shapes, and a large amount of background pixels.

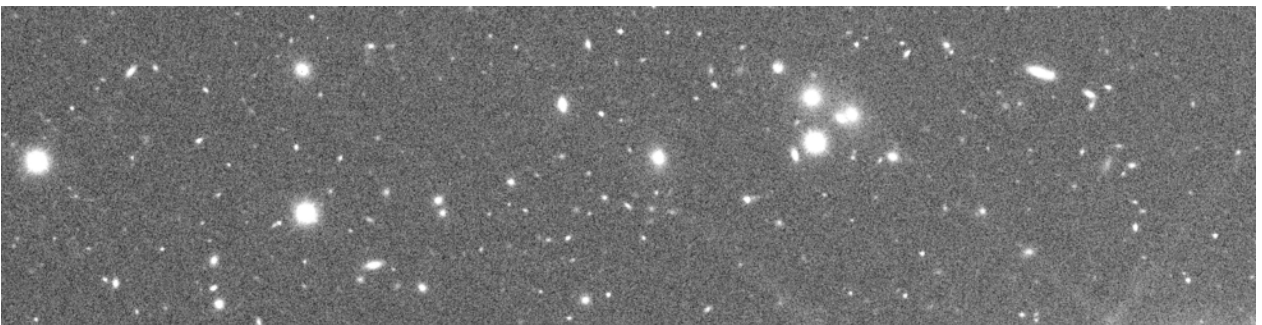


Figure 4.2: This simulated image, generated by the LSST team, represents an example of the type of images that will be obtained by the LSST.

## 4.3 Relevant characteristics in the context of multi-frame super-resolution

In the context of multi-frame super-resolution, there are two main elements used to describe some characteristics of astronomical images that need to be considered. These elements are the Point-Spread Function (PSF) and the Signal-to-Noise Ratio (SNR), which are typically

employed to measure, or have a notion, of the quality of the information contained in an astronomical image.

The importance of both elements comes from the fact that they are used for describing, in mathematical terms, two relevant characteristics of astronomical images and which are part of the conceptualization introduced for multi-frame super-resolution: the blur and the noise. For astronomers, the blur that affects the quality of an image is modeled by the PSF, while the amount of noise that corrupts an image is quantified employing the SNR.

### 4.3.1 Point-Spread Function (PSF)

In the context of optical astronomical imaging, the PSF represents the atmospheric effects that disturb the quality of an image during acquisition as a convolution kernel. In practice, however, there are other elements that should be considered in order to have a detailed description of the PSF, such as the light dispersion on the detector and tracking errors. There is no way to know the PSF exactly, since it changes in time and space as the turbulences of the atmosphere move around and change (the PSF can be different for two different pixels in the same time and can be also different for the same pixel in two different moments). Therefore, in practice, astronomers work with approximations of the PSF.

A simple approach for PSF modeling is considering it as a 2D Gaussian kernel. The parameters of this kernel are estimated through the following process:

1. Selection of a set of suitable stars in an astronomical image, which means that the shape of these stars should be well defined in such image (for example, they should not present diffraction spikes<sup>2</sup>).
2. Estimation of the FWHM<sup>3</sup> and the ellipticity for every selected star in the image after fitting a 2D Gaussian.
3. The average of the obtained values actually represents the FWHM and the ellipticity of the PSF in the image (since stars should be point sources).

Then, using the estimated values for the FWHM and the ellipticity of the PSF, the 2D Gaussian kernel can be constructed. This procedure can be performed employing two computational tools developed for processing and analyzing astronomical images: SExtractor [5] and PSFEx [4]. The first one is used to select the required set of stars, while the second one uses this set of stars to estimate the FWHM and the ellipticity of the PSF according to the procedure previously described.

As ellipticity values are usually close to zero, the 2D Gaussian approximation of the PSF can be generated using the same standard deviation for the Gaussian in both axes. This stan-

---

<sup>2</sup>Diffraction spikes are lines radiating from bright light sources in reflecting telescope images. They are artifacts caused by light diffracting around the support vanes of the secondary mirror of the telescope.

<sup>3</sup>The Full Width at Half Maximum (FWHM) is a parameter commonly used to describe the width of a bump on a curve or function. It is given by the distance between the points on the function at which it reaches the half of its maximum value. In an astronomical context, the FWHM is used to have an estimation of the width of the kernel that represents the PSF.

standard deviation is obtained from the existing relation between the FWHM and the standard deviation in Gaussian functions. This relation, which is depicted in Figure 4.3, is given by:

$$\text{FWHM} = 2 \sqrt{2 \ln(2)} \sigma \approx 2.355 \sigma \quad (4.1)$$

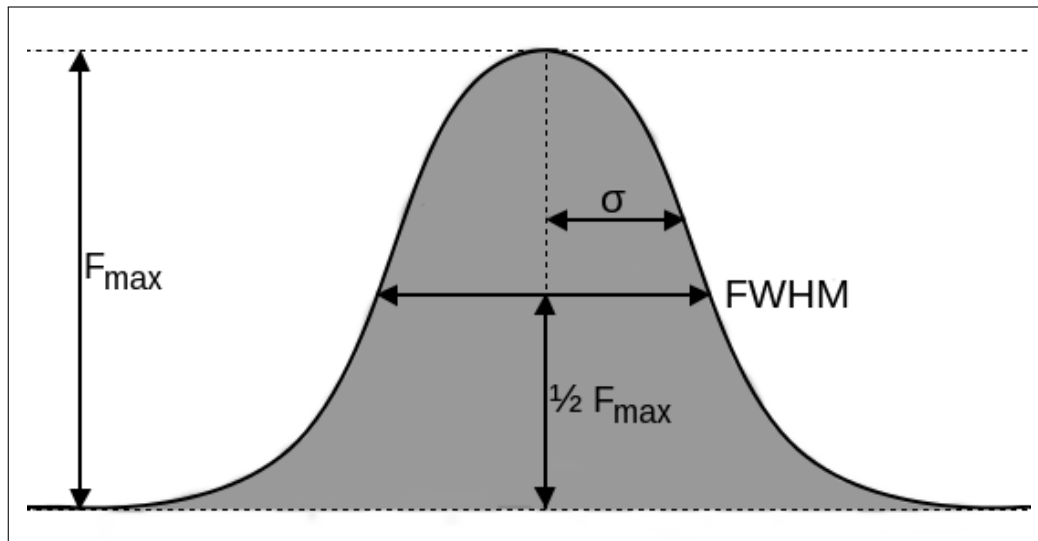


Figure 4.3: Relation between the FWHM and the standard deviation in a Gaussian function.

Therefore, this 2D Gaussian approximation of the PSF is useful to estimate the quality of an astronomical image. For larger values of the FWHM or, equivalently, the standard deviation, the blur will affect the image more severely, but for smaller values, the blur will not affect the image quality in such a drastic way. This relation can be appreciated in Figure 4.4, where we can see some examples of how the quality of an astronomical image is blurred when it is convolved with a 2D Gaussian kernel for some set of FWHM values.

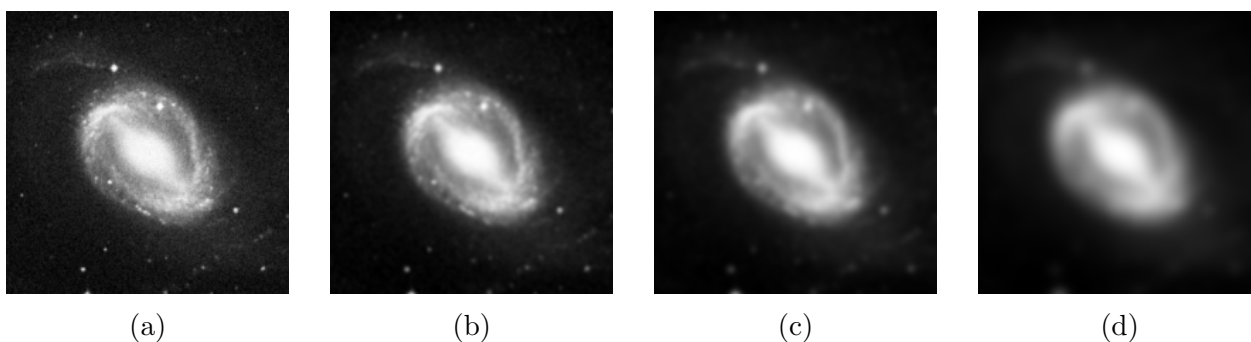


Figure 4.4: Results obtained from the convolution of an astronomical image (a) with 2D Gaussian kernels with FWHM values corresponding to 2.5 pixels, 5 pixels and 10 pixels are presented in (b), (c) and (d) respectively.

### 4.3.2 Signal-to-Noise Ratio (SNR)

The SNR relates the amount of useful information (signal coming from the actual astronomical objects) with the noise contained in an image. There are many different definitions for the SNR but, in this thesis, the following one will be used:

$$\text{SNR} = \frac{\text{Avg}(\text{signal})}{\sigma_{\text{noise}}} \quad (4.2)$$

where  $\text{Avg}(\text{signal})$  represents the average between the values of the pixels that contain signal, and  $\sigma_{\text{noise}}$  represents the standard deviation of the noise contained by the image considered. Every pixel whose intensity value is bigger than a threshold is considered as a pixel containing signal. This threshold value, which allows to separate the signal from the background pixels, can be computed using SExtractor.

The SNR then can be regarded as a measure of the quality of the image, since its value indicates the amount of noise present in an astronomical image. For example, a value close to 1 for the SNR means that there is a similar amount of noise and signal in the image, which precludes the proper identification and analysis of that signal. But a large value for the SNR means that there is a large amount of signal contained in the image compared to the amount of noise, and then this noise is not an impediment to identify the signal. All this can be seen in Figure 4.5, where some examples of astronomical images with different SNR values are shown.

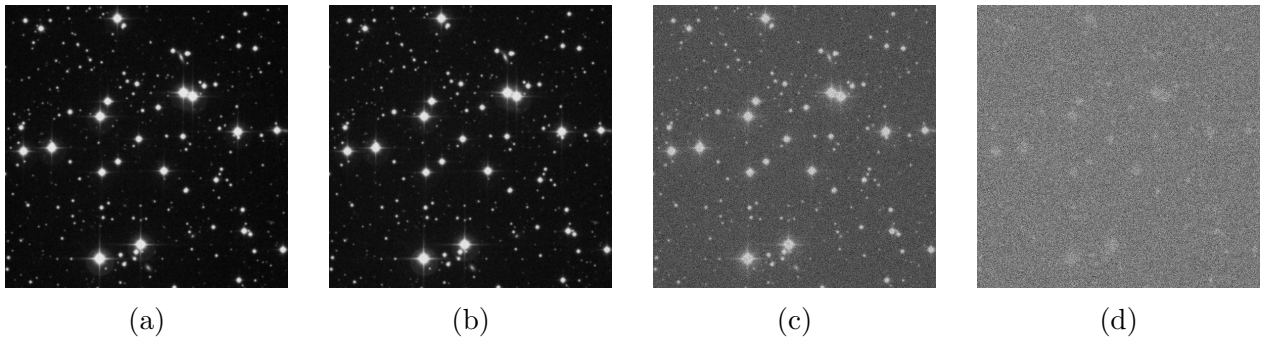


Figure 4.5: Results obtained from adding Gaussian noise to an astronomical image (a) until reaching SNR values corresponding to 100, 10 and 1, are presented in (b), (c) and (d) respectively.

# Chapter 5

## Experimental setting

In this chapter we describe, in a detailed manner, all the experiments that were carried out for analyzing the performance of the four multi-frame super-resolution algorithms, as function of the Signal-to-Noise Ratio (SNR), in order to achieve the different goals of this thesis. It is important to remember that these goals correspond to the following four points: (i) to find out the relation between the performance of each algorithm and the SNR, (ii) to determine which algorithm has the best performance, (iii) to analyze the reduction in the performance results of the algorithms when the estimation of the blur and registration parameters is not accurate, and (iv) to check if the employment of quadratic registration instead of affine registration for motion estimation implies an improvement in the performance of the algorithms.

In first place, we present a description of each one of the four multi-frame super-resolution algorithms in terms of the expressions, previously obtained for the cost functions and their corresponding gradients. After that, we discuss the relevant details about image simulation, since the experiments performed for this thesis are based on the utilization of simulated images generated with the Image Observation Model (IOM) and PhoSim. We also introduce the two metrics employed for measuring the algorithms' performance: the Peak Signal-to-Noise Ratio (PSNR) and the Reduced  $\chi^2$ .

With these concepts, we later discuss the details about each one of the experiments designed for studying the performance of the multi-frame super-resolution algorithms. These experiments are organized in two experimental frameworks, where the aim of each one is to analyze the algorithms' performance under different circumstances. In the first experimental framework (1EF), the algorithms employ the simulation parameters as input for recovering high-resolution images. This means that the blur and registration information of the simulated low-resolution images is known beforehand. Moreover, in the second experimental framework (2EF), the blur and registration parameters are estimated without knowing any prior information, as it should be done in practice. As consequence, the results obtained in the 2EF will be more realistic than the ones obtained in the 1EF, since, in this case, the performance of the algorithms will be affected by the errors introduced in the parameter estimation stage. In fact, the purpose of having these two frameworks is to be able of measuring the reduction, that should manifest the algorithms' performance, when the results obtained under an ideal setting, corresponding to the 1EF, are compared with the results obtained in

a more realistic context, such as the one established in the 2EF.

Finally, after introducing all the details concerning to both experimental frameworks, we present a brief discussion about some relevant technical aspects that are also required to have a comprehensive understanding about the different experiments performed in this thesis. Among these technical aspects we can mention the implementation details of the different algorithms considered in this thesis, such as the two registration procedures and the four multi-frame super-resolution algorithms, and the description of the computational infrastructure employed to carry out each one of the experiments.

## 5.1 Selected algorithms

In this thesis, the performance of four multi-frame super-resolution algorithms is analyzed as a function of the SNR value that describes the low-resolution images employed as input. These four algorithms, which were previously introduced and denoted as LA, LZ, GA and GZ, are defined as it follows:

- LA: Selection of Laplacian prior for the cost function, according to Eq. (3.17), and employment of the analytical expression for computing the corresponding gradient, which is specified by Eq. (3.18).
- LZ: Selection of Laplacian prior for the cost function, according to Eq. (3.17), and employment of Zomet's approximation for computing the corresponding gradient, which is specified by Eq. (3.23).
- GA: Selection of gradient prior for the cost function, according to Eq. (3.19), and employment of the analytical expression for computing the corresponding gradient, which is specified by Eq. (3.20).
- GZ: Selection of gradient prior for the cost function, according to Eq. (3.19), and employment of Zomet's approximation for computing the corresponding gradient, which is specified by Eq. (3.24).

Each one of these algorithms corresponds to one of the four possible combinations between the two priors (Laplacian and gradient) and the two expressions used for computing the gradient of the cost function (analytical expression and Zomet's approximation), which have already been presented in this thesis. The idea behind the selection of these algorithms is to combine all the available tools to approach the ill-posed nature of the super-resolution problem, as well as to deal with the noise which affects the set of low-resolution images (since this distortion element can severely affect the results of the super-resolution reconstruction procedure). Therefore, the evaluation of the algorithms' performance will allow us to determine which one of these tools turns out to be more effective in the context of multi-frame super-resolution.

It is important to mention explicitly what the expected utility, or reason of selection, is for each one of the considered tools. In first place, the use of prior terms intends to regularize the super-resolution problem, allowing algorithms to recover a high-resolution image in spite of the noise and the lack of complementary information in the set of low-resolution images.

Zomet's approximation offers a robust mechanism for computing the data term in the gradient and improve the optimization process, which represents another technique to deal with the presence of noise.

## 5.2 Image simulation

In order to evaluate the performance of the different multi-frame super-resolution algorithms as function of the SNR, multiple sets of low-resolution images were generated considering a range of values for the SNR. First, a set of 100 astronomical images was built, which were used as high-resolution image templates. Then, for each SNR value in the relevant range and for each one of the 100 high-resolution image templates, a set of 10 low-resolution images was generated, each one of these images having the corresponding SNR. This means that every high-resolution image template was degraded 10 times, considering random translations (vertical and horizontal shifts) with sub-pixel accuracy (satisfying the main condition required to use of multi-frame super-resolution procedures), and a given value for the SNR.

The simulation process, by which low-resolution images are obtained from the high-resolution image templates, was performed considering two different schemes which are described in later sections. In general terms, this simulation process can be summarized in the three following steps:

1. Selection of an astronomical image from the template set.
2. Degradation of that image 10 times, considering a random translations and a given value for the SNR.
3. Grouping these 10 simulated images, each one with the same SNR value, in one low-resolution set characterized by this SNR value and associated to the original image from the template set.

There are two more relevant parameters on the simulation process, which have not been mentioned: the downsampling factor and the PSF. The downsampling factor was established with a fixed value of 2 in all the simulations. This means that every simulated low-resolution image has a half of the resolution in each axis with respect to the high-resolution image template from which it was generated (then, the number of pixels in a low-resolution image is a quarter of the number of pixels in a high-resolution image template). The aspects related to the parametrization of the PSF effects are presented later, since each one of the two schemes considered employs a different approach for modeling the influence of the PSF in the simulation process.

The details concerning the construction of the set with high-resolution image templates are now discussed, which represents the main input for the simulation process. Then, each one of the two schemes used to carry out the simulation process are described. This description includes an explanation of how each one of these schemes handles the modeling of the PSF effects in the simulated images.

### 5.2.1 Construction of the template set

The set of high-resolution image templates was constructed with 100 cutouts obtained from astronomical images. Each cutout was manually obtained from a different astronomical image, since these cutouts must satisfy a special condition in order to be used in simulations of the low-resolution images to be employed as input for the multi-frame super-resolution algorithms. This condition is that each cutout must include at least one star, since the process used to estimate the value of the FWHM of the Gaussian approximation of the PSF, which was presented in Section 4.3.1, uses the stars contained in an image to operate.

The large amount of memory and processing time required by the algorithms to recover large images makes the repeated use of these algorithms infeasible if a complete astronomical image is employed. Since each algorithm needs to be used multiple times, cutouts with a size of  $200 \times 200$  pixels were considered for the template set in order to have faster runtimes and smaller memory consumption.

Therefore, if we expect to recover an image with a size of  $200 \times 200$  pixels from a set of 10 low-resolution images with a size of  $100 \times 100$  pixels, 10 matrices with a size of  $10,000 \times 40,000$  are needed to be stored in memory (corresponding to each one of the matrices  $\mathbf{W}_k$  considered in the IOM). Besides, the multiplication of these matrices is carried out several times during the optimization process, whenever a computation of the cost function or its gradient is performed. Consequently, performing the set of experiments considered in this thesis would not be possible for large images.

Some examples of the cutouts selected for the template set can be seen in Figures 4.4a, 4.5a and 5.1a. In each one of these examples we can notice the presence of the stars required for obtaining the Gaussian approximation of the PSF, whose FWHM represents a relevant parameter employed in the multi-frame super-resolution process. Moreover, and according to the source characterization previously introduced, we can see clear examples of extended sources in Figures 4.4a and 5.1a, since both images show galaxies, while in Figure 4.5a we can only see point sources that correspond to stars.

### 5.2.2 Simulations based in the image observation model

The first scheme used for simulating low-resolution images is based on the replication of the degradation process specified by the IOM. This means that each low-resolution image is generated by successively applying a random translation, a convolution with a Gaussian kernel (which, as previously mentioned, represents the approximation of the PSF), and a downsampling factor of two (meaning that every low-resolution pixel is obtained by averaging four high-resolution pixels) over the high-resolution image template, to finally add Gaussian noise in order to obtain a specific value for the SNR.

In this case, the PSF is parametrized in terms of the FWHM of its Gaussian approximation. The value used for the FWHM in all the simulations was 3.52 pixels, which is the value estimated for the FWHM of the Gaussian approximation of the PSF of the LSST. The mechanism used for the obtention of this value and the reasons for its use in this simulation

scheme based in the IOM are detailed in the next section.

### 5.2.3 PhoSim simulations

The second scheme used to simulate low-resolution images is based on the utilization of a new simulation tool called PhoSim [53], short for Photon Simulator. This tool, recently developed by the LSST team, uses a Monte Carlo approach to generate images by sampling photons from models of astronomical sources, and then simulating those photons through the system as they interact with the atmosphere, the telescope, and the camera. All the physical effects for optical light that determine the shapes, locations, and brightnesses of stars and galaxies are accurately represented by this image simulation tool.

Since PhoSim can use an image as input for the simulation process, this tool was employed using the images of the template set as input, considering the default configuration provided in PhoSim (that attempts to replicate the physical conditions under which the LSST will operate), in order to obtain their low-resolution versions. These simulated low-resolution images consider a wider range of distortions than the ones that can be modeled with the IOM.

In regards to the utilization of PhoSim, it is important to mention that we only had explicit control over the downsampling factor, which value was set to 2. A downsampling factor of 2 means the size of a pixel in a low-resolution image is twice the size (on both axes) of a pixel in a high-resolution image, thus, the area spanned by a pixel on a low-resolution image is 4 times the area spanned by a pixel on a high-resolution image. Although in theory the position of the simulated low-resolution images can also be defined, to then include the required translations that allow using multi-frame super-resolution algorithms, the atmospheric turbulence induced by PhoSim severely affects the final position of the images. This is not an impediment for using multi-frame super-resolution procedures, but it means that the registration parameters are not known beforehand for the simulated images.

The same situation happens with the SNR. While it is possible to simulate images considering a specific amount of photons, two images simulated according to the same sets of parameters will not have the exact same SNR, due to atmospheric turbulences and the Monte Carlo approach used by PhoSim, where each photon is generated by an individual process.

In this case, we do not have a mechanism for controlling the PSF, since its specific form is defined by a great deal of parameters and also by the random processes derived from the Monte Carlo approach. Because of this, an estimation of the FWHM of the PSF of the LSST is used, which corresponds to 3.52 pixels, in the first simulation scheme (that is based on the replication of the IOM). This will allow to compare the results obtained after performing multi-frame super-resolution reconstruction in sets of images generated with both simulation schemes.

The procedure employed to obtain this estimation of the value of the FWHM of the Gaussian approximation of the PSF of the LSST was the same that was presented in Section 4.3.1. In this case, a set of 100 simulated images, each one containing 10 stars in random

positions, was generated using PhoSim. Then, using SExtractor and PSFEx, the value for the FWHM of the PSF was calculated, obtaining an average value of 3.52 pixels (with an associated average value for the ellipticity of 0.02 pixels).

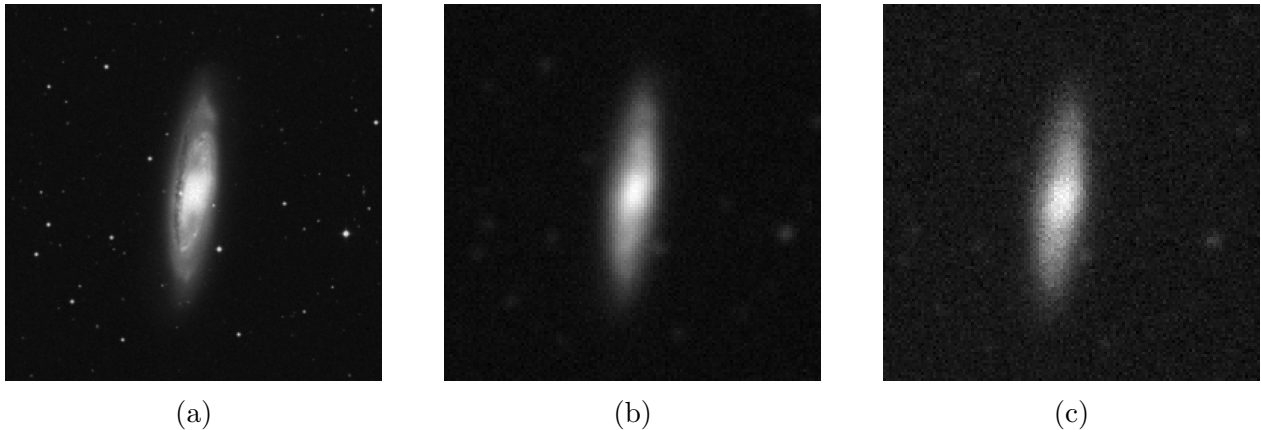


Figure 5.1: An example of the images of the template set is presented in (a), while the simulated low-resolution versions obtained using the IOM and PhoSim are presented in (b) and (c) respectively.

### 5.3 Performance metrics

The evaluation of the four multi-frame super-resolution algorithms was carried out considering two performance metrics. These metrics correspond to the Peak Signal-to-Noise Ratio (PSNR) and the Reduced  $\chi^2$ , and they were employed in the different experiments for measuring the performance achieved by each one of the algorithms. The purpose of the first metric is to compare the reconstructed high-resolution image with the template image used in the simulation process, while the idea behind the second metric is to compare how well the reconstructed image reflects the information contained in the set of low-resolution images used as input for the super-resolution process.

#### 5.3.1 Peak Signal-to-Noise Ratio (PSNR)

Since the performance of multi-frame super-resolution using simulations is to be analyzed, it is of interest to compare the image reconstructed using one of the algorithms with the original image, used as template in the simulation process. For this comparison, the PSNR was used, which is defined as:

$$\begin{aligned}
 \text{PSNR}(\mathbf{T}, \mathbf{I}) &= 10 \log_{10} \left( \frac{\text{Max}(\mathbf{T})^2}{\text{MSE}(\mathbf{T}, \mathbf{I})} \right) \\
 &= 20 \log_{10}(\text{Max}(\mathbf{T})) - 10 \log_{10}(\text{MSE}(\mathbf{T}, \mathbf{I}))
 \end{aligned} \tag{5.1}$$

where  $\mathbf{T}$ ,  $\mathbf{I}$ ,  $\text{Max}(\mathbf{T})$  and  $\text{MSE}(\mathbf{T}, \mathbf{I})$  represent the template image, the reconstructed image, the maximum value in the pixels of the template image, and the Mean Squared Error (MSE) of the template and the reconstructed image, respectively. The MSE of images  $\mathbf{T}$  and  $\mathbf{I}$ , considering a size of  $m \times n$  for these images, is defined as:

$$\text{MSE}(\mathbf{T}, \mathbf{I}) = \frac{1}{mn} \sum_{(x,y)} \left( \mathbf{T}(x,y) - \mathbf{I}(x,y) \right)^2 \quad (5.2)$$

where the sum is performed over all the possible pixel coordinates  $(x, y)$ , which means that  $x$  runs between 1 and  $m$ , and  $y$  between 1 and  $n$ . The value of the MSE is then equivalent to the division between the SSD of these two images, defined by Eq. (3.25), and their respective number of pixels.

The PSNR compares the maximum possible value of a signal, which is usually referred as signal's power, with the intensity of the distorting noise that affects the quality of its representation. In the context of multi-frame super-resolution, the template image represents this signal while the reconstructed image, obtained with the algorithms, corresponds to the representation of such signal and that is affected by many distorting effects where the noise is the main one. From the definition introduced for the PSNR in Eq. (5.1), it is important to notice that small PSNR values are consequence of large MSE values which indicate the presence of high levels of noise in the reconstructed image. In an inverse manner, large PSNR values are consequence of small MSE values which indicate the presence of small noise levels in the reconstructed image.

### 5.3.2 Reduced $\chi^2$

The reconstructed image, obtained after using a regularized multi-frame super-resolution algorithm over a set of low-resolution images, is basically a fit respect to the information contained in that set of low-resolution images. The effectiveness of the model can be represented as the reconstructed high resolution image. Thus, this effectiveness can be measured against the available observations (represented by the set of low-resolution images). For this, the reduced  $\chi^2$  can be used.

The expression defining this performance metric is given by the following formula:

$$\text{Reduced } \chi^2 = \frac{1}{\nu} \sum_{k=1}^N \sum_{(x,y)} \frac{\left( \mathbf{M}_k(x,y) - \mathbf{O}_k(x,y) \right)^2}{\sigma_k^2} \quad (5.3)$$

where  $\mathbf{O}_k$  is the  $k$ -th image in the set of  $N$  low-resolution images (observations),  $\mathbf{M}_k$  is the degraded version of the reconstructed high-resolution image (model) degraded according to the parameters estimated for  $\mathbf{O}_k$ , and  $\sigma_k$  corresponds to the variance in  $\mathbf{O}_k$  which is, in this case, the variance of the noise contained in the low-resolution image represented by  $\mathbf{O}_k$ .

The inner sum is performed over all the possible pixel coordinates  $(x, y)$  in the space of low-resolution pixels, while the outer sum is performed over the set of  $N$  low-resolution images, in order to compare the pixel values between each low-resolution image and its corresponding degraded version of the reconstructed high-resolution image. Finally,  $\nu$  represents the number of degrees of freedom involved in the problem, given by:

$$\begin{aligned} \nu &= \binom{\text{Number of observations}}{\phantom{\text{Number of observations}}} - \binom{\text{Number of fitted parameters}}{\phantom{\text{Number of fitted parameters}}} - 1 \\ &= \binom{\text{Total number of low-resolution pixels}}{\phantom{\text{Total number of low-resolution pixels}}} - \binom{\text{Total number of high-resolution pixels}}{\phantom{\text{Total number of high-resolution pixels}}} - 1 \end{aligned} \quad (5.4)$$

Therefore, a high-resolution image of size  $2L \times 2L$  is to be reconstructed using a set of  $N$  low-resolution images of size  $L \times L$ , then the value of  $\nu$  will be:

$$\begin{aligned} \nu &= (N \cdot L \cdot L) - (2L \cdot 2L) - 1 \\ &= L^2(N - 4) - 1 \end{aligned} \quad (5.5)$$

which means that, for  $N = 10$  and  $L = 100$  (corresponding to the case where a set of 10 low-resolution images, each one with a size of  $100 \times 100$  pixels, is used to recover a high-resolution with a size of  $200 \times 200$  pixels), the value of  $\nu$  corresponds to 59,999.

In general terms, a value close to 1 for the reduced  $\chi^2$  indicates that the degree of match between the observations (low-resolution images) and the model (reconstructed high-resolution images) is in accordance with the variance (noise). A value bigger than 1 indicates that the model has not fully represented the data (or that the error variance has been underestimated), while a value smaller than 1 indicates that the model is over-fitting the data (or that the error variance has been overestimated).

## 5.4 Experimental frameworks

Two experimental frameworks were considered for the organization of the different experiments of this thesis. In the first experimental framework (1EF), the performance of the four multi-frame super-resolution algorithms was analyzed considering a wide range of SNR values, and using only low-resolution images obtained with the IOM. In the second experimental framework (2EF), the algorithms' performance was analyzed in a range of SNR values similar to the one employed in the 1EF, but using low-resolution images obtained with both simulation schemes (PhoSim and IOM). Ideally, all the algorithms would have been tested with both simulations schemes and considering exactly the same range of SNR values, but this was not possible due to the nature of the mechanisms employed by PhoSim for simulating images. Since PhoSim bases its operation in a Monte Carlo approach, it is not feasible to obtain simulated images with an exact and predetermined value for the SNR. Nevertheless, the final range of SNR values obtained after simulating images with PhoSim is very similar

to the one used in the 1EF, since the parameter values employed for these simulations were selected with this purpose.

The idea behind these two different experimental frameworks is to test the four multi-frame super-resolution algorithms under different circumstances. In the 1EF an ideal case is considered, since the reconstructions are performed employing the parameters used in the simulation process carried out with the IOM. Moreover, a real case is considered in the 2EF, since before performing the multi-frame super-resolution reconstruction, a stage where the different parameters required are estimated is carried out. Therefore, in this 2EF all the parameters needed for the operation of the four multi-frame super-resolution algorithms, and which correspond to the blur and registration parameters, are estimated as should be done in practice.

### 5.4.1 First experimental framework (1EF)

The aim of the 1EF is to validate the proper operation of the four multi-frame super-resolution algorithms, LA, LZ, GA and GZ, in a wide range of SNR values. In order to do that, the sets of low-resolution images were generated using the first simulation scheme, which is based on the IOM, to then perform multi-frame super-resolution reconstruction employing the parameters that were used during the simulation process.

Only simulations based on the IOM were considered, because we did not have explicit control over all the relevant parameters with PhoSim. Since it is not possible to simulate low-resolution images with PhoSim according to a specific set of values for all these relevant parameters related to the super-resolution procedure, the reconstruction of high-resolution images considering an ideal case is not feasible due to the necessity of estimating all these parameters, which supposes the introduction of a degree of error in the reconstruction process.

This experimental framework has three main stages. The first one consists in the simulation of the different sets of low-resolution images, using as input the template set of high-resolution images and the selected simulation parameters. The second stage is given by the reconstruction of high-resolution images with all the algorithms, employing the sets of simulated low-resolution images and the already known simulation parameters. The third and final stage consists in the computation of the two metrics used to characterize the performance of the algorithms. The PSNR is computed for each one of the algorithms using the template image, employed to generate the input set of low-resolution images, and the image reconstructed from that set. Finally, the reduced  $\chi^2$  is also computed for each one of the algorithms, employing the set of low-resolution images, their SNR values (obtained from the simulation parameters) and the high-resolution image that was reconstructed from that set. A flow chart describing this experimental framework, its three stages and the relations between them is presented in Figure 5.2.

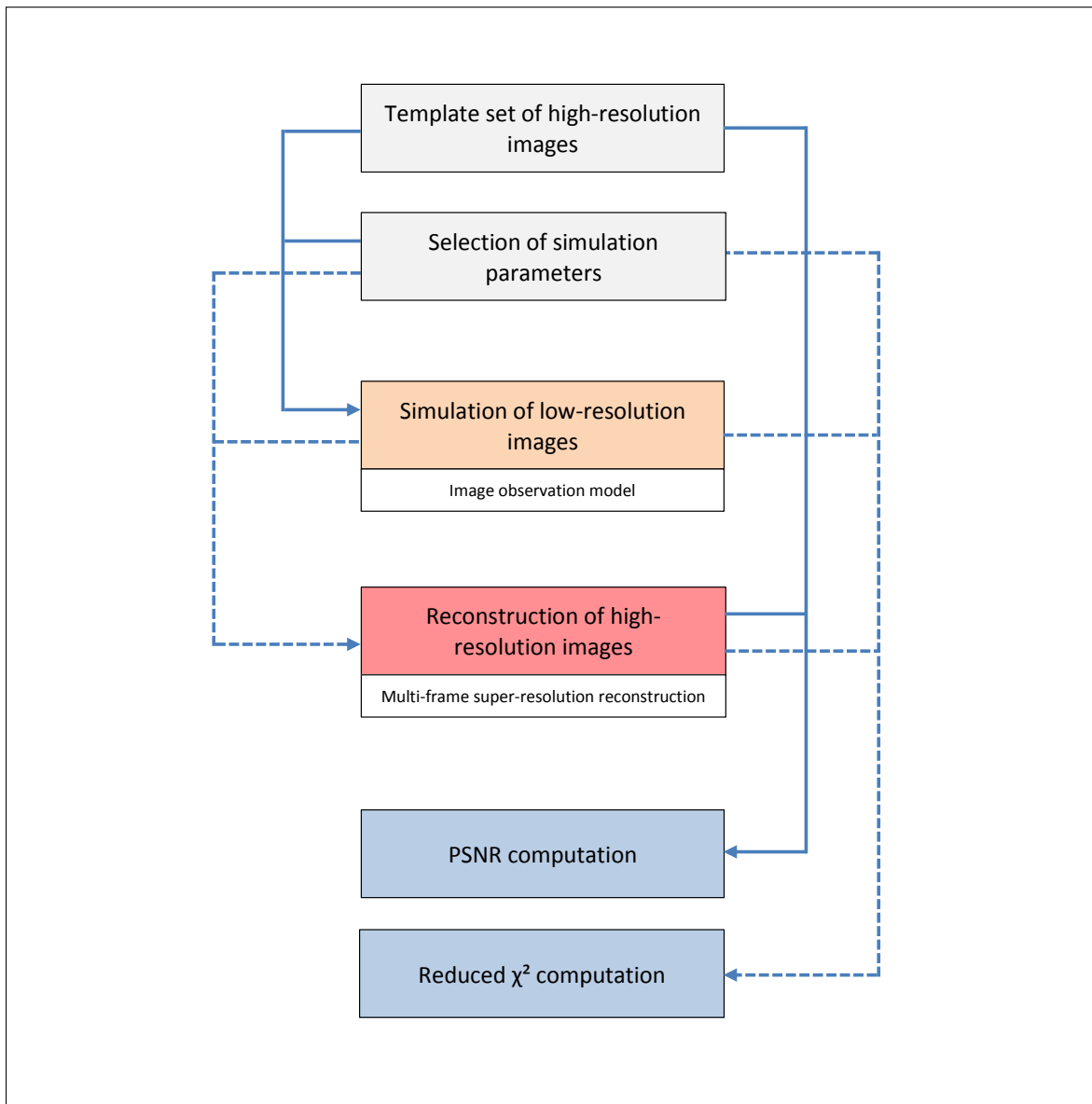


Figure 5.2: This flow chart presents the three successive stages of the 1EF: simulation of low-resolution images (orange), multi-frame super-resolution (red) and computation of metrics (blue).

### First stage: simulation of low-resolution images

For the simulation process performed in the first stage of this experimental framework, an equispaced and wide set of seven SNR values, between 1 and 100, considering a logarithmic scale, was used. The considered set of SNR values was  $\{1, 2.15, 4.64, 10, 21.54, 46.42, 100\}$ , which was obtained from the computation of the values of the expression  $10^{\frac{i}{3}}$  for  $i$  in  $\{0, 1, 2, 3, 4, 5, 6\}$ . A fixed value of 2 was considered for the downsampling factor, which means that the area of a low-resolution pixel is four times the area of a high-resolution pixel. For the FWHM of the Gaussian approximation of the PSF, a value of 3.52 pixels was employed.

Table 5.1: Parameters employed in the simulation stage of the first experimental framework.

Parameter	Value specification
Set of SNR values	{1.0, 2.15, 4.64, 10.0, 21.54, 46.42, 100.0}
Number of sets of LR images for each SNR value	100
Number of LR images in each set	10
Downsampling Factor	2
FWHM of the considered PSF (pixels)	3.52
Coordinates of translations with sub-pixel accuracy	Randomly selected in {0, 0.05, 0.1, ..., 0.95}

Using the parameter values previously specified, 100 sets of 10 low-resolution images each were generated for each SNR value in the considered range, where each one of these images was obtained with the simulation scheme based on the IOM. In the simulation process, translations with sub-pixel accuracy were considered in order to allow the utilization of the multi-frame super-resolution algorithms. Each one of the two values that define these translations (one by each coordinate) were randomly selected from the set  $\{0, 0.05, 0.1, \dots, 0.95\}$ .

Since a range of 7 values was considered for the SNR, 7 different sets of low-resolution images, each one containing 10 frames, were generated from each high-resolution image template. This means that a total amount of 7000 low-resolution images were simulated in this first stage of the 1EF. A summary with all the parameters employed in these simulations is presented in Table 5.1.

### Second stage: reconstruction of high-resolution images

Using the simulation parameters previously introduced, four high-resolution images were reconstructed, employing each one of the four multi-frame super-resolution algorithms, from each one of the 700 available sets of simulated low-resolution images. This means that a total of 2800 reconstructions were performed during this stage of the first experimental framework.

### Third stage: computation of performance metrics

In order to measure the performance of the four multi-frame super-resolution algorithms, the two metrics previously presented were computed. The PSNR was computed using the image reconstructed by each one of the algorithms from an input set, and the high-resolution image template that was employed to simulate that set. The reduced  $\chi^2$  was computed using the image reconstructed by each one of the algorithms and the set of low-resolution images employed to reconstruct that image. Also, the value of the SNR considered for the simulation of this input set was used to obtain the standard deviation of the noise contained in each one of the simulated low-resolution images, a parameter required in the computation of the reduced  $\chi^2$ .

Therefore, for each one of the four multi-frame super-resolution algorithms and each one of the seven SNR values contemplated in this framework, there are 100 computed values for the PSNR and the reduced  $\chi^2$ . Then, employing this information, the average and the

standard deviation of both metrics were calculated, in order to construct two performance curves by algorithm (one for each metric). These curves are presented in Section 6.1.

### 5.4.2 Second experimental framework (2EF)

The purpose of the 2EF is to study the performance of the four multi-frame super-resolution algorithms under more realistic circumstances. In order to do this, the estimation of the two parameters needed for employing the four multi-frame super-resolution algorithms, which are the PSF and the registration, is incorporated as another requirement of the experiments considered in this second framework. For all these experiments, whose details are presented later, the PSF is estimated using the procedure previously introduced (see Section 4.3.1), while the registration parameters are estimated employing affine and quadratic registration.

This experimental framework is made up of four stages. In the first one, two different groups of sets of low-resolution images were generated, each one obtained with one of the two simulation schemes available, PhoSim and the IOM. In the second stage, the FWHM of the Gaussian approximation of the PSF and the registration parameters are estimated using the procedures mentioned above. In the third stage, multi-frame super-resolution is performed by each algorithm in the two groups of input sets (each one obtained with one simulation scheme) and considering the parameters estimated in the previous step. Since there are two estimations for the registration parameters (affine and quadratic), and also two groups of low-resolution image sets (obtained with PhoSim and the IOM), four PSNR and reduced  $\chi^2$  values are then computed, in the final stage, for each algorithm and each value in the SNR range considered. A flow chart describing this second experimental framework, its three stages and the relations between them is presented in Figure 5.3.

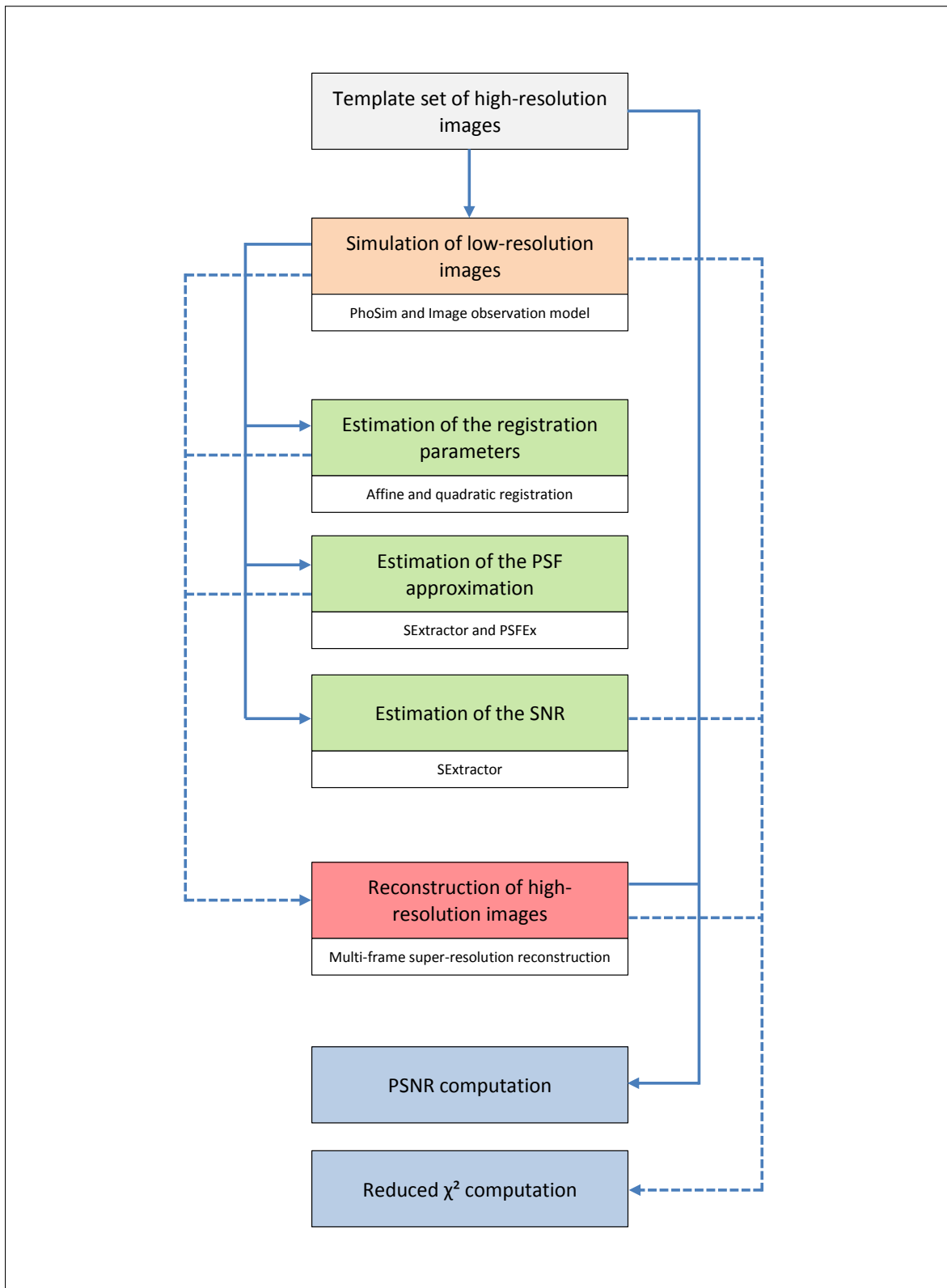


Figure 5.3: This flow chart presents the four successive stages of the 2EF: simulation of low-resolution images (orange), estimation of the parameters (green), multi-frame super-resolution reconstruction (red) and computation of metrics (blue).

Table 5.2: The values employed for the exposure time in the PhoSim simulations of the 2EF are displayed in the first column. In second column we can see the average SNR computed for the images obtained from these simulations with their corresponding errors (standard deviation). In the third column the percentages that represent these errors respect to the average SNR values are displayed.

Exposure time (s)	Estimated SNR	SNR percentage error
3.5	$1.43 \pm 1.02$	71.32 %
5.0	$2.68 \pm 1.42$	52.99 %
6.5	$5.37 \pm 2.21$	41.16 %
9.0	$10.32 \pm 3.88$	37.60 %
30.0	$25.87 \pm 6.31$	24.39 %
90.0	$52.12 \pm 9.85$	18.90 %
240.0	$96.56 \pm 13.98$	14.48 %

### First stage: simulation of low-resolution images

In the first stage of the 2EF, two groups of sets of low-resolution images were simulated, using the high-resolution image templates and both simulation schemes. First, images were simulated employing PhoSim considering a set of 7 *exposure times* for a fixed *magnitude*<sup>1</sup> value. With these two parameters we were able of having certain degree of control over the SNR of the simulated images generated by PhoSim, since the exposure time corresponds to the amount of time employed in the observation of a source during the acquisition of an astronomical image, while the magnitude is a measure of the brightness of that source or, in other words, the amount of that photons are emitted by unit of time from such source.

The image simulation was then performed considering the values corresponding to 3.5, 5.0, 6.5, 9.0, 30.0, 90.0 and 240.0 seconds for the exposure time and fixed magnitude of 16. These values were selected in order to obtain a SNR range as similar as possible to the one considered in the 1EF. Unfortunately, due to the Monte Carlo approach of PhoSim, the use of an specific exposure time value in two different simulations of the same image does not imply the obtention of the same SNR value. Because of this, the 100 sets of low-resolution images, generated for each one of the 7 exposure times considered, were characterized in terms of the average of the SNR values computed for each one of these sets. The details with the relation between these 7 values employed for the exposure time and the average SNR values estimated for the simulated low-resolution images are presented in Table 5.2.

Later, using the sequence of SNR values obtained for each one of these 7 exposure times (and that correspond to 1.43, 2.68, 5.37, 10.32, 25.87, 52.12 and 96.56), the second group of low-resolution images were generated, employing the first simulation scheme that corresponds to the IOM. The idea behind this is to enable the later comparison between the reconstruction results obtained with both groups of simulated low-resolution images, by considering the same range of SNR values. Also, in order to allow this comparison, the same downsampling factor (corresponding to 2) was considered for both groups of low-resolution images, and the

---

<sup>1</sup>In astronomy, the magnitude is the logarithmic measure of the flux of photons emitted by a source, considering a specific wavelength or band.

FWHM of the Gaussian approximation obtained for the LSST (corresponding to 3.52 pixels) was employed in the simulations performed with the second scheme.

For both groups of simulated low-resolution images, the inclusion of random translations was considered, where the values of the two coordinates of these translations were randomly selected from the set  $\{0, 0.05, 0.1, \dots, 0.95\}$ . In practice, the inclusion of these translations in the low-resolution images generated with PhoSim was not really relevant, since the final position of an image is very variable due to the atmospheric turbulences included in the default setting of this simulation tool. This means that the registration parameters are always unknown for the simulations obtained using PhoSim, as a consequence, the utilization of a registration procedure is required. To understand how atmospheric turbulences affect the simulated images, introducing spontaneous motions and modifying the shape of the astronomical objects contained in these images, Figure 5.4 presents three simulations of a star (point source) where these effects can be observed. These three simulations were obtained with PhoSim and employing, in each one, the same set of parameter values (without considering any motion). Also, since a point source is considered as an input for the simulations presented in Figure 5.4, these three images allow to have a notion of the FWHM of the Gaussian approximation of PSF of the LSST.

The parameter values employed for both groups of simulations are presentend in Table 5.3 and Table 5.4. In the first one, the parameter values considered for the simulations generated with Phosim are shown, while the second table shows the values employed in the simulations performed with the scheme based in the IOM.

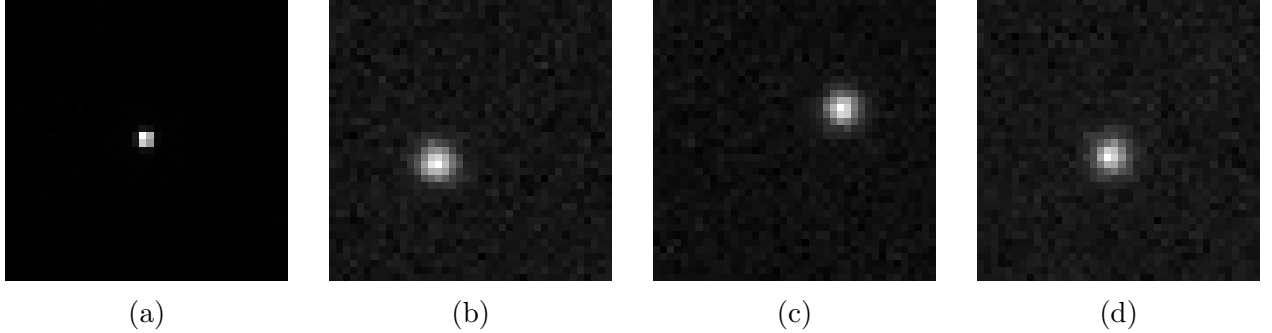


Figure 5.4: The simulated result of observing a point source without the presence of the atmosphere is presented in (a). Images (b), (c) and (d) are simulations obtained with the same set of parameter values for the observation of that point source but considering the presence of the atmosphere. All these simulations were generated with PhoSim.

## Second stage: Estimation of parameters

In the second stage of the 2EF, different procedures are employed to estimate the FWHM of the PSF and the registration parameters. The estimation of the FWHM is performed using SExtractor and PSFEx, in the same manner that has been previously mentioned. The estimation of registration parameters is carried out using the two approaches presented in this thesis, where the SSD between images is minimized considering affine or quadratic transformations to model the motion.

Table 5.3: Parameters employed in the simulations performed with PhoSim in the first stage of the 2EF.

Parameter	Value specification
Set of exposure time values (s)	{3.5, 5.0, 6.5, 9.0, 30.0, 90.0, 240.0}
Magnitude	16
Number of sets of LR images for each exp. time value	100
Number of LR images in each set	10
Downsampling Factor	2
Coordinates of translations with sub-pixel accuracy	Randomly selected in {0, 0.05, 0.1, ..., 0.95}

Table 5.4: Parameters employed in the simulations performed with the IOM in the first stage of the 2EF.

Parameter	Value specification
Set of SNR values	{2.04, 3.46, 5.18, 6.45, 8.29, 10.86, 12.30, 14.62}
Number of sets of LR images for each SNR value	100
Number of LR images in each set	10
Downsampling Factor	2
FWHM of the considered PSF (pixels)	3.52
Coordinates of translations with sub-pixel accuracy	Randomly selected in {0, 0.05, 0.1, ..., 0.95}

Therefore, since there are two different groups of simulated low-resolution images (each one generated with a different simulation scheme) and two approaches for computing the registration parameters (affine and quadratic), there is a total number of four different scenarios where the performance of the four multi-frame super-resolution algorithms can be tested. This also means that each registration procedure is employed 1,400 times, because each one of the two groups of simulated low-resolution images is made up of 700 sets (since 7 SNR values and 100 high-resolution image templates are considered).

### Third stage: Reconstruction of high-resolution images

The reconstruction of high-resolution images, using each one of the algorithms in the four considered scenarios, is the purpose of the third stage of this experimental framework. In this case there are, for each SNR value (from a total number of seven), two groups of 100 sets of low-resolution images (with each set composed by 10 frames), where each set has two associated registration estimates. These four scenarios mentioned, each one defined by the simulation scheme and the registration approach employed, are given by:

- Case 1: PhoSim and affine registration
- Case 2: IOM and affine registration
- Case 3: PhoSim and quadratic registration
- Case 4: IOM and quadratic registration

According to this, each one of the four algorithms performs 700 reconstructions in each scenario (100 sets of simulated low-resolution images for each one of the seven SNR values).

Since four different algorithms (LA, LZ, GA and GZ) and four different scenarios are considered, in this third stage of this experimental framework 11,200 reconstructions are performed in total (2,800 by each algorithm).

#### **Fourth stage: computation of performance metrics**

In fourth and final stage of this experimental framework, the performance metrics are calculated for each algorithm in each one of the four scenarios considered. The PSNR is computed as usual, using the reconstructed image and the high-resolution image template. In the case of the scenarios where the simulated low-resolution images were obtained employing PhoSim, the computation of the PSNR will be affected by the registration errors. This means that, for these cases, the PSNR is a biased metric of the performance. This problem does not affect the results of the reconstructions performed with low-resolution sets obtained using the IOM, because in these cases the registration parameters used for a proper computation of the PSNR are known beforehand.

The reduced  $\chi^2$  is also computed as usual, employing the reconstructed image, the set of low-resolution images used as input in the reconstruction process of that image, and the SNR value associated to this set (used to obtain the standard deviation of the noise, which is known from the first stage). Also, for the scenarios where simulated low-resolution images, generated with PhoSim, are used as input of the reconstruction process, the errors introduced during the registration and the SNR estimation process affect the suitable computation of the reduced  $\chi^2$ . Then, for these cases, this metric is also a biased estimator of the performance of the algorithms. This is not a problem for the cases where simulated low-resolution images were generated using the IOM, since all the parameters required for an exact computation of the reduced  $\chi^2$  are known beforehand.

## **5.5 Relevant technical aspects**

A review about some relevant technical aspects, concerning to the implementation and execution of the different multi-frame super-resolution algorithms and registration procedures mentioned along this thesis, is now presented. The idea behind the discussion of these aspects is to provide all the details needed to have a comprehensive understanding of the experiments considered in this thesis.

### **5.5.1 Implementation of multi-frame super-resolution algorithms**

The multi-frame super-resolution problem was posed as an optimization problem, where a cost function should be minimized. Each one of the four super-resolution algorithms is consequently defined in terms of a specific cost function and its gradient. The expressions for these cost functions and their gradients, considering the mathematical derivation of each expression, were presented in Chapter 3.

The implementation of the algorithms was then carried out considering a gradient-based approach where these expressions are employed. As was previously mentioned, the most straightforward implementation is given by the employment of the gradient descent method. However, this option was discarded, since this method, due to its simplicity, usually shows a relatively slow convergence and difficulties when finding the global minimum if the problem is not convex enough.

The method finally selected for the implementation of the multi-frame super-resolution algorithms was the non-linear conjugate gradient. This selection can be considered as a design decision, since there is no specific recipe for the selection of optimization procedures, although theory suggests that this method has a better performance than, for example, gradient descent or Gauss-Newton methods. Besides, this method only requires the gradient's expression to operate, which is an advantage since many optimization procedures also need an expression for the Hessian matrix. The algorithms' implementation relied in the utilization of the non-linear conjugate gradient implementation provided by *Scipy*<sup>2</sup>, a Python package for scientific computing, in its module *optimize*.

Another aspect that should be mentioned about the implementation of the four multi-frame super-resolution algorithms is that a limit value was defined for the maximum number of iterations during the minimization process. The reason for establishing this limit is to avoid unnecessary oscillations around a minimum when the available precision is not enough for reaching such minimum in an exact manner. In practice this limit did not have any relevant impact over the results obtained in the different experiments, since in most cases the algorithms required less than 50 iterations to converge to a minimum of their corresponding cost functions.

## 5.5.2 Implementation of image registration

The image registration problem was also posed as an optimization problem where a cost function should be minimized. Two different strategies for image registration were considered: the first one, known as affine registration, employs affine transformations for motion modeling, while the second one, known as quadratic registration, uses quadratic transformations for the same. For these two strategies there are also expressions for the corresponding cost function and its gradient, which were presented in Chapter 3. Therefore, both image registration procedures were implemented also employing the non-linear conjugate gradient, in exactly the same manner considered in the section above.

It is important to notice that the general expressions for the cost function and its gradient, which are given by Eq. (3.25) and Eq. (3.27), are the same for both registration procedures. The differences appear when the motion models considered by each procedure are replaced into this pair of expressions, yielding to different formulas for the cost function and its gradient in each case. The motion model based on affine transformations, which has 6 degrees of freedom, is specified by Eq. (3.29), while the motion model based on quadratic transformation, which has 12 degrees of freedom, is specified by Eq. (3.31).

---

<sup>2</sup><http://scipy.org/>

Another relevant aspect about image registration is the employment of interpolation techniques. The obtention of an image after applying a transformation requires the utilization of an interpolation procedure, since the coordinates of the new pixels generated by a transformation are usually not-integer, meaning that the information in-between pixels should be estimated in order to generate the transformed image. For this task we employed the implementation of the interpolation technique known as *cubic splines* provided by *Scipy*.

### 5.5.3 Implementation of the prior terms

Two prior terms, Laplacian and gradient, are considered for the different cost functions associated with each one of the multi-frame super-resolution algorithms. The Laplacian prior, specified in Eq. (3.14), and which was employed in the implementation of the algorithms, corresponds to the following kernel:

$$\Gamma_l = \begin{bmatrix} 1 & 1 & 1 & 1 & 1 \\ 1 & 1 & 1 & 1 & 1 \\ 1 & 1 & -24 & 1 & 1 \\ 1 & 1 & 1 & 1 & 1 \\ 1 & 1 & 1 & 1 & 1 \end{bmatrix} \quad (5.6)$$

On the other hand, the gradient prior, specified in Eq. (3.15), was computed using central differences for each one of the pixels along each direction. Later, using the results obtained for both directions, the magnitude of the gradient is computed for the image considered to then obtain the kernel required for the cost function (and its gradient) by matrix inversion.

### 5.5.4 Utilization of the NLHPC's cluster

All the experiments described for this thesis were performed employing the supercomputing infrastructure provided by the *Leftraru* cluster of the National Laboratory for High Performance Computing<sup>3</sup> (NLHPC). The utilization of this cluster was a key element for carrying out these experiments, since many of the processes involved have significant requirements of memory and computing capacity. The obtention of the results presented in this thesis would have not been possible if the only available resources had been those of a personal computer.

For example, the purpose of the experiments described here is to study the performance of the four multi-frame super-resolution algorithms when they are employed to recover a high-resolution image, with a size of  $200 \times 200$  pixels, from a set of 10 low-resolution images, each one with a size of  $100 \times 100$  pixels. In order to do this, each algorithm needs to compute 10 degradation matrices (denoted by  $W_i$  in the equations previously reviewed), where each one of these matrices has a size of  $10,000 \times 40,000$ . Considering that each one of the values contained in these matrices is stored in memory using 8 bytes, then the memory space employed by each one of these 10 matrices is 3.2 GB. The minimization process needs

---

<sup>3</sup><http://www.nlhpc.cl>

to have simultaneous access to these 10 matrices for computing the value of the cost function and its gradient, thus the utilization of the algorithms in the different experiments requires of at least 32 GB in order to store the 10 degradation matrices into RAM memory.

The NLHPC's cluster is made up of 128 nodes that can be employed by the users for running their programs according to a system of prioritization whose aim is to guarantee a balanced use of resources. Each one of these 128 nodes is made up of 20 cores (each one with an speed of 2.2 GHz) and it has a maximum availability of 48 GB of RAM memory. Therefore, by using the NLHPC's nodes considering a parallel scheme, it was possible to fulfill all the requirements (especially those corresponding to memory consumption), run the experiments, and then obtain all the results.

# Chapter 6

## Experimental results

In this chapter, the results obtained after conducting all the experiments previously detailed are presented. In these experiments, the performance of the four multi-frame super-resolution algorithms was characterized by measuring two metrics, the PSNR and the reduced  $\chi^2$ , as functions of a range of SNR values. First we present the results obtained for the First Experimental Framework (1EF), which represents an ideal setting in the context of the analysis performed in this thesis. Then we present the results obtained for the four cases that made up the Second Experimental Framework (2EF), which represents a real setting to study the algorithms' performance, since all the relevant parameters for the reconstruction process, and that correspond to the registration information and the PSF, are estimated with some degree of error.

A comparison between the outcomes achieved by the four multi-frame super-resolution algorithms in both experimental frameworks is also presented, which was carried out by computing the PSNR and the (Reduced  $\chi^2 - 1$ ) ratios between the results obtained in the 1EF and each one of the four cases of the 2EF. The purpose of this comparison is to have a notion of how much worse the performance of the algorithms is under real circumstances, compared to that obtained considering the ideal setting.

Finally, another group of performance comparisons results is introduced, this time between the different cases considered in the 2EF. First, the results obtained for the cases with a different registration approach and a common simulation scheme are compared, and later the results for the cases with a common registration approach and a different simulation scheme are also compared. The idea behind these second group of comparisons is to understand the influence of the two registration procedures, affine and quadratic, and the two simulation schemes, PhoSim and the Image Observation Model (IOM), in the performance results achieved by the algorithms in the four cases of the 2EF.

## 6.1 Results of the first experimental framework

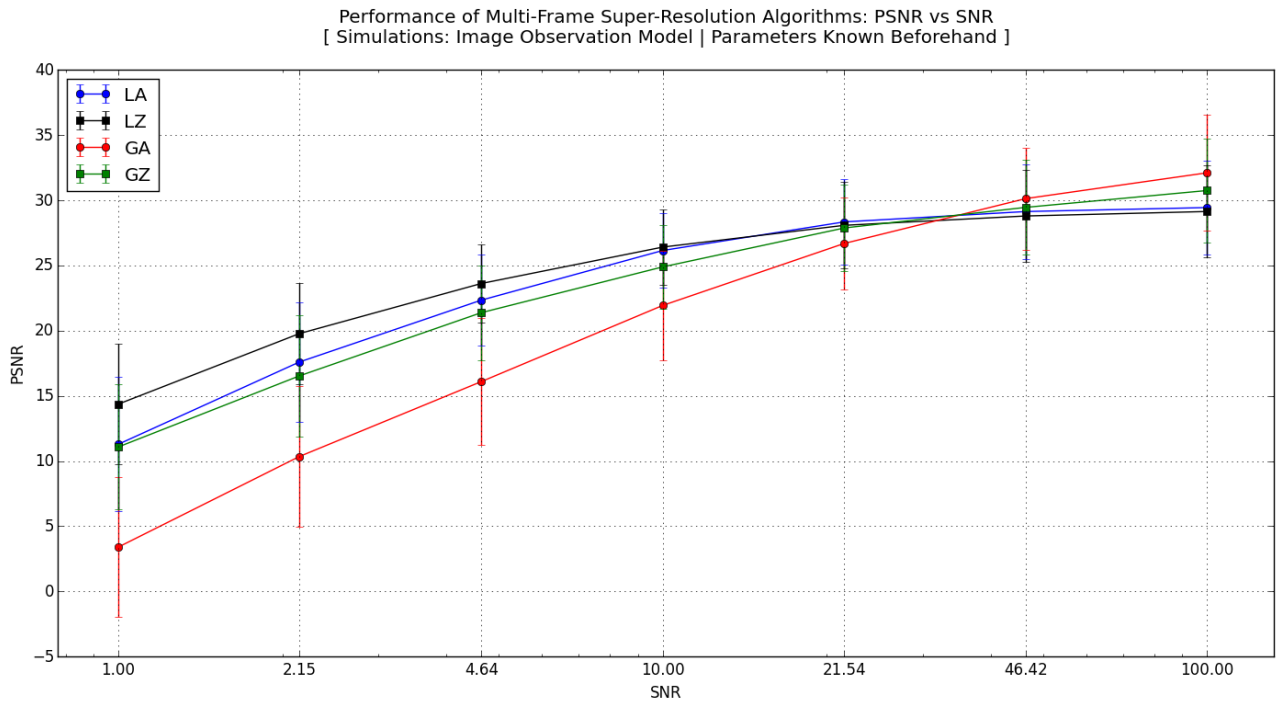
In the 1EF, the performance of the four multi-frame super-resolution algorithms under ideal circumstances was analyzed. In this case, all the parameters required for image reconstruction were known beforehand. The performance was measured employing the PSNR and the reduced  $\chi^2$  as metrics. The results obtained for both metrics are presented, as a function of the SNR value, in Figure 6.1a for the case of the PSNR, and in Figure 6.1b for the case of the reduced  $\chi^2$ . All the values presented in both plots are detailed in Table A.1.

For the case of the PSNR, the trend in the results shows an increase in the value of this metric as the SNR grows. This means that the algorithms are working as expected, since the quality of the reconstructed image should be proportional to the amount of noise present in the low-resolution images of the input set.

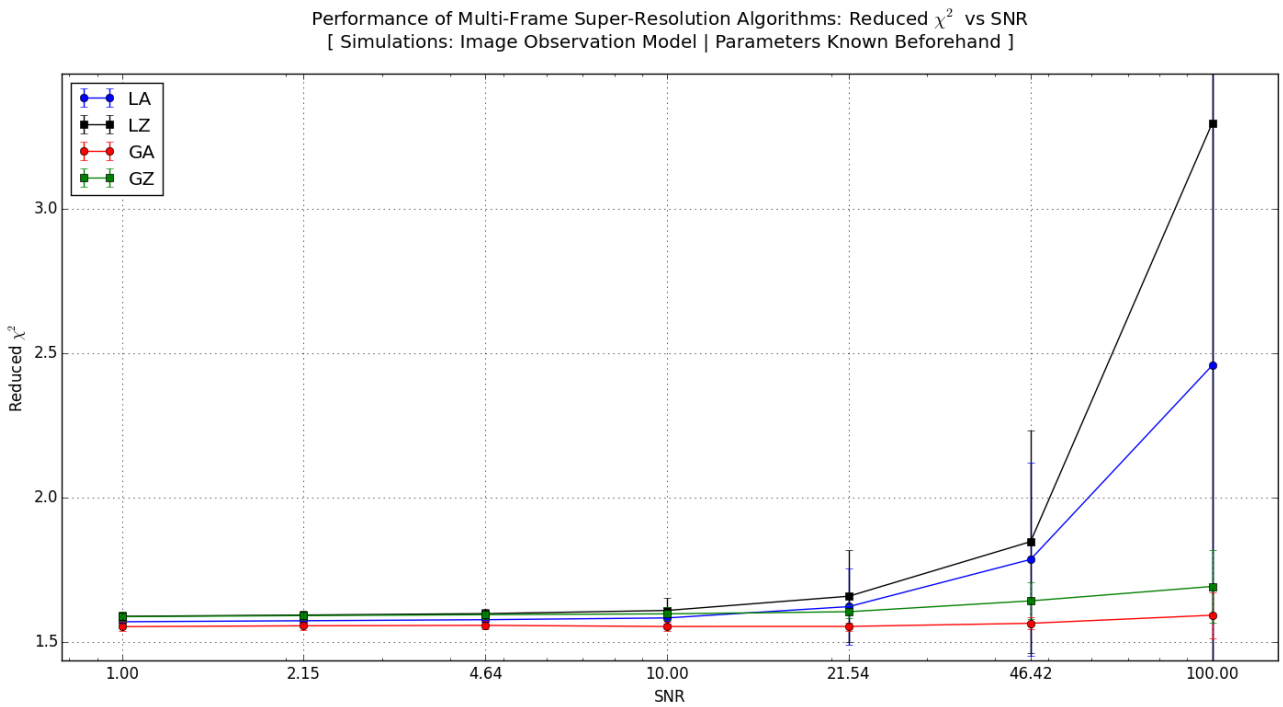
Regarding the specific behaviour of the algorithms it is important to note that, when the same prior is considered, the algorithm that uses Zomet's approximation for computing the gradient has a better performance for small SNR values (high levels of noise). However, for high SNR values, the approach based on the analytical computation of the gradient has a better performance. This difference is more evident between GA and GZ than between LA and LZ (LA only has a slightly better performance than LZ for high SNR values). These results also indicate the existence of a critical point for the SNR, located between 21.54 and 46.42, which divides the SNR range between small and large values. These results also prove that Zomet's approximation is indeed an appropriate tool to deal with the presence of noise, since the algorithms that employ Zomet's approximation for computing the gradient achieve better performances than their counterparts, which use the analytical expression, for SNR values smaller than said critical point.

For the case of prior selection, the PSNR results suggest that a Laplacian prior is the best choice for small SNR values, while the gradient prior presents better results if high SNR values are considered. The performance differences for small SNR values between LA and GA (both algorithms employ the analytical expression of the gradient) show a clear improvement in the outcome if the Laplacian prior is used instead of the gradient prior. Besides, in the four PSNR curves, the ratio between the size of the error bars (that represents the standard deviation) and the value of the metric decreases when the SNR grows. Therefore, all the algorithms work in a more stable manner if the presence of noise is diminished in the group of images of the input set.

The values obtained for the reduced  $\chi^2$  of GA and GZ are very stable, and have only a small tendency to increase as the SNR grows. Moreover, in the case of LA and LZ, this trend is only valid for SNR values equal or smaller than 10.0, since both algorithms present a significative increment of the reduced  $\chi^2$  for higher SNR values. This means that the smoothing process, introduced by the utilization of the Laplacian prior, is actually removing signal instead of noise (which is to be expected, due to the low levels of noise considered). Besides, this small increasing tendency in the reduced  $\chi^2$  values indicates that the quality of the reconstruction worsens when the SNR grows. This is a logical consequence derived from the design of the algorithms, since they all are a combination of different tools used to deal with noise. Because of this, performance is not the best when the input images have low



(a) PSNR vs SNR



(b) Reduced  $\chi^2$  vs SNR

Figure 6.1: Results obtained in the 1EF using the PSNR and the reduced  $\chi^2$  as performance metrics. In this case the blur and registration parameters are known beforehand.

levels of noise (in fact, the employment of the ML approach would be better for this case).

At first glance, values around 1.6 for the reduced  $\chi^2$  are not ideal, since the optimal value for this metric is 1 (which represents a perfect fit), and they suggest that the reconstructed image is not properly reflecting the information contained in the set of low-resolution images. However, this interpretation is not appropriate for the analysis of these specific results, since the reconstruction process carried out by the algorithms employed only 10 low-resolution images as input. This amount of images is not enough to perform a perfect reconstruction, this being the main reason for having values not close to 1, even for high SNR values. In fact, since all the reconstructions performed in the 1EF used the correct value for the different parameters required, the values obtained for the reduced  $\chi^2$  can be considered as a limit for algorithm performance when only 10 low-resolution images are available. Then, to the extent that more images are considered in the input set, these limit values should progressively get closer to 1.

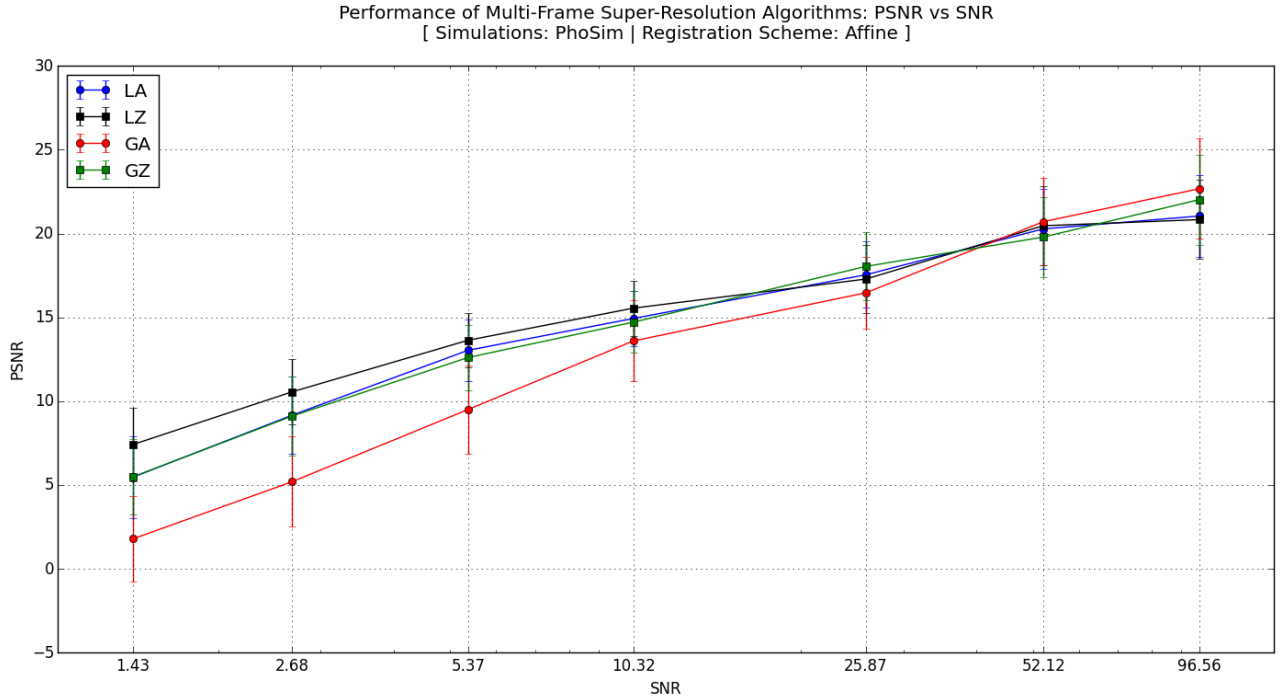
## 6.2 Results of the second experimental framework

The results obtained for the four cases considered in the 2EF are now presented. Each case is defined in terms of the approach used for the registration process (affine or quadratic) and the simulation scheme employed to obtain the different sets of simulated low-resolution images (PhoSim or the IOM). In the four cases the performance was measured using the PSNR and the reduced  $\chi^2$  as metrics.

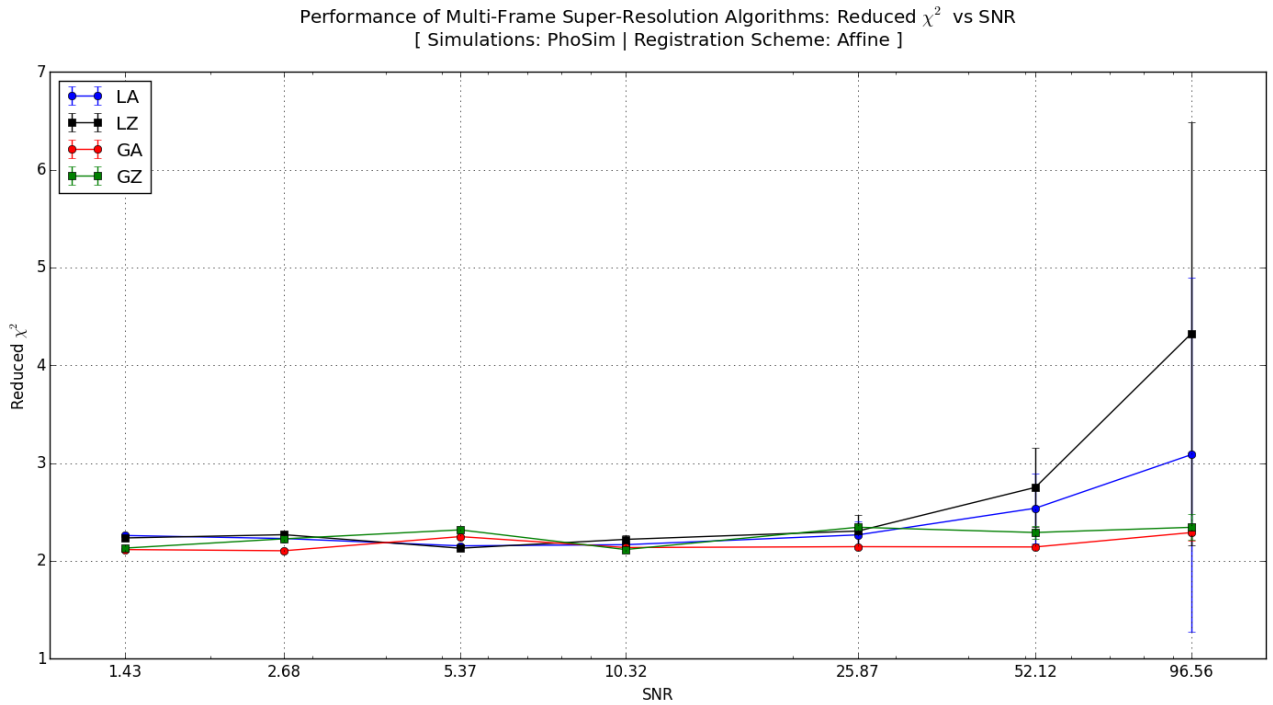
### 6.2.1 Case 1: PhoSim and affine registration

Performance results obtained for each one of the four multi-frame super-resolution algorithms in case 1 of the 2EF, where simulations were obtained using PhoSim and affine registration was employed for image alignment, are presented in Figure 6.2a for the case of the PSNR, and in Figure 6.2b for the case of the reduced  $\chi^2$ . All values presented in the curves of both plots are detailed in Table A.2.

For the case of PSNR, all curves show an increase in the value of this metric as the SNR grows. The ratio between the size of the error bars and the corresponding PSNR values also decreases as the SNR increases, which means that the stability of the algorithms improves if the noise levels in the input images are smaller. Also, a better performance of the methods that employ Zomet’s approximation for computing the gradient, instead of the analytical expression, can be noticed when high levels of noise are present. For SNR values smaller or equal than 10.32, LZ presents a better performance than LA, while LA achieves results slightly better than LZ for higher SNR values. In the case of the other two algorithms, we can notice that GZ has a better performance than GA for SNR values equal or smaller than 25.87, while this relation is reversed for higher SNR values. Regarding to the prior selection it can be noticed that, for small SNR values, the algorithms with Laplacian priors have better performances than their counterparts with gradient priors, while for higher SNR values the



(a) PSNR vs SNR



(b) Reduced  $\chi^2$  vs SNR

Figure 6.2: Results obtained in case 1 of the 2EF considering the PSNR and the reduced  $\chi^2$  as performance metrics. In this case the simulations are obtained using PhoSim and affine registration is employed for image alignment.

algorithms that employ gradient priors present better results, this being clearly evident for the highest SNR value of the considered range.

The results obtained for the reduced  $\chi^2$  should be divided into two groups for their analysis since, according to the prior selected, the curves present different behaviors. In the first place, we can notice that the reduced  $\chi^2$  values corresponding to GA and GZ oscillate between 2.104 and 2.344 with a slight tendency to decrease as the SNR grows. Moreover, the reduced  $\chi^2$  values obtained for LA and LZ oscillate between 2.129 and 2.305, a range very similar to the one previously mentioned, but only for SNR values equal or smaller than 25.87. For higher SNR values, the reduced  $\chi^2$  has a substantial growth for both algorithms, reaching values for the highest SNR corresponding to 3.086 in the case of LA and 4.324 in the case of LZ. It can be also noticed that the size of the error bars increases as the SNR grows in each one of the four curves.

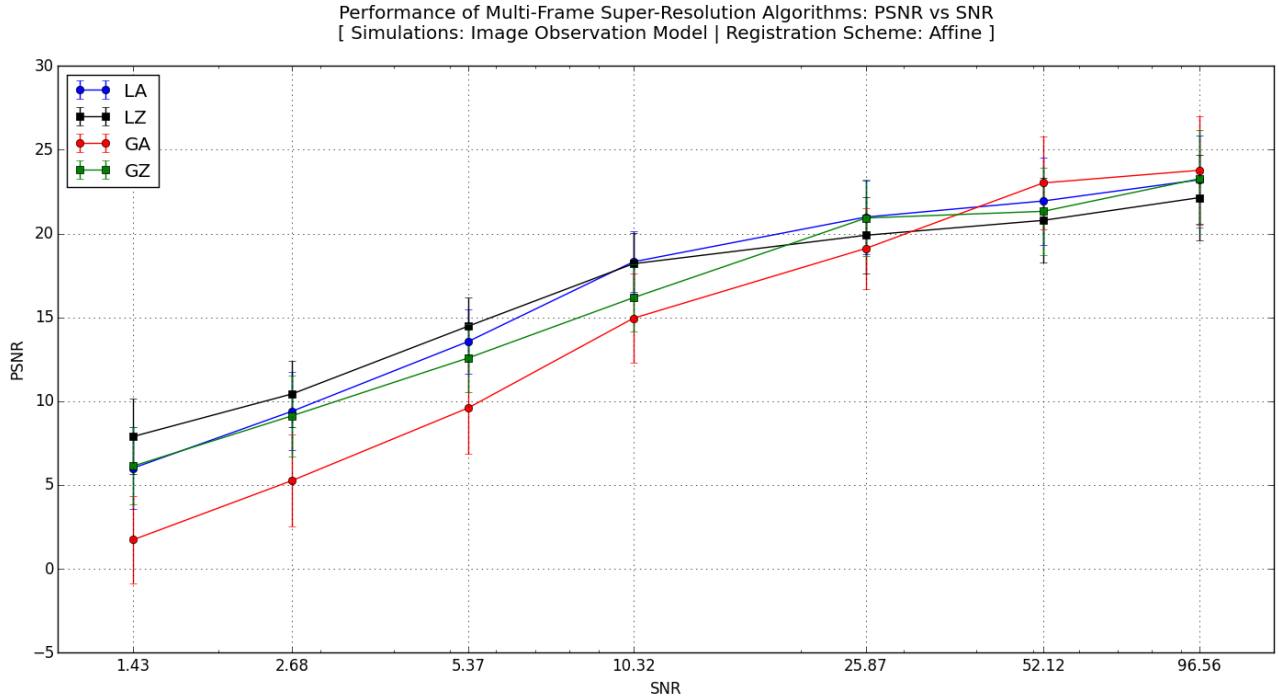
The behavior of the curves obtained for both performance metrics is consistent, in terms of the trends, with the results obtained in the 1EF. However, the results obtained in this first case of the 2EF framework are worse than the ones obtained in the 1EF, since the PSNR and reduced  $\chi^2$  values achieved by the algorithms are, respectively, smaller and larger than the ones achieved in the 1EF. This difference, which proves the existence of a reduction in the algorithms' performance in comparison with the results obtained in the 1EF, is a consequence of the errors associated to the process of estimating the blur and registration parameters. The details about this performance reduction will be later analyzed and discussed.

## 6.2.2 Case 2: Image observation model and affine registration

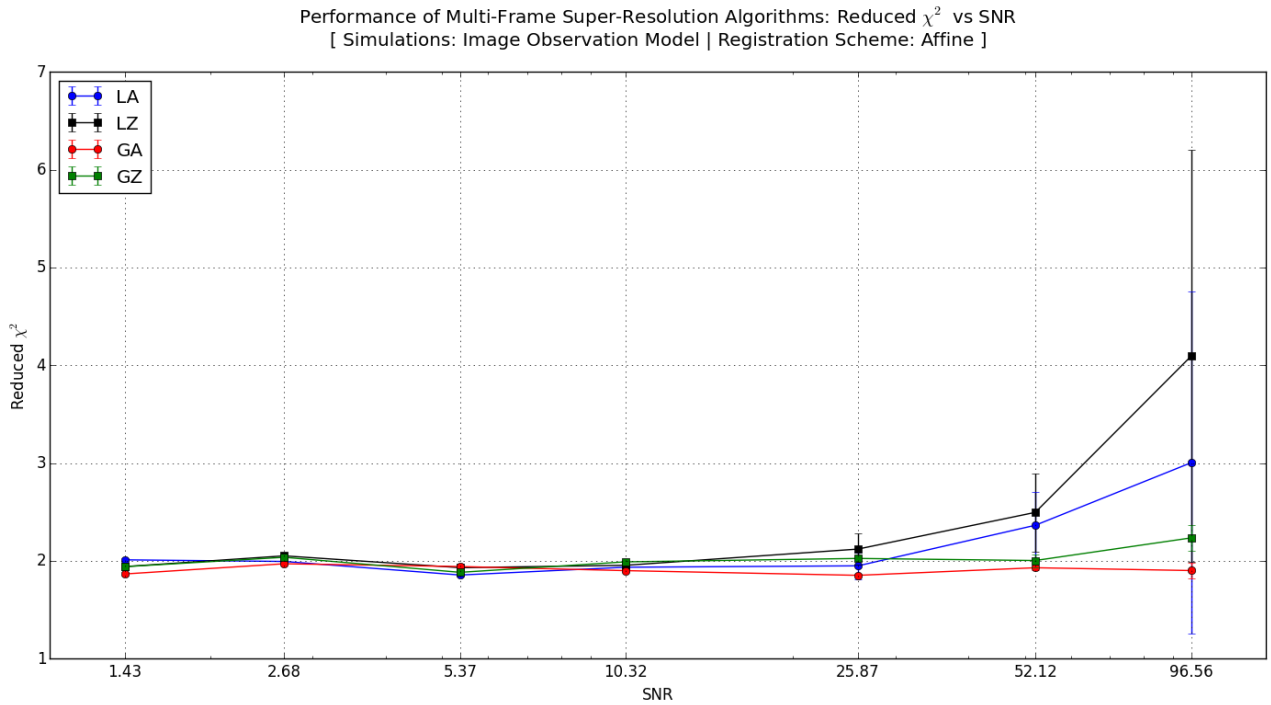
Performance results obtained for each one of the four multi-frame super-resolution algorithms in case 1 of the 2EF, where simulations were obtained using the IOM and affine registration was employed for image alignment, are presented in Figure 6.3a for the case of the PSNR, and in Figure 6.3b for the case of the reduced  $\chi^2$ . All values presented in the curves of both plots are detailed in Table A.3.

In the second case of the 2EF, all the PSNR curves show an increase in the value of this metric as the SNR grows, while the ratio between the size of the error bar and the corresponding PSNR value decreases as the SNR increases, since the error is relatively stable regardless of the SNR. Here it can be also noticed that the algorithms that use Zomet's approximation have better results, in a range of small SNR values, than their counterparts that employ the analytical expression of the gradient. In fact, LZ has a better performance than LA for SNR values equal or smaller than 5.37; then, both algorithms perform almost the same way for a SNR value of 10.32, while LA achieves better results than LZ for SNR values higher than 10.32. For SNR values equal or smaller than 25.87 we can see that GZ has a better performance than GA, but this relation is reversed for higher SNR values, where GA achieves better results than GZ.

In the curves obtained for the reduced  $\chi^2$  we can notice the same global trends that have been observed in the results corresponding to the 1EF and the first case of the 2EF. For the algorithms that use the gradient prior, GA and GZ, it can be noticed that their reduced  $\chi^2$



(a) PSNR vs SNR



(b) Reduced  $\chi^2$  vs SNR

Figure 6.3: Results obtained in case 2 of the 2EF considering the PSNR and the reduced  $\chi^2$  as performance metrics. In this case the simulations are obtained using the IOM and affine registration is employed for image alignment.

values oscillate between 1.852 and 2.235, without any clear tendency in the case of GZ and with a slight tendency to decrease in the case of GA. Moreover, the values corresponding to LA and LZ oscillate between 1.855 and 2.121 for SNR values equal or smaller than 25.87, while both algorithms present a significant growth for higher SNR values. In fact, for the highest value of the SNR range, corresponding to 96.56, the reduced  $\chi^2$  values achieved by LA and LZ are 3.004 and 4.095 respectively. Finally, in all these curves we can notice that the size of the error bars increases as the SNR grows.

The results obtained in this second case of the 2EF are consistent with those obtained in the 1EF, since we can observe the same general trends in the curves analyzed in both cases. Nevertheless, a reduction on the algorithms' performance can also be noticed here, since the results presented are worse than those obtained in the 1EF. A more detailed analysis about this performance reduction will be later presented.

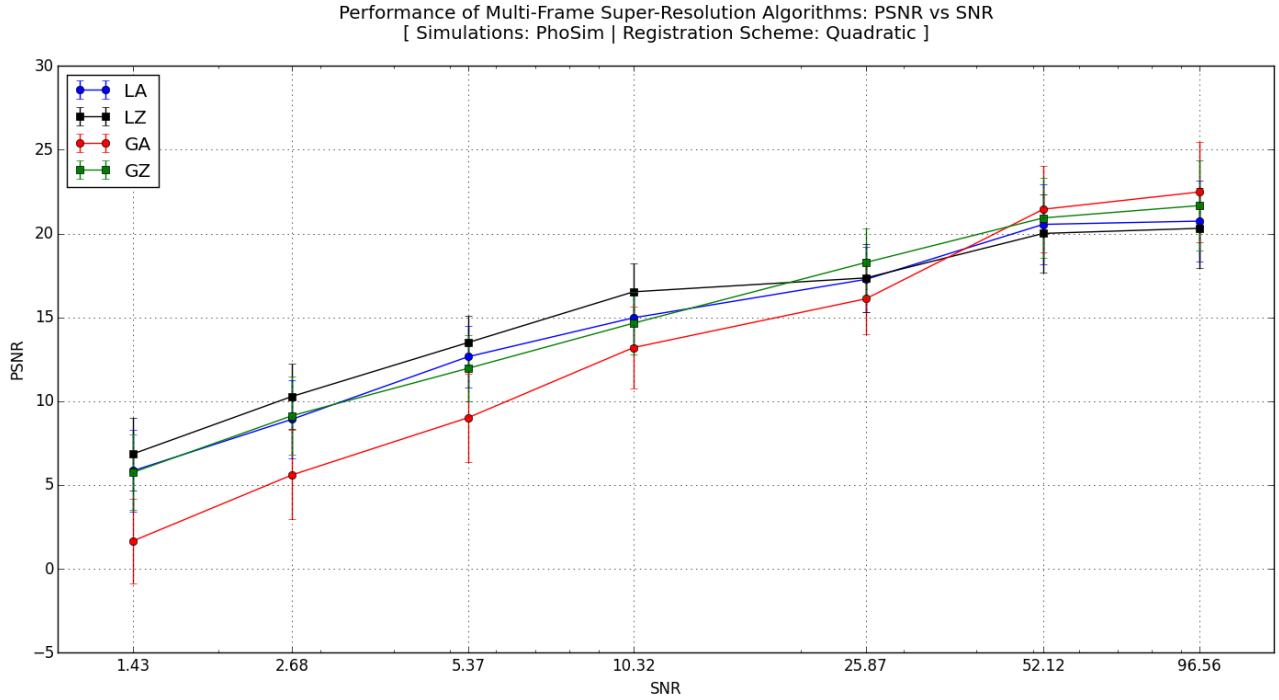
### 6.2.3 Case 3: Phosim and quadratic registration

Performance results obtained for each one of the four multi-frame super-resolution algorithms in case 3 of the 2EF, where simulations were obtained using PhoSim and quadratic registration was employed for image alignment, are presented in Figure 6.4a for the case of the PSNR, and in Figure 6.4b for the case of the reduced  $\chi^2$ . All values presented in the curves of both plots are detailed in Table A.4.

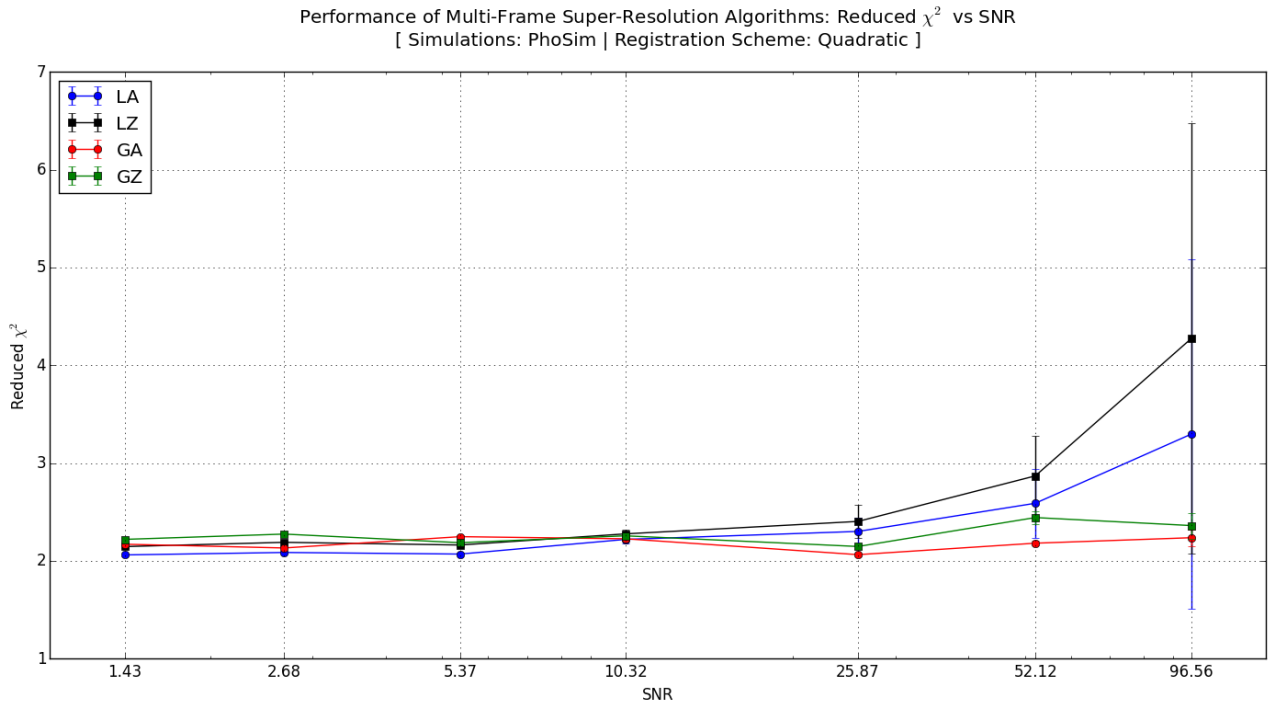
In the third case of the 2EF, the PSNR curves present the same tendencies observed in previous case: an increase in the PSNR value and a decrease in the ratio between the size of the error bars and the corresponding PSNR value as the SNR grows. Also, Zomet's approximation presents better results than the analytical expression for computing the gradient in a range of small SNR values. For SNR values equal or smaller than 25.87, GZ achieves better results than GA, while for higher SNR values this relation is reversed. In the case of LA and LZ we can notice that both algorithms have almost an identical performance for a SNR value corresponding to 25.87, while for smaller SNR values LZ achieves better results than LA and for higher SNR values LA performs better than LZ. Here it can be also noticed that the algorithms that use the Laplacian prior are the best choices for reconstructing images if the levels of noise are high, while the algorithms that employ the gradient prior offer better results when the levels of noise are low.

Regarding the results corresponding to reduced  $\chi^2$ , all the curves show the same general behavior that has been observed in previous cases. The values of the curves of GA and GZ oscillate between 2.064 and 2.443 without any specific tendency. For LA and LZ it can be noticed that the reduced  $\chi^2$  values oscillate between 2.061 and 2.403 for SNR values smaller or equal than 25.87. Also, as in previous cases, for the two highest SNR values the curves corresponding to LA and LZ present an important growth. For a SNR value of 96.56, which corresponds to the highest value of the SNR range, 3.296 and 4.274 are the reduced  $\chi^2$  values achieved respectively by LA and LZ. Moreover, the size of the error bars increases as the SNR grows for each one of the four curves analyzed.

The behavior of the PSNR and reduced  $\chi^2$  curves is consistent with the results previ-



(a) PSNR vs SNR



(b) Reduced  $\chi^2$  vs SNR

Figure 6.4: Results obtained in case 3 of the 2EF considering the PSNR and the reduced  $\chi^2$  as performance metrics. In this case the simulations are obtained using PhoSim and quadratic registration is employed for image alignment.

ously presented. The comparison between these curves and those corresponding to the 1EF also proves the existence of a reduction in the performance of the four multi-frame super-resolution algorithms. All details about this performance reduction will be discussed in depth in following sections.

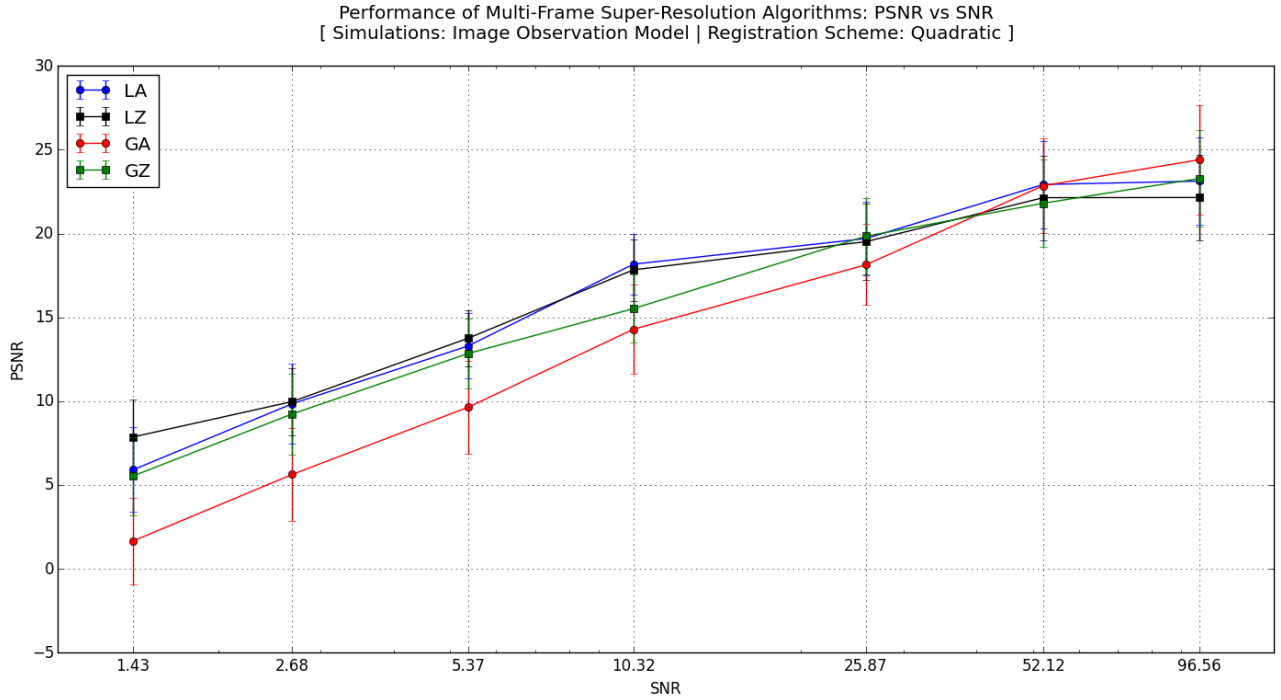
## 6.2.4 Case 4: Image observation model and quadratic registration

Performance results obtained for each one of the four multi-frame super-resolution algorithms in case 4 of the 2EF, where simulations were obtained using the IOM and quadratic registration was employed for image alignment, are presented in Figure 6.5a for the case of the PSNR, and in Figure 6.5b for the case of the reduced  $\chi^2$ . All values presented in the curves of both plots are detailed in Table A.5.

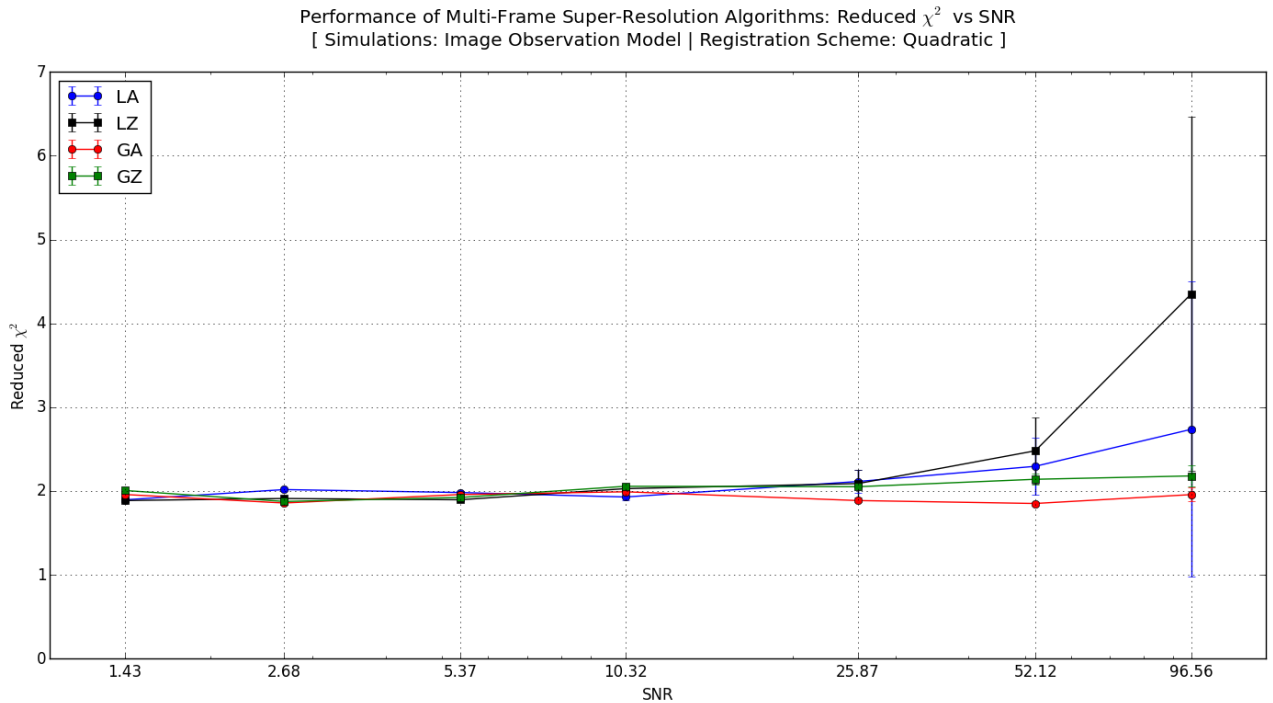
In the fourth and final case of the 2EF, the same general tendencies previously described can be noticed for both performance metrics. For the PSNR, all the curves show an increase in the value of this metric as the SNR grows. Also, the ratio between the size of the error bars and the corresponding PSNR value decreases as the SNR increases, which is associated to an improvement in the stability of the algorithms when the noise level is lower in the input images. In the case of the algorithms that use the gradient prior, we can notice that GZ presents a better performance than GA for SNR values equal or smaller than 25.87, while GA achieves better results than GZ for higher SNR values. In the case of the other two algorithms, the performance of LZ is better than the performance of LA for the three smallest values of the considered SNR range, while LA performs better than LZ for SNR values higher or equal than 10.32. It can be also noticed in these PSNR curves that the algorithms that use the Laplacian prior achieve better results when high levels of noise are considered.

For the reduced  $\chi^2$  curves we can also notice the same general behavior described in previous cases. The values corresponding to the curves of GA and GZ oscillate between 1.851 and 2.180, with an slight tendency to increase in the case of GZ and with an slight tendency to decrease in the case of GA. Moreover, the reduced  $\chi^2$  values corresponding to LA and LZ oscillate between 1.886 and 2.113 for SNR values equal or smaller than 25.87. For the two highest values of the SNR range, the curves of LA and LZ present the same considerable growth observed in previous cases. Here, LA and LZ reach reduced  $\chi^2$  values corresponding to 2.736 and 4.352 for the highest SNR value. Finally, it can be noticed that in each one of the four curves the size of the error bars increases as the SNR grows.

Again, the comparison between these results and those obtained in the 1EF, considering both metrics, indicates a reduction in the performances achieved by the four multi-frame super-resolution algorithms. An estimation of this performance reduction, considering each one of the four cases of the 2EF, is later presented, along with a discussion about the reasons that explain such situation.



(a) PSNR vs SNR



(b) Reduced  $\chi^2$  vs SNR

Figure 6.5: Results obtained in case 4 of the 2EF considering the PSNR and the reduced  $\chi^2$  as performance metrics. In this case the simulations are obtained using the IOM and quadratic registration is employed for image alignment.

### 6.3 Comparison between results of both frameworks

A major concern of this thesis, according to what has been mentioned in the goals, is to understand how the performance results change when we compare both experimental frameworks, since they represent different circumstances under which the algorithms were tested. In the 1EF, the registration and blur parameters were provided to each one of the algorithms, since these parameters were known from the simulation process, in order to obtain a measure of their performances under ideal circumstances. On the other hand, in each one of the four cases of the 2EF, such parameters were estimated using two registration procedures, affine and quadratic, along with the PSF-approximation process that was previously presented. The values obtained from these estimation mechanisms always present some degree of error, since their operation can be affected by many distorting effects, noise being the most relevant one. Therefore, the performance curves obtained for both metrics in the 2EF correspond to a more realistic setting, since these performance results are affected by the errors introduced during the estimation of the registration and blur parameters, as it happens in practice.

Ideally, the comparison between the results of both experimental frameworks should be made considering exactly the same range of SNR values. As we mentioned before, due to technical limitations associated to the employment of PhoSim, we were not able to obtain simulations with this tool for the exact same SNR range selected in the 1EF. Nevertheless, the SNR range of the 2EF is close enough to the SNR range of the 1EF, in terms of the sampling and the magnitude of the values, so the comparison is still possible but not optimal.

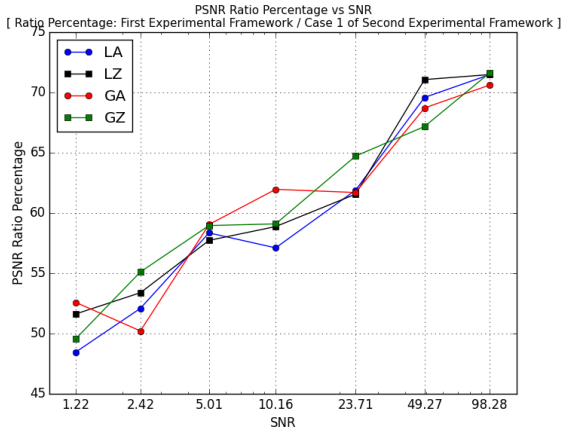
As it was previously mentioned, during the analysis of the results obtained in the 2EF, there is a reduction in the algorithms' performance that we want to estimate by comparing the results of both experimental frameworks. In order to do this, the ratio of the PSNR and the (Reduced  $\chi^2 - 1$ ) was computed between the values obtained in each one of the cases of the 2EF and the corresponding values of the 1EF. It is important to remember that the optimal value expected for the Reduced  $\chi^2$  is 1 and, as consequence, the ratio for this performance metric should be computed using the deviations from the optimal value instead of the actual value obtained for the metric.

The existence of the performance reduction was in evidence because the PSNR values obtained in the 2EF were smaller than those obtained in the 1EF, while the Reduced  $\chi^2$  values obtained in the 2EF were larger than those obtained in the 1EF. As a consequence, and since the ratios were computed as percentages, the PSNR ratio and the (Reduced  $\chi^2 - 1$ ) ratio will be smaller and larger than 100%, respectively, in all the analyzed cases.

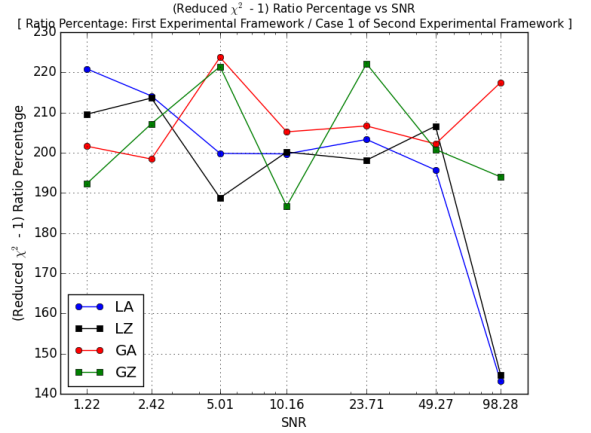
Below we introduce eight plots with the results obtained after computing the ratios according to what was previously mentioned. For each one of the four comparisons, between the results of each one of the four cases of the 2EF and the results of the 1EF, we present two plots, where the first one shows the curves obtained for the PSNR ratio and the second one shows the curves obtained for the (Reduced  $\chi^2 - 1$ ) ratio. All these curves are presented as a function of the SNR. The SNR values employed in the x-axis correspond to the average between the SNR values of both experimental frameworks, since we do not have a perfect coincidence between the SNR ranges of the 1EF and the 2EF.

### 6.3.1 Comparison between results of the 1EF and the case 1 of the 2EF

The ratio percentages computed from the comparison between the results obtained in the case 1 of the 2EF and those obtained in the 1EF are presented in Figure 6.6a for the PSNR ratio percentage, and in Figure 6.6b for the (Reduced  $\chi^2 - 1$ ) ratio percentage. All the values used to obtain these plots are detailed in Table A.6. It is important to remember that, in case 1 of the 2EF, the low-resolution images were simulated using PhoSim, while the registration parameters were estimated using affine registration.



(a) PSNR ratio vs SNR



(b) (Reduced  $\chi^2 - 1$ ) ratio vs SNR

Figure 6.6: Ratios computed between the results obtained for the PSNR and the (Reduced  $\chi^2 - 1$ ) in the 1EF and in case 1 of the 2EF.

The four curves in the PSNR ratio plot present a steady growth as the SNR increases. For the smallest SNR value, which corresponds to 1.22, the curves are around 50%, while for the highest SNR value, which corresponds to 98.28, the curves are around 71%. This means that the performance reduction of the algorithms decreases as the SNR grows, which is an expected behavior since the accuracy achieved by the registration methods and the PSF-approximation procedure should be improved if lower levels of noise are considered.

On the other hand, the (Reduced  $\chi^2 - 1$ ) ratio remains relatively stable and oscillates around 200% in the four curves without any specific tendency, regardless of the SNR value. For the highest value of the SNR range, the curves corresponding to LA and LZ present a substantial decrease, reaching values around 144%. This behavior seems to be related with the growth observed in the reduced  $\chi^2$  for the highest SNR values in the four cases of the 2EF and, also, in the 1EF. Therefore, this decrease in the (Reduced  $\chi^2 - 1$ ) ratio does not necessarily mean that the performance reduction corresponding to LA and LZ is smaller for a SNR value of 98.28, since the results obtained for the reduced  $\chi^2$  were not optimal in both cases.

### 6.3.2 Comparison between results of the 1EF and the case 2 of the 2EF

The ratio percentages computed from the comparison between the results obtained in the case 2 of the 2EF and those obtained in the 1EF are presented in Figure 6.7a for the PSNR ratio percentage, and in Figure 6.7b for the (Reduced  $\chi^2 - 1$ ) ratio percentage. All the values used to obtain these plots are detailed in Table A.7. It is important to remember that, in case 2 of the 2EF, the low-resolution images were simulated using the IOM while the registration parameters were estimated using affine registration.

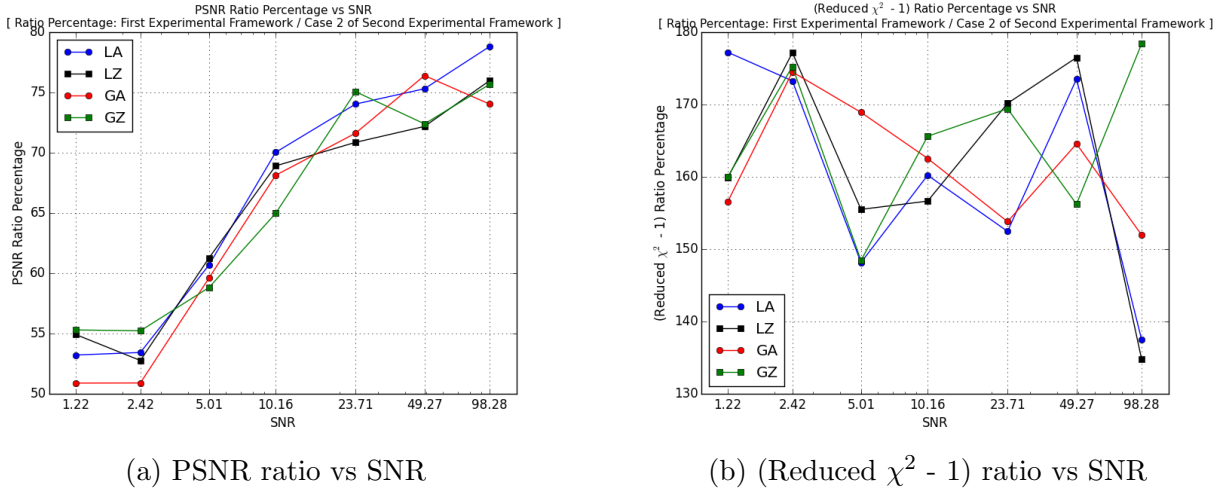


Figure 6.7: Ratios computed between the results obtained for the PSNR and the (Reduced  $\chi^2 - 1$ ) in the 1EF and in case 2 of the 2EF.

The four curves in the PSNR ratio plot present an steady growth as the SNR increases. For the smallest SNR value, which corresponds to 1.22, the curves are around 53%, while for the highest SNR value, which corresponds to 98.28, the curves are around 77%. This means that the performance reduction of the algorithms decreases as the SNR grows, which is an expected behavior since the accuracy achieved by the registration methods and the PSF-approximation procedure should be improved if lower levels of noise are considered.

On the other hand, the (Reduced  $\chi^2 - 1$ ) ratio remains relatively stable and oscillates around 165% in the four curves without any specific tendency, regardless of the SNR value. For the highest value of the SNR range, the curves corresponding to LA and LZ present a substantial decrease, reaching values around 136%. This behavior seems to be related with the growth observed in the reduced  $\chi^2$  for the highests SNR values in the four cases of the 2EF and, also, in the 1EF. Therefore, this decrease in the (Reduced  $\chi^2 - 1$ ) ratio does not necessarily mean that the performance reduction corresponding to LA and LZ is smaller for a SNR value of 98.28, since the results obtained for the reduced  $\chi^2$  were not optimal in both cases.

### 6.3.3 Comparison between results of the 1EF and the case 3 of the 2EF

The ratio percentages computed from the comparison between the results obtained in the case 3 of the 2EF and those obtained in the 1EF are presented in Figure 6.8a for the PSNR ratio percentage, and in Figure 6.8b for the (Reduced  $\chi^2 - 1$ ) ratio percentage. All the values used to obtain these plots are detailed in Table A.8. It is important to remember that, in case 3 of the 2EF, the low-resolution images were simulated using PhoSim while the registration parameters were estimated using quadratic registration.

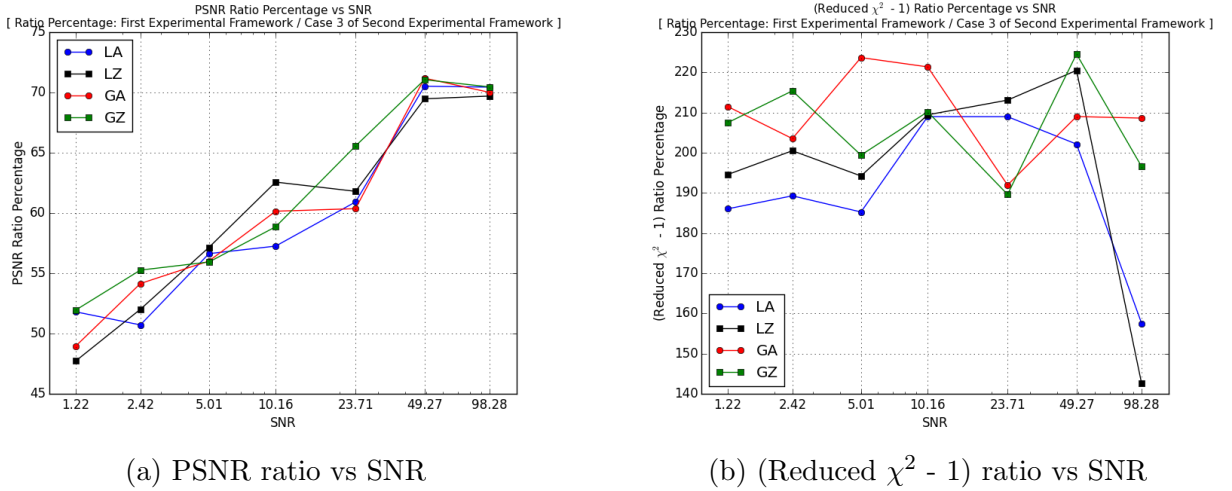


Figure 6.8: Ratios computed between the results obtained for the PSNR and the (Reduced  $\chi^2 - 1$ ) in the 1EF and in case 3 of the 2EF.

The four curves in the PSNR ratio plot present an steady growth as the SNR increases. For the smallest SNR value, which corresponds to 1.22, the curves are around 49%, while for the highest SNR value, which corresponds to 98.28, the curves are around 70%. This means that the performance reduction of the algorithms decreases as the SNR grows, which is an expected behavior since the accuracy achieved by the registration methods and the PSF-approximation procedure should be improved if lower levels of noise are considered.

On the other hand, the (Reduced  $\chi^2 - 1$ ) ratio remains relatively stable and oscillates around 200% in the four curves without any specific tendency, regardless of the SNR value. For the highest value of the SNR range, the curves corresponding to LA and LZ present a substantial decrease, reaching values around 150%. This behavior seems to be related with the growth observed in the reduced  $\chi^2$  for the highests SNR values in the four cases of the 2EF and, also, in the 1EF. Therefore, this decrease in the (Reduced  $\chi^2 - 1$ ) ratio does not necessarily mean that the performance reduction corresponding to LA and LZ is smaller for a SNR value of 98.28, since the results obtained for the reduced  $\chi^2$  were not optimal in both cases.

### 6.3.4 Comparison between results of the 1EF and the case 4 of the 2EF

The ratio percentages computed from the comparison between the results obtained in the case 1 of the 2EF and those obtained in the 1EF are presented in Figure 6.9a for the PSNR ratio percentage, and in Figure 6.9b for the (Reduced  $\chi^2 - 1$ ) ratio percentage. All the values used to obtain these plots are detailed in Table A.9. It is important to remember that, in case 4 of the 2EF, the low-resolution images were simulated using the IOM while the registration parameters were estimated using quadratic registration.

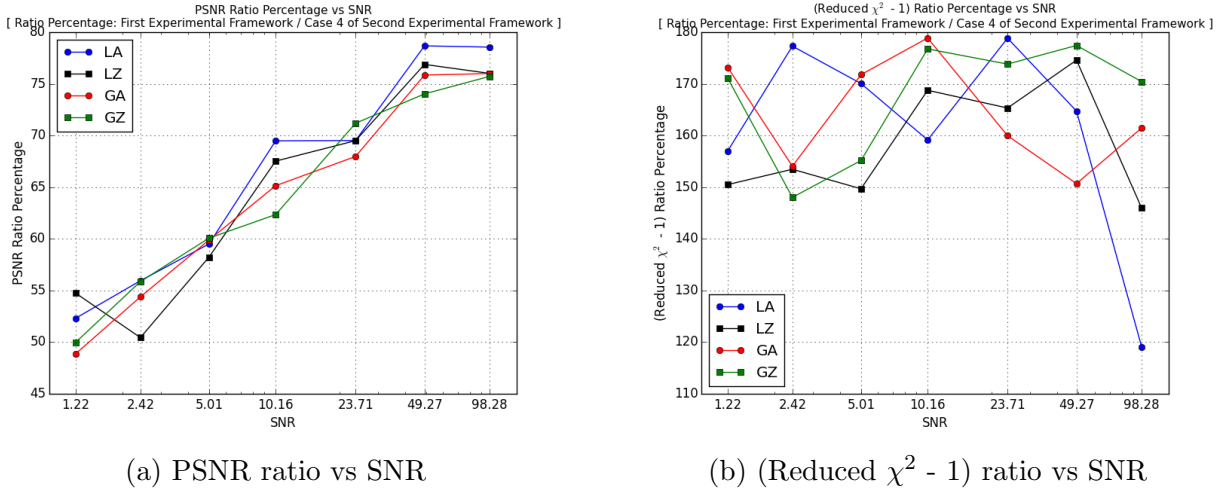


Figure 6.9: Ratios computed between the results obtained for the PSNR and the (Reduced  $\chi^2 - 1$ ) in the 1EF and in case 4 of the 2EF.

The four curves in the PSNR ratio plot present an steady growth as the SNR increases. For the smallest SNR value, which corresponds to 1.22, the curves are around 53%, while for the highest SNR value, which corresponds to 98.28, the curves are around 77%. This means that the performance reduction of the algorithms decreases as the SNR grows, which is an expected behavior since the accuracy achieved by the registration methods and the PSF-approximation procedure should be improved if lower levels of noise are considered.

On the other hand, the (Reduced  $\chi^2 - 1$ ) ratio remains relatively stable and oscillates around 165% in the four curves without any specific tendency, regardless of the SNR value. For the highest value of the SNR range, only the curve corresponding to LA presents a substantial decrease reaching a value of 119% (in the three previous comparisons such decrease is observed in the curves of LA and LZ). Nevertheless, this behavior, now only for LA, seems to be also related with the growth observed in the reduced  $\chi^2$  for the highests SNR values in the four cases of the 2EF and, also, in the 1EF. Therefore, this decrease in the (Reduced  $\chi^2 - 1$ ) ratio does not necessarily mean that the performance reduction corresponding to LA is smaller for a SNR value of 98.28, since the results obtained for the reduced  $\chi^2$  were not optimal.

## 6.4 Comparison between results of the second experimental framework

In previous sections the results obtained in the 1EF and in the four cases of the 2EF were presented. The results obtained in each one of these four cases were compared against the one obtained in 1EF by computing the ratios of the PSNR and the (Reduced  $\chi^2 - 1$ ), in order to estimate the magnitude of the performance reduction. The ranges of values obtained in each one of these four comparisons indicate that the magnitude of the performance reduction is highly influenced by the mechanism employed for simulating the low-resolution images. This explains why the results obtained in the first and the third comparison, where the ratios are computed between the results of the cases 1 and 3 of the 2EF and the results of the 1EF, are very similar, since in both cases PhoSim was used for the simulation of images. The same happens with the second and the four comparison, where the ratios are computed between the results of the cases 2 and 4 of the 2EF and the results of the 1EF, since in both cases the IOM was used for image simulation.

The results corresponding to the comparison between the four cases that made up the 2EF are now introduced. This comparison is also performed considering the ratios for the PSNR and the (Reduced  $\chi^2 - 1$ ) for the cases with the same simulation scheme (PhoSim or IOM) and for the cases with the same simulation approach (affine or quadratic). This, besides enabling us to check the validity of the hypothesis that the simulation tool employed has a strong influence over the magnitude of the reduction in the algorithms' performance, allows us to analyze the influence of the different registration procedures in the obtained results.

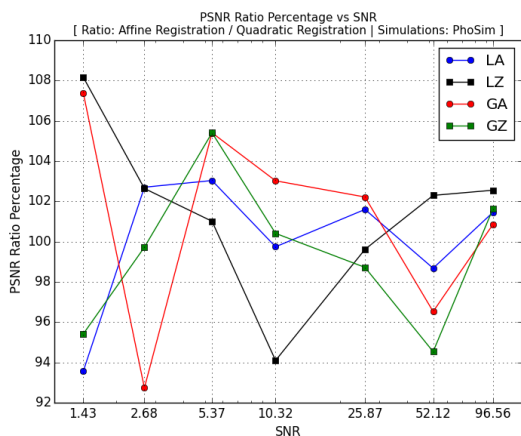
### 6.4.1 Comparison of results with the same simulation scheme

Here, the results obtained by computing the ratios between the values of the PSNR and (Reduced  $\chi^2 - 1$ ) are introduced, corresponding to cases 1 and 3 of the 2EF, to then review the same ratios for cases 2 and 4. In both cases, the compared results were obtained using the same simulation scheme, PhoSim in the first case (cases 1 and 3) and the IOM in the second one (cases 2 and 4). Therefore, this means that different registration approaches are actually being compared, since the simulation scheme is common between the considered cases.

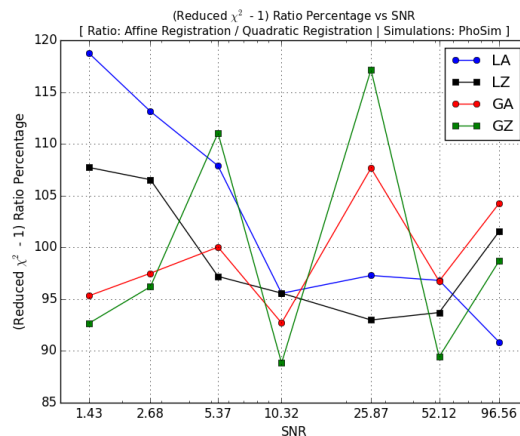
The results corresponding to the ratios between cases 1 and 3 are presented in Figure 6.10a for the PSNR, and in Figure 6.10b for the (Reduced  $\chi^2 - 1$ ). In both cases, PhoSim was the scheme employed to simulate the low-resolution images. These results represent the comparison between the performances achieved by the algorithms using different registration approaches, since affine registration was employed for case 1 and quadratic registration was employed for case 3.

The values obtained for both ratios oscillate around 100% without any specific tendency, which means that the algorithms' performance is not affected by the registration method employed. Since a clear tendency cannot be established in these results, the only possible interpretation corresponds to consider that both registration procedures achieve similar accuracies, which implies that the errors they introduce in the reconstruction process have

the same magnitude for the same image simulation scheme, regardless of the SNR value considered.



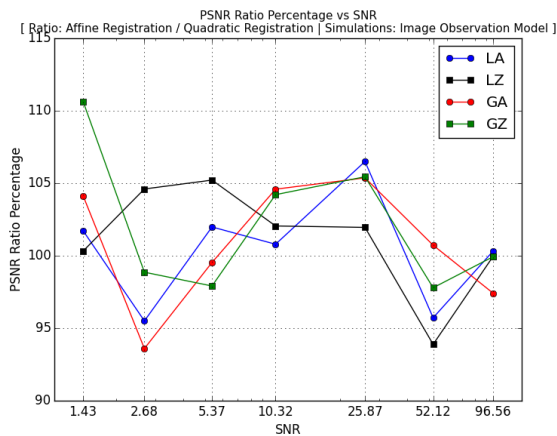
(a) PSNR ratio vs SNR



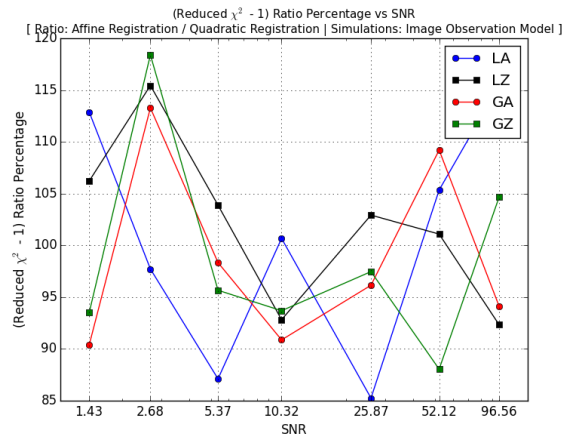
(b) (Reduced  $\chi^2 - 1$ ) ratio vs SNR

Figure 6.10: Ratios computed between the results obtained for the PSNR and the (Reduced  $\chi^2 - 1$ ) in cases 1 and 3 of the 2EF.

The results corresponding to the ratios between cases 2 and 4 are presented in Figure 6.11a for the PSNR, and in Figure 6.11b for the (Reduced  $\chi^2 - 1$ ). In both cases, IOM was the scheme employed to simulate the low-resolution images. These results represent the comparison between the performances achieved by the algorithms using different registration approaches, since affine registration was employed for case 2 and quadratic registration was employed for case 4.



(a) PSNR ratio vs SNR



(b) (Reduced  $\chi^2 - 1$ ) ratio vs SNR

Figure 6.11: Ratios computed between the results obtained for the PSNR and the (Reduced  $\chi^2 - 1$ ) in cases 2 and 4 of the 2EF.

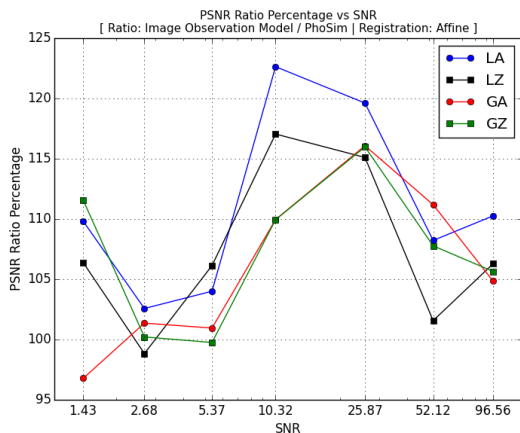
Here, as in the previous comparison, the values obtained for both ratios oscillate around 100% without any specific trend. Then, it can be concluded again that the registration method used does not affect the performance of the different algorithms, since the errors

introduced by affine and quadratic registration have similar values if the same simulation scheme was considered, regardless of the SNR values considered.

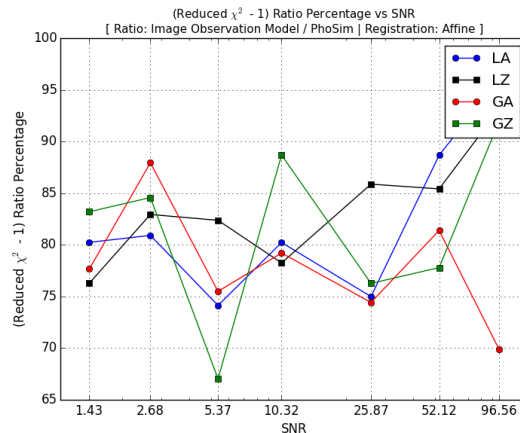
In summary, the results of the two comparisons presented here indicate that the registration procedure employed for motion estimation does not have a significant influence over the performance results achieved by the different algorithms. In fact, these results suggest that both registration mechanisms have similar performances, since no evidence indicating that one of the algorithms yields better results was obtained.

## 6.4.2 Comparison of results with the same registration procedure

The same comparison is now presented between cases where the same registration approach is employed. This allows us to compare the influence of the two simulation schemes considered, when the same registration procedure is used. These results were also obtained by computing the ratios between the values of the PSNR and (Reduced  $\chi^2 - 1$ ) corresponding, in this opportunity, to cases 2 and 1 of the 2EF, to then review the same ratios for cases 4 and 3. In the first comparison, both cases employed affine registration (cases 2 and 1), while in the second one both cases employed quadratic registration (cases 4 and 3). It is important to notice that the ratio is comparing the performance achieved by the algorithms when the IOM is used in the simulation process, against the performance achieved when PhoSim is used to obtain the low-resolution images.



(a) PSNR ratio vs SNR



(b) (Reduced  $\chi^2 - 1$ ) ratio vs SNR

Figure 6.12: Ratios computed between the results obtained for the PSNR and the (Reduced  $\chi^2 - 1$ ) in cases 2 and 1 of the 2EF.

The results corresponding to the ratios between cases 2 and 1 are presented in Figure 6.12a for the PSNR, and in Figure 6.12b for the (Reduced  $\chi^2 - 1$ ). Here we can notice that almost all the values of the PSNR ratio are larger than 100%, which means that the performance of the algorithms is better when the images are simulated using the IOM instead of PhoSim. This is totally expected, since the algorithms are based in the IOM and, as a consequence, they should work better with low-resolution images generated with such simulation scheme. It is interesting to note that, for the PSNR ratio, the algorithms present better performances

for middle SNR values (such as 10.32 and 25.87) than they do for the extreme values of the considered SNR range.

On the other hand, the values obtained for the (Reduced  $\chi^2 - 1$ ) ratios are stable and they oscillate, without any specific tendency, around 80%. This means that the multi-frame super-resolution algorithms achieve better performances when IOM is employed to simulate images, which is consistent with what was observed for the PSNR ratios. Therefore, in terms of the deviation of the reduced  $\chi^2$  from 1, the algorithms are working 20% worse when PhoSim is employed to simulate images than what they do when the IOM is used.

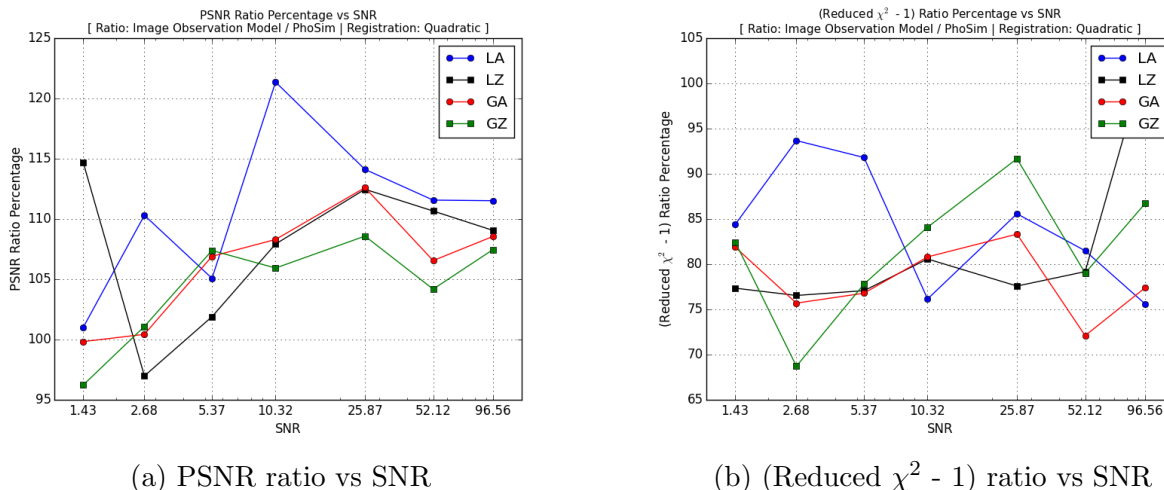


Figure 6.13: Ratios computed between the results obtained for the PSNR and the (Reduced  $\chi^2 - 1$ ) in cases 4 and 3 of the 2EF.

The results corresponding to the ratios between cases 4 and 3 are presented in Figure 6.13a for the PSNR, and in Figure 6.13b for the (Reduced  $\chi^2 - 1$ ). In this second comparison of the cases where the same registration procedure was employed we can notice again that almost all the PSNR ratio values are larger than 100%, which means that the performance of the algorithms is again better when the images are simulated with the IOM instead of PhoSim. In this case we can notice a steady increase in the values of the PSNR ratios as the SNR grows, from around 100% for the smallest SNR values to around 110% for the highest SNR values of the range. Unlike the previous comparison, a significant growth of the PSNR ratios for middle SNR values is not observed here.

For the values obtained for the (Reduced  $\chi^2 - 1$ ) ratios we can notice the same behavior observed in the previous comparison, where the curves of each one of the four multi-frame super-resolution algorithms oscillate, without any specific tendency, around 80%. Therefore, we can notice again that the algorithms are working 20% worse when PhoSim is employed to simulate images than when the IOM is used.

The two sets of results reviewed for both comparisons are totally consistent between them, and they are also consistent with the results obtained from the comparisons between cases where the same simulation tool was employed and that were presented previously. The reason to conclude this comes from the fact that the same behavior was noticed in the curves obtained in both comparisons for almost an identical range of values, where we observed an increase

of the PSNR ratio from percentages around 100% to percentages around 110% as the SNR grows, and (Reduced  $\chi^2 - 1$ ) ratio values oscillating around 80%. This common behavior was observed in spite of the fact that different registration procedures were employed in the two cases of the 2EF considered in each comparison, which means that the registration procedure does not have a significant influence over the results achieved by the algorithms. Such conclusion was also obtained from the analysis of the ratios obtained for the comparisons previously reviewed, where cases with the same simulation scheme but different simulation tools were considered.

The common behavior observed for both cases also validates the fact that the simulation scheme employed has a strong influence over the results obtained, which was also a conclusion derived from the analysis of the comparisons presented for the cases with different registration procedures. The behavior observed for the PSNR ratios indicates that the algorithms work with similar accuracies when there are high levels of noise in the images but, when the noise is low, the algorithms achieve better results with images simulated using the IOM than what they achieve with images simulated with PhoSim. Thus, although the influence of the simulation tool employed is very relevant, such influence depends on the SNR and it can be noticed only if the amount of noise contained in the low-resolution images is not that high. Moreover, in terms of the (Reduced  $\chi^2 - 1$ ) ratios, the strong influence of the simulation scheme is also noticeable but, in this case, it does not present a dependency on the SNR, since the values corresponding to these ratios oscillate around a stable value regardless of the SNR value considered.

## 6.5 Examples of reconstructed images

Here we present some examples of high-resolution images reconstructed by each one of the four multi-frame super-resolution algorithms in order to have a graphical notion of how these algorithms work. In Figures 6.14, 6.15, and 6.16 we can see three examples of reconstructions performed in case 3 of the 2EF, for SNR values corresponding to 5.37, 25.87 and 96.56, respectively. In each one of these examples, all images involved in the reconstruction process are presented, including the high-resolution image employed as template, one example of the simulated low-resolution images used as input, and the four images reconstructed by each one of the algorithms. Also, the differences obtained from subtracting the high-resolution template with the four reconstructed images are presented, along with the differences obtained from subtracting the low-resolution image, showed as an example, with the degraded versions of the four reconstructed images. Each one of these eight differences was obtained after registering and normalizing the pair of images required for computing such differences and, as consequence, the errors associated with the operation of the registration process also affect all these differences.

In Figure 6.14 we can see the images reconstructed by each algorithm for a relatively small SNR value corresponding to 5.37, which means that the low-resolution images used for the obtention of these reconstructed images were affected by important levels of noise. As a consequence, the presence of multiple artifacts can be noticed in each one of the reconstructed images, these artifacts being introduced into the reconstructed images by the regularized

approach employed by the algorithms. For the SNR value considered, the image reconstructed by GA (see Figure 6.14e) is the worst one between the set of four reconstructed images, since the presence of artifacts severely affects its quality. This is consistent with the PSNR results previously presented for case 3 of the 2EF (see 6.4a), where it can be observed that GA has the worst performance of the four multi-frame super-resolution algorithms for small SNR values. In fact, this situation can be also observed in the results obtained in the 1EF and in all the other cases of the 2EF.

In the comparison between the images obtained with algorithms that use the same prior term, it can be noticed that the images reconstructed by the algorithms that employ Zomet's approximation are less corrupted by artifacts than the images reconstructed by their counterparts that use the analytical expression for computing the gradient. Therefore, the results presented in Figure 6.14 are consistent with the fact that Zomet's approximation is the best choice for reconstructing images when high levels of noise affect the low-resolution images used as input by the algorithms.

Moreover, the eight differences obtained show that Laplacian prior represents the best option for processing sets of low-resolution images with high levels of noise. This can be observed in the fact that the differences computed using the images reconstructed by LA and LZ have a higher degree of smoothness than what happens with the differences computed employing the images reconstructed by GA and GZ. The degree of smoothness can be observed in these images considering the contrast of the noise that is present on the background, which is more intense in the case of the differences corresponding to GA and GZ than what it is in the case of the differences obtained using LA and LZ.

In Figure 6.15 we can see the images reconstructed by each algorithm for a middle SNR value corresponding to 25.87. In each one of the four reconstructed images it can be noticed that the noise was removed by all the algorithms, since now there are not artifacts like the ones observed in the group of images previously reviewed. This is completely expected since the amounts of noise considered in this example are smaller than those considered in the previous one (where the SNR value describing the amount of noise in the images was 5.37).

A relevant aspect that can be clearly observed in this second set of images is that the levels of blur that are present in the reconstructed images are still significant. In each one of the differences the presence of *rings* around the location of each point source (star) can be noticed, which shows that the PSF estimated for this reconstruction process was not optimal. Since we can observe rings of similar sizes in both groups of differences, those obtained using the high-resolution template and those obtained using the low-resolution image example, it can be concluded that the FWHM of the PSF in the reconstructed images is smaller than the FWHM of the PSF in the low-resolution image example but larger than the FWHM of the PSF in the high-resolution template. This situation shows how the errors in the estimation of the blur parameters affect the quality of the reconstructed images, even if the amount of noise that corrupts the set of low-resolution images is not substantially high.

In Figure 6.16 we can see the images reconstructed by each algorithm for the highest value in the SNR range corresponding to 96.56. In this case we can notice that the size of the rings observed in the differences computed using the high-resolution template is clearly smaller than the size of the rings observed in the differences obtained employing the low-resolution

image example. This indicates that the degree of error associated to the estimation of the FWHM of the PSF is lower here than in the previous case, which is totally expected since the accuracy of the estimation of the FWHM of the PSF should be better as the SNR grows.

With this third group of reconstructed images we can have a graphical notion of the degree of blur that corrupts the reconstructed images by observing the spiral galaxy (extended source) that is contained in such images. The arms of the galaxy can be seen in the reconstructed images with more detail than it can be done in the low-resolution image example, although such level of detail is still lower than the one of the high-resolution template. Nevertheless, the comparison between the two groups of differences indicates that a great amount of information is actually recovered by the reconstruction process, since in the differences obtained using the low-resolution image example we can identify multiple structural details of the galaxy that can not be observed in the other group of differences computed employing the high-resolution template. This entails that there is a great degree of similarity between the high-resolution images and their corresponding common high-resolution template, which is completely expected since the amount of noise that corrupts the low-resolution images and affects the operation of the multi-frame super-resolution algorithms is negligible.

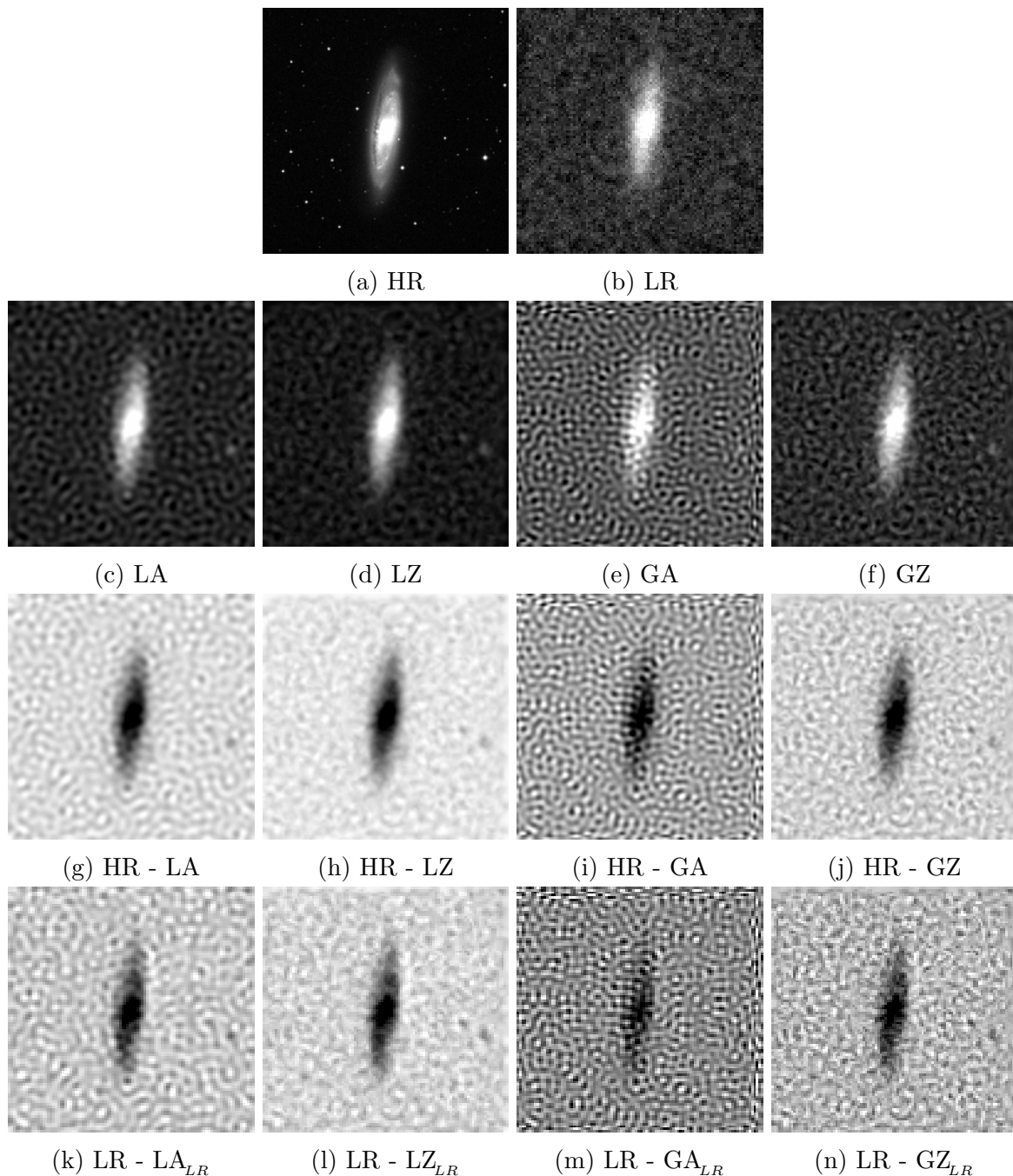


Figure 6.14: Images involved in one example of the reconstruction processes of the case 3 of the 2EF for a SNR value of 5.37. The high-resolution (HR) template employed for simulating low-resolution images with PhoSim is showed in (a), while an example of these simulated low-resolution (LR) images is presented in (b). In (c), (d), (e) and (f) the images reconstructed by LA, LZ, GA and GZ are respectively displayed. The differences obtained from subtracting the high-resolution template (a) with the images reconstructed by LA, LZ, GA and GZ, after registering each pair of images, are respectively showed in (g), (h), (i) and (j). The differences obtained from subtracting the low-resolution image example (b) with the degraded versions of the the images reconstructed by LA, LZ, GA and GZ, after registering each pair of images, are respectively presented in (k), (l), (m) and (n).

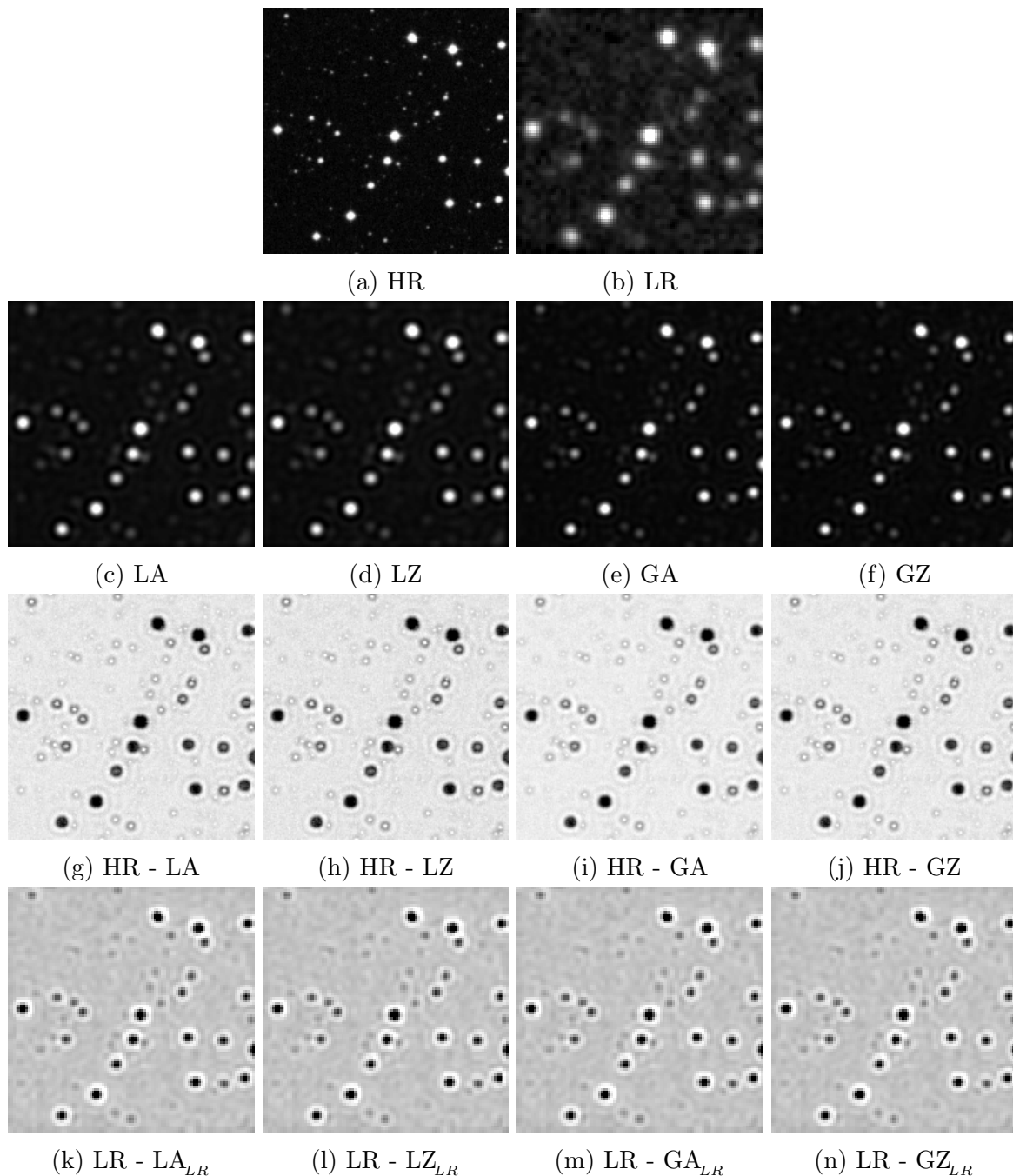


Figure 6.15: Images involved in one example of the reconstruction processes of the case 3 of the 2EF for a SNR value of 25.87. The high-resolution (HR) template employed for simulating low-resolution images with PhoSim is showed in (a), while an example of these simulated low-resolution (LR) images is presented in (b). In (c), (d), (e) and (f) the images reconstructed by LA, LZ, GA and GZ are respectively displayed. The differences obtained from subtracting the high-resolution template (a) with the images reconstructed by LA, LZ, GA and GZ, after registering each pair of images, are respectively showed in (g), (h), (i) and (j). The differences obtained from subtracting the low-resolution image example (b) with the degraded versions of the the images reconstructed by LA, LZ, GA and GZ, after registering each pair of images, are respectively presented in (k), (l), (m) and (n).

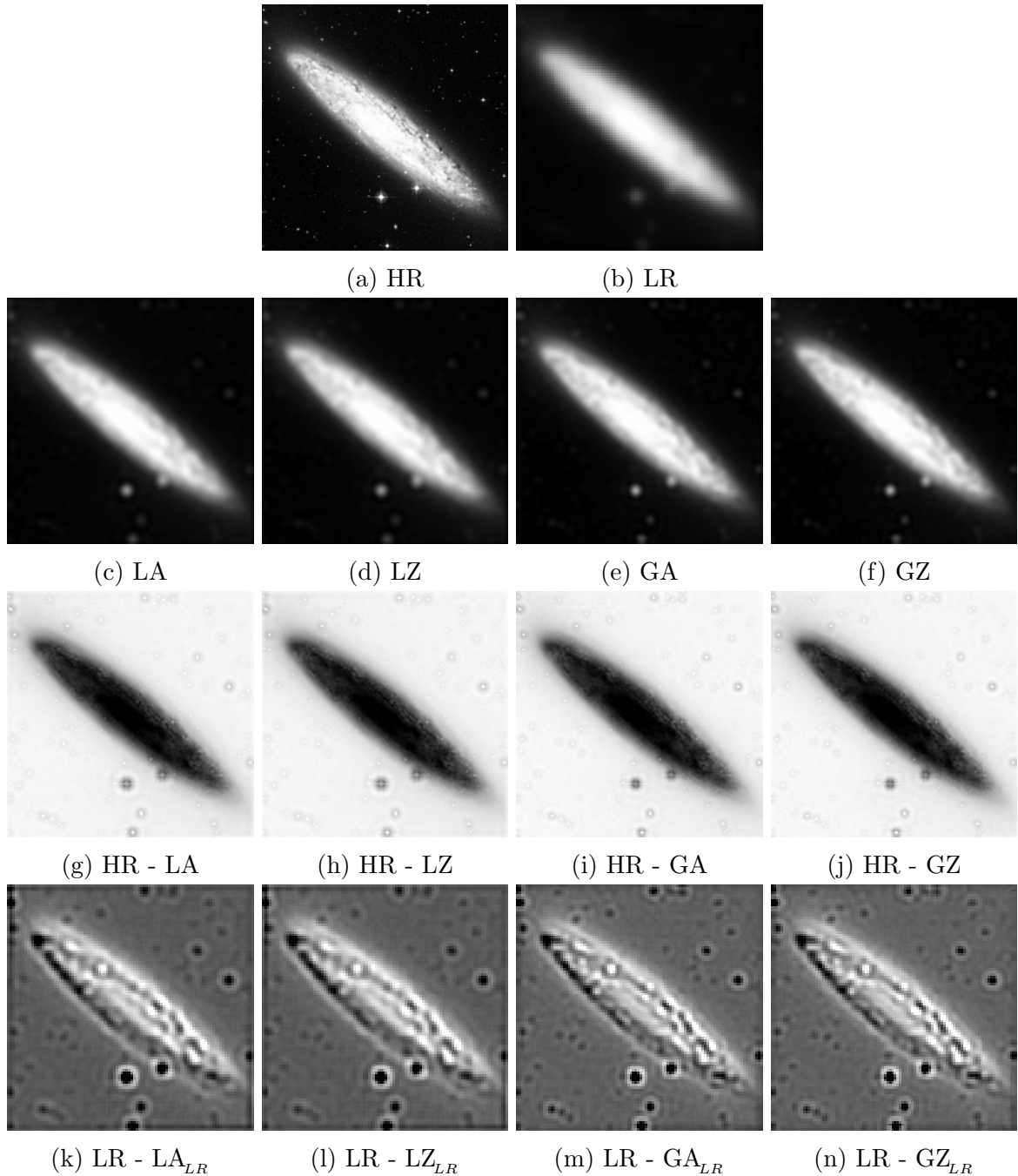


Figure 6.16: Images involved in one example of the reconstruction processes of the case 3 of the 2EF for a SNR value of 96.56. The high-resolution (HR) template employed for simulating low-resolution images with PhoSim is showed in (a), while an example of these simulated low-resolution (LR) images is presented in (b). In (c), (d), (e) and (f) the images reconstructed by LA, LZ, GA and GZ are respectively displayed. The differences obtained from subtracting the high-resolution template (a) with the images reconstructed by LA, LZ, GA and GZ, after registering each pair of images, are respectively showed in (g), (h), (i) and (j). The differences obtained from subtracting the low-resolution image example (b) with the degraded versions of the the images reconstructed by LA, LZ, GA and GZ, after registering each pair of images, are respectively presented in (k), (l), (m) and (n).

# Chapter 7

## Conclusions

In this final chapter we introduce the conclusions derived from the analysis of the multiple results obtained from the experiments of the First Experimental Framework (1EF) and each one of the four cases that made up the Second Experimental Framework (2EF). The purpose of these conclusions is to discuss the validity of the hypotheses that were posed for the different research questions associated to the goals of this thesis, and also summarize the most relevant ideas drawn from all the experiments that were carried out. Among the topics that are addressed in these conclusions we can mention the relation that exists between the algorithms' performance and the SNR, the best choice between the four algorithms for reconstructing high-resolution images as function of the SNR, the magnitude and the behavior of the performance reduction that can be observed in each one of the cases of the 2EF, and the comparison between the results achieved in the experiments considering different registration procedures.

We also present a comprehensive discussion about the main research directions that can be considered in future works, in order to expand the scope of the conclusions obtained in this thesis for the problem of studying the performance of the four multi-frame super-resolution algorithms when they are employed to reconstruct astronomical high-resolution images. In general, the ideas considered for these research directions suggest exploring the influence of the different procedures that participate, sometimes not in an explicit manner, in the reconstruction process.

### 7.1 Relation between performance and SNR

The first goal of this thesis consisted in figuring out the relation that exists between the performance of the four multi-frame super-resolution algorithms and the SNR value of the low-resolution images used as input in the reconstruction process. The hypothesis proposed suggests that the algorithms' performance should improve as the SNR grows, which means that the results achieved by the algorithms should enhance to the extent that the amount of noise that corrupts the images decreases. This was actually verified in each one of the experiments carried out in this thesis, but only in terms of the PSNR (see Figures 6.1a, 6.2a,

6.3a, 6.4a and 6.5a). Therefore, we can indeed conclude that every algorithm achieves better PSNR results as the SNR grows.

In terms of the reduced  $\chi^2$  we can not draw the same conclusion, since the results obtained in each experiment indicate that the values corresponding to this metric remain relatively stable regardless of the SNR value (see Figures 6.1b, 6.2b, 6.3b, 6.4b and 6.5b). This does not imply that the reconstruction process is not working properly, since the purpose of the reduced  $\chi^2$  is to reflect how well the reconstructed image reflects the information contained in the low-resolution images. Nevertheless, the behavior of the reduced  $\chi^2$  curves indicates that there is a limit in the degree of similarity that can exist between the reconstructed image and the low-resolution images, which seems to be counterintuitive since a growth in the degree of similarity would be expected if the SNR value increases.

To consider that the errors associated to the estimation of the blur and registration parameters explain the behavior of the reduced  $\chi^2$  would be a naive interpretation, since such behavior is also observed in the results corresponding to the 1EF, where these parameters were known beforehand. Therefore, according to the results obtained here, it can only be concluded that the performance of the four multi-frame super-resolution algorithms is stable and does not depend on the SNR value when such performance is measured using the reduced  $\chi^2$ . The only case where this conclusion is not valid is for LA and LZ when high SNR values are considered, since both algorithms show a significant growth in the reduced  $\chi^2$  for the two highest values of the SNR range. More experiments are required to fully understand the reasons behind this fact, but the most probable explanation is that the smoothing process derived from the usage of the Laplacian prior, whose aim is to remove noise, is excessively strict. Because of this, when only small amounts of noise are corrupting the low-resolution images, the Laplacian prior removes part of the signal that should be included in the reconstructed image in order to guarantee some degree of smoothness.

## 7.2 Best algorithms according to SNR values

Finding out which one of the four algorithms offers the best results as a function of the SNR values is the second goal stated in this thesis. The proposed hypothesis suggests that the algorithms that employ Zomet's approximation should have better performances than their counterparts, that use the analytical expression for computing the gradient, when small SNR values are considered. Besides, this hypothesis indicates that this relation is reversed for high SNR values, which means that the algorithms that use the analytical expression should achieve better results than those that employ Zomet's approximation if the noise corrupting the low-resolution images is small.

As it happened in the previous case, only the PSNR results obtained in the experiments validate, at least in a partial manner, the hypothesis corresponding to this second goal, since the expected behavior can be observed in the results of the 1EF and also in each one of the four cases that made up the 2EF. Moreover, the results corresponding to the reduced  $\chi^2$  do not coincide with what is stated in the hypothesis, since all the algorithms have similar performances according to the curves obtained for this metric. However, considering what

has been previously mentioned about what is actually being quantified by the reduced  $\chi^2$ , the particular behavior of this metric does not represent an invalidation of the conclusions derived from the hypothesis.

It is important to remember that Zomet’s approximation represents, according to theory, an alternative mechanism to compute an approximation of the gradient and that is supposed to be robust against the presence of noise. As a consequence of this, the results obtained using Zomet’s approximation should be better than those obtained using the analytical expression of the gradient when significant levels of noise are present in the set of low-resolution images. This is actually clearly observed in all the reviewed results (see Figures 6.1a, 6.2a, 6.3a, 6.4a and 6.5a), since LZ always achieves better PSNR results than LA, at least for the three smallest values in the SNR range considered in the 2EF (and that correspond to 1.43, 2.68 and 5.37) and also in the 1EF (and that correspond to 1.0, 2.15 and 4.64). The same happens with the algorithms that use the gradient prior but in a wider range, since GZ always presents better PSNR results than GA for the five smallest values in the SNR range considered in the 2EF (and that correspond to 1.43, 2.68, 5.37, 10.32, 25.87) and also in the 1EF (and that correspond to 1.0, 2.15, 4.64, 10.0 and 21.54). Therefore, we can conclude that the first part of the hypothesis, which refers to the behavior of the algorithms for small SNR values, is totally valid along with being completely consistent with theory.

The second part of the hypothesis, which refers to the behavior of the algorithms for high SNR values, can also be validated from the analysis of the PSNR results but without the same degree of certainty. The reason for this comes from the fact that the differences observed between the algorithms’ performances are larger for small SNR values than for high SNR values, which is completely expected because the operation of the algorithms should be close to the optimum if small amounts of noise are corrupting the low-resolution images. Therefore, it can be concluded that for high SNR values the algorithms that use the analytical expression of the gradient have a slightly better performance than the algorithms that use Zomet’s approximation. The main implication of this conclusion is the fact that Zomet’s approximation represents a very useful tool for recovering high-resolution images, since it has excellent results for small SNR values and because the loss of accuracy that can be observed for high SNR values, due to the approximation process, is not very significant in comparison with the PSNR results achieved by the algorithms that employ the analytical expression for computing the gradient.

In order to expand the conclusions presented here, we now discuss which algorithm presents the best performance according to the prior term selected for the cost function. It is important to mention again that this discussion is based only on the analysis of the PSNR results, since the curves obtained for the reduced  $\chi^2$  remain relatively stable around some specific value regardless of the SNR (except in the case of LA and LZ for two highest SNR values), and then they do not provide any information that can be used to determine which algorithm has the best performance (see Figures 6.1b, 6.2b, 6.3b, 6.4b and 6.5b).

In the 1EF, and practically in all the cases of the 2EF, it can be observed that the algorithms that use the Laplacian prior have better performances than their counterparts that use the gradient prior for the four smallest values of the SNR range. This relation is reversed, but with smaller differences between the performances, for the two highest SNR

values considered in both frameworks (which means that the gradient prior works better than the Laplacian one for high SNR values). For the SNR value located between the four smallest and the two highest values of the SNR ranges, which corresponds to 21.54 in the 1EF and to 25.87 in the 2EF, all the algorithms present similar PSNR results, thus it is not possible to clearly establish an order relation between their performances.

Finally, from a more specific analysis of the PSNR results, it can be concluded that LZ is the best choice for the four smallest values of the SNR ranges of both frameworks, while GA is the best choice for the two highest SNR values (being this completely clear in the results of the 1EF but less clear in the results obtained in the four cases of the 2EF). This is totally consistent with what has been previously concluded regarding the selection, as function of the SNR, of a mechanism for computing the gradient and a prior term for the cost function. In fact, LZ is the combination between the best option for computing the gradient and the best prior term that can be selected for small SNR values (Zomet's approximation and Laplacian prior), while GA is the combination between the best option for computing the gradient and the best prior term that can be selected for high SNR values (analytical expression of the gradient and gradient prior).

### 7.3 Performance reduction of the algorithms

The third goal posed in this thesis consisted in analyzing if the performance of the four multi-frame super-resolution algorithms decreases with the presence of errors in the values estimated for the blur and registration parameters. In order to accomplish such goal, the results obtained in the 1EF, which are not affected by the errors since the all the parameters are known beforehand, were compared with the results obtained in the four cases that made up the 2EF which are actually affected by the errors derived from the estimation process, since the blur and registration parameters were estimated using the PSF-approximation mechanism and both registration procedures.

The comparison mentioned was performed by computing the ratios between the values obtained for the PSNR and the (Reduced  $\chi^2$ ) in the four cases of the 2EF and in the 1EF. In each one of the four pairs of ratios that were yielded from this comparison, it can be observed that percentages corresponding to the PSNR ratios and the (Reduced  $\chi^2 - 1$ ) ratios are respectively smaller and larger than 100%. This implies that there is indeed a reduction in the performance of the algorithms, since the PSNR values achieved in the 2EF are smaller than those achieved in the 1EF and the deviations of the reduced  $\chi^2$  from 1 are larger in the 2EF than what they are in the 1EF. Therefore, the first conclusion that can be drawn from the analysis of the ratios corresponds to acknowledging that the errors derived from the process of estimating the blur and registration parameters entails a reduction in the performance of the four multi-frame super-resolution algorithms.

Although the performance reduction can be noticed in the ratios computed for both metrics, the dependency on the SNR observed in the PSNR ratios is different than the one observed in the (Reduced  $\chi^2 - 1$ ) ratios. In the case of the PSNR ratios, the performance reduction presents an explicit dependency on the SNR values since its magnitude decreases

as the SNR grows, while, in the case of the (Reduced  $\chi^2 - 1$ ) ratios, the reduction observed remains relatively stable regardless of the SNR.

The curves obtained for the PSNR ratios of case 1 of the 2EF show a steady increase, which seems to be linear, from percentages around 50% for a SNR value corresponding to 1.22, to percentages around 71% for a SNR value corresponding to 98.28, which means that the magnitude of the performance reductions decreases from 50% to 29% as the SNR grows between these pair of SNR values (see Figure 6.6a). The curves obtained for the PSNR ratios of case 3 of the 2EF also show a steady increase, which also seems to be linear, from percentages around 49% to percentages around 70% for the same pair of the SNR values previously mentioned (see Figure 6.8a). Therefore, for cases 1 and 3, the magnitude of the performance reduction computed in terms of the PSNR is very similar and behaves practically in the same manner in both cases. This can be noticed in the fact that the PSNR ratios obtained from the comparison of these two cases oscillate around 100% for all the values in the SNR range (see Figure 6.10a).

Something similar happens with the PSNR ratio curves obtained for cases 2 and 4 of the 2EF. A steady increase, which does not seem to be linear, can be observed in the PSNR ratio curves corresponding to case 2. This increase goes from percentages around 53% to percentages around 77% for the same pair of SNR values previously mentioned and which correspond to 1.22 and 98.28 (see Figure 6.7a). This means that the magnitude of the performance reduction decreases from 47% to 23% as the SNR grows between these two SNR values. Practically the same general behavior can be observed in the PSNR ratio curves obtained for case 4, since the growth of these curves goes also from percentages around 53% to percentages around 77% for the same pair of SNR values (see Figure 6.9a). Therefore, we again have very similar behaviors between two cases of the 2EF, which can be also observed in the fact that the percentages obtained for the PSNR ratios computed from the comparison of cases 2 and 4 oscillate around 100% (see Figure 6.11a).

The same correspondence between the results obtained for the two pairs of cases of the 2EF previously mentioned can be noticed in the (Reduced  $\chi^2 - 1$ ) ratios. For cases 1 and 3, the ratios oscillate around 200% without any specific tendency and regardless of the SNR (see Figures 6.6b and 6.8b), which means that the performance reduction, measured in terms of the deviation of the reduced  $\chi^2$  values from 1, has a magnitude of 100% for these two cases. For cases 2 and 3, the ratios oscillate around 165% without any particular behavior and regardless of the SNR (see Figures 6.7b and 6.9b), which means that the performance reduction for these two cases has a magnitude of 65% according to the ratios computed. The similarities between the behavior of the (Reduced  $\chi^2 - 1$ ) for cases 1 and 3 are consistent with the fact that the ratios computed from the comparison between these two cases correspond, essentially, to percentages that oscillate around 100% (see Figure 6.10b) The same situation can be observed for the ratios computed from the comparison between cases 2 and 4, since they also correspond to percentages that oscillate around 100% without any clear trend (see Figure 6.11b).

It can be concluded, in accordance with the foregoing, that the performance reduction, which affects the algorithms when the blur and registration parameters are estimated, presents a strong dependency on the simulation scheme employed for simulating the low-

resolution images of the input set. This is inferred from the fact that similar behaviors for the performance reduction are observed in the cases of the 2EF where the same simulation tool was employed. In cases 1 and 3 the low-resolution images were obtained using PhoSim, while in cases 2 and 4 the IOM was used for such task. Therefore, the magnitude of the performance reduction, when PhoSim is employed, decreases from 50% to 29% for the PSNR as the SNR grows from 1.22 to 98.28, while, in terms of the (Reduced  $\chi^2 - 1$ ), the magnitude of this reduction remains relatively stable around a value of 100% regardless of the SNR. Moreover, the magnitude of the performance reduction, when the IOM is used for image simulation, decreases from 47% to 23% for the PSNR as the SNR grows from 1.22 to 98.28, while, in terms of the (Reduced  $\chi^2 - 1$ ), the magnitude of this reduction remains relatively stable around a value of 65% regardless of the SNR.

The main implication derived from what has just been mentioned is given by the fact that the magnitude of the performance reduction, in terms of both metrics, is clearly smaller when the IOM is employed instead of PhoSim. These differences between the magnitude in performance reduction can be observed in PSNR and (Reduced  $\chi^2 - 1$ ) ratios computed between cases of the 2EF where the same registration procedure but different simulation tools were employed (see Figures 6.12 and 6.13). This conclusion is totally expected since the operation of the four multi-frame super-resolution algorithms is based on the IOM and, as a consequence, their performances should be better if the low-resolution images are obtained using this simulation scheme instead of PhoSim. Besides, multiple distortions, which are not even considered in the IOM, are included in the simulation process of PhoSim, thus the performance achieved by a reconstruction process using this simulation scheme is affected by the presence of these distortions.

## 7.4 Influence of the registration procedures

The purpose of the fourth and last goal of this thesis was to verify if the employment of quadratic registration yields to better performance results than those achieved by the algorithms when affine registration is used for image alignment. The hypothesis stated for this research question indicates that the results obtained with quadratic registration should indeed be better than the ones obtained using affine registration. The justification of this supposition comes from the fact that a motion model based on quadratic transformations is more flexible than one based on affine transformations. Such flexibility should represent an advantage for registering astronomical images, since the multiple distorting effects that diminish the quality of this sort of images also affect the accuracy achieved by any algorithm used to perform this task. Thus, since the usage of quadratic registration represents a more sophisticated way for dealing with these distortions, it is expected to obtain more precise results than those obtained by using affine registration.

In order to verify the validity of this hypothesis, the results obtained in the four cases that made up the 2EF were compared considering two pairs of cases, where each pair is conformed by the two cases where the same simulation tool but different registration procedures are employed. First, we computed the PSNR and (Reduced  $\chi^2 - 1$ ) ratios between the results obtained in cases 2 and 1 of the 2EF, which means that we compared the performances

achieved by affine and quadratic registration when PhoSim is employed for image simulation (see Figure 6.10). We computed the same ratios between cases 4 and 3 of the 2EF, which means that we compared the performances achieved by both registration procedures when the low-resolution images are obtained using the IOM (see Figure 6.11).

The curves obtained for the PSNR and the (Reduced  $\chi^2 - 1$ ) ratios present the same general behavior in both comparisons, where it can be observed that the values of these curves oscillate around 100% without any specific tendency and regardless of the SNR. This means that affine and quadratic registration achieve similar results regardless of the simulation scheme employed. Therefore, it can be concluded that the proposed hypothesis is not valid, since there is no evidence of the achievement of better results when quadratic registration is employed instead of affine registration.

## 7.5 Future research directions

The work presented in this thesis is mainly focused on studying how the performance of four multi-frame super-resolution algorithms is related to the SNR when astronomical images are considered. Since there are many parameters that affect the performance achieved by the algorithms and there are also many parameters that affect the quality of the astronomical images, the number of questions that can be made respect to the relations that exist between all these parameters is huge. Now we present some interesting examples of these questions that can be used as base for future research that would extend the conclusions presented in this work.

### 7.5.1 Testing new parameters

In this thesis, a fixed value was used through all the experiments for the FWHM of the PSF, the number of low-resolution images that made up each input set, and the downsampling factor used to generate the low-resolution images from the high-resolution template. Although the results obtained from experiments using such values provide a basis to draw conclusions and general guidelines about the behaviour of the four multi-frame super-resolution algorithms for astronomical images, this still poses a very limited approach.

The FWHM of the PSF corresponds to a crucial value when describing astronomical images. Using a fixed value for this element does not allow us to draw conclusions about how this parameter can affect the performance results obtained. A more general description of the performance of multi-frame super-resolution algorithms for astronomical images could be obtained by repeating the same experiments carried out in this thesis but over a range of values for the FWHM of the PSF. Besides, the modeling of this element in each simulation scheme is very different, thus we can expect to obtain different dependencies for the algorithms' performance as function of this parameter according to the simulation scheme employed.

It would also be interesting to see how the amount of low-resolution images contained on

each input set affects the outcome of the algorithms. A bigger number of images given as input could supply more information for the multi-frame super-resolution algorithms to use, allowing better results for the image reconstruction process. The same happens with the downsampling factor, since this number relates the resolution of the original high-resolution image with the resolution of the simulated low-resolution images. Thus, a variation on the downsampling factor will generate a variation on the amount of information contained in each one of the pixels of the simulated low-resolution images. This could also spawn changes on the results obtained for the reconstruction of the astronomical images.

### 7.5.2 ML vs MAP

The four algorithms presented and analyzed in this thesis were developed considering the Maximum a Posteriori (MAP) approach for the multi-frame super-resolution problem. Using regularization, this approach offers a mechanism to find a solution of this problem even though not enough low-resolution images are available. On the other hand, the Maximum Likelihood (ML) approach bases its operation on the exclusive utilization of the information contained in each low-resolution image contained in the input set. Because of this, when there is a lack of available low-resolution images, algorithms based in the ML approach are not useful to recover high-resolution images.

Therefore, it would be very interesting to analyze the performance achieved by MAP and ML algorithms considering input sets made up with different amounts of low-resolution images. The purpose of performing this experiment would be to find the critical number of images that is required in an input set to have a better performance of methods based in the ML approach than those based in the MAP approach.

### 7.5.3 Different registration methods

One of the conclusions presented in this thesis suggests that there is no significant difference in using quadratic or affine registration for aligning the set of low-resolution images. This conclusion is very limited since it is restricted to only two specific registration methods, and it does not provide any information for figuring out how the errors associated to the estimation of the registration parameters are related with the performance results achieved by the multi-frame super-resolution algorithms. In any case, to find such relation it is necessary to design new experiments, more sophisticated than those performed in this thesis.

However, the two registration methods considered are not the only ones existing and applicable in the context of astronomical images. This means that the results obtained in this thesis can be extended, in order to obtain more compelling conclusions, if the experiments are repeated including other registration algorithms.

Both registration methods used on this thesis are based on the minimization of the SSD between images. It would be interesting, for example, to consider registration methods based on the optimization of other similarity or dissimilarity measures, such as mutual information

or cross correlation. Only after accomplishing the same experiments of this thesis using more and different registration mechanisms, the real influence of this process over the performance of multi-frame super-resolution image reconstruction can be determined.

#### **7.5.4 Influence of optimization methods**

The implementation of each one of the four multi-frame super-resolution algorithms is based on the use of an optimization procedure. Although many different optimization techniques exist, the work presented on this thesis was restricted to using only the method known as non-linear conjugate gradient.

Different optimization methods could yield variations on the results obtained in the different experiments considered in this thesis. It would be interesting to analyze how the performance of the four multi-frame super-resolution algorithms changes when a different optimization procedure is used, since this could affect the algorithms' outcomes in terms of the accuracy of the results, but it could also affect performance in terms of the convergence time required for the reconstruction process. Besides, an optimization procedure is also required to perform image alignment with affine and quadratic registration, thus it would be also interesting to study how the performance of the two registration approaches is determined by the optimization method employed.

#### **7.5.5 Influence of interpolation methods**

The work developed in this thesis was not only restricted to the use of one optimization technique, the same can be said about the interpolation method employed. The optimization procedure by which image registration is performed, based on the minimization of the SSD, requires the utilization of multiple and successive interpolations in order to find the best values for the registration parameters.

In this thesis, the interpolation method used within the registration process was limited only to cubic spline. Nevertheless, many different interpolations methods exist and could be used in both registration procedures studied in this thesis. Just as the case with optimization methods mentioned above, performing the experiments carried out on this thesis considering different interpolation mechanisms could yield variations of the results, in terms of accuracy of the reconstructed high-resolution image and also in terms of the convergence time needed for estimating the registration parameters required by each one of the four multi-frame super-resolution algorithms.

# Appendix A

## Detailed results

In this appendix, all the results obtained for the four multi-frame super-resolution algorithms, LA, LZ, GA and GZ, are introduced. These results were obtained in the different experiments considered in the First Experimental Framework (1EF) and in the four cases that make up the Second Experimental Framework (2EF), and they were employed to generate all the plots displayed along the pages of this thesis. They are here presented in a series of tables where the average values obtained for the PSNR and the reduced  $\chi^2$ , along with their corresponding errors (standard deviation), are specified in different columns according to the range of SNR values considered in each experiment.

The details of the comparisons carried out between the performance results obtained in the 1EF and those obtained in each one of the four cases of the 2EF are also introduced. For each comparison one table is presented, where the PSNR and the (Reduced  $\chi^2 - 1$ ) ratios computed are presented as percentages for each one of the four algorithms considering each one of the values of the SNR range.

## A.1 Detailed results of the 1EF

Table A.1: Results of the 1EF considering the PSNR and the reduced  $\chi^2$  as performance metrics.

SNR	Algorithm	PSNR	PSNR error	Reduced $\chi^2$	Reduced $\chi^2$ error
1.0	LA	11.297	5.147	1.570	0.015
	LZ	14.374	4.623	1.589	0.016
	GA	3.411	5.381	1.553	0.015
	GZ	11.089	4.802	1.588	0.016
2.15	LA	17.600	4.591	1.574	0.014
	LZ	19.778	3.870	1.593	0.014
	GA	10.352	5.378	1.556	0.014
	GZ	16.536	4.672	1.591	0.014
4.64	LA	22.342	3.478	1.577	0.016
	LZ	23.618	2.998	1.598	0.018
	GA	16.096	4.861	1.558	0.014
	GZ	21.381	3.632	1.595	0.014
10.0	LA	26.152	2.879	1.583	0.037
	LZ	26.412	2.914	1.609	0.045
	GA	21.939	4.216	1.554	0.016
	GZ	24.894	3.221	1.598	0.022
21.54	LA	28.342	3.254	1.623	0.133
	LZ	28.080	3.331	1.659	0.159
	GA	26.689	3.533	1.554	0.014
	GZ	27.876	3.334	1.605	0.023
46.42	LA	29.136	3.619	1.786	0.334
	LZ	28.796	3.530	1.847	0.385
	GA	30.129	3.906	1.565	0.021
	GZ	29.457	3.623	1.642	0.064
100.0	LA	29.442	3.625	2.458	1.702
	LZ	29.139	3.542	3.297	2.061
	GA	32.109	4.469	1.593	0.080
	GZ	30.749	3.989	1.692	0.125

## A.2 Detailed results of the 2EF

### A.2.1 Case 1: PhoSim and affine registration

Table A.2: Results of the 2EF considering the PSNR and the reduced  $\chi^2$  as performance metrics, for the case 1 where simulations were obtained using PhoSim and affine registration was employed.

SNR	Algorithm	PSNR	PSNR Error	Reduced $\chi^2$	Reduced $\chi^2$ Error
1.43	LA	5.475	2.439	2.259	0.016
	LZ	7.421	2.191	2.234	0.017
	GA	1.793	2.573	2.116	0.016
	GZ	5.497	2.248	2.131	0.017
2.68	LA	9.167	2.329	2.228	0.015
	LZ	10.558	1.957	2.267	0.015
	GA	5.199	2.682	2.104	0.015
	GZ	9.113	2.335	2.226	0.015
5.37	LA	13.036	1.856	2.154	0.017
	LZ	13.634	1.605	2.129	0.019
	GA	9.504	2.629	2.248	0.015
	GZ	12.606	1.930	2.317	0.015
10.32	LA	14.935	1.662	2.165	0.039
	LZ	15.549	1.652	2.220	0.048
	GA	13.595	2.410	2.136	0.017
	GZ	14.712	1.841	2.116	0.023
25.87	LA	17.542	1.976	2.266	0.142
	LZ	17.286	2.025	2.305	0.168
	GA	16.467	2.147	2.145	0.015
	GZ	18.042	2.017	2.344	0.025
52.12	LA	20.275	2.391	2.538	0.356
	LZ	20.465	2.343	2.751	0.407
	GA	20.704	2.604	2.142	0.023
	GZ	19.788	2.404	2.290	0.068
96.56	LA	21.044	2.418	3.086	1.807
	LZ	20.830	2.363	4.324	2.164
	GA	22.674	2.994	2.289	0.085
	GZ	22.024	2.692	2.343	0.131

## A.2.2 Case 2: IOM and affine registration

Table A.3: Results of the 2EF considering the PSNR and the reduced  $\chi^2$  as performance metrics, for the case 2 where simulations were obtained using the IOM and affine registration was employed.

SNR	Algorithm	PSNR	PSNR Error	Reduced $\chi^2$	Reduced $\chi^2$ Error
1.43	LA	6.012	2.460	2.011	0.016
	LZ	7.894	2.263	1.942	0.016
	GA	1.736	2.596	1.866	0.016
	GZ	6.132	2.306	1.941	0.016
2.68	LA	9.403	2.326	1.994	0.014
	LZ	10.435	1.976	2.051	0.014
	GA	5.269	2.754	1.970	0.015
	GZ	9.132	2.414	2.036	0.014
5.37	LA	13.559	1.944	1.855	0.016
	LZ	14.471	1.694	1.930	0.018
	GA	9.594	2.753	1.942	0.015
	GZ	12.575	2.045	1.883	0.014
10.32	LA	18.315	1.813	1.935	0.038
	LZ	18.200	1.812	1.954	0.046
	GA	14.948	2.641	1.900	0.016
	GZ	16.175	2.010	1.990	0.022
25.87	LA	20.983	2.199	1.949	0.137
	LZ	19.898	2.263	2.121	0.163
	GA	19.115	2.412	1.852	0.015
	GZ	20.925	2.271	2.025	0.024
52.12	LA	21.942	2.602	2.364	0.342
	LZ	20.786	2.526	2.496	0.400
	GA	23.020	2.781	1.930	0.022
	GZ	21.326	2.598	2.004	0.066
96.56	LA	23.204	2.641	3.004	1.751
	LZ	22.141	2.552	4.095	2.107
	GA	23.772	3.230	1.901	0.083
	GZ	23.269	2.889	2.235	0.128

### A.2.3 Case 3: Phosim and quadratic registration

Table A.4: Results of the 2EF considering the PSNR and the reduced  $\chi^2$  as performance metrics, for the case 3 where simulations were obtained using PhoSim and quadratic registration was employed.

SNR	Algorithm	PSNR	PSNR Error	Reduced $\chi^2$	Reduced $\chi^2$ Error
1.43	LA	5.852	2.438	2.061	0.016
	LZ	6.860	2.167	2.146	0.017
	GA	1.670	2.530	2.170	0.016
	GZ	5.761	2.249	2.220	0.017
2.68	LA	8.926	2.328	2.086	0.015
	LZ	10.287	1.956	2.190	0.014
	GA	5.606	2.664	2.132	0.015
	GZ	9.138	2.344	2.274	0.015
5.37	LA	12.652	1.859	2.069	0.017
	LZ	13.498	1.608	2.162	0.019
	GA	9.016	2.635	2.247	0.015
	GZ	11.960	1.962	2.186	0.015
10.32	LA	14.973	1.660	2.219	0.039
	LZ	16.525	1.685	2.276	0.047
	GA	13.196	2.437	2.226	0.017
	GZ	14.652	1.846	2.256	0.023
25.87	LA	17.266	1.967	2.301	0.141
	LZ	17.353	2.023	2.403	0.169
	GA	16.110	2.132	2.064	0.015
	GZ	18.276	2.043	2.147	0.025
52.12	LA	20.547	2.399	2.589	0.353
	LZ	20.006	2.325	2.869	0.406
	GA	21.449	2.578	2.181	0.022
	GZ	20.932	2.393	2.443	0.068
96.56	LA	20.740	2.422	3.296	1.790
	LZ	20.311	2.381	4.274	2.202
	GA	22.478	2.982	2.237	0.084
	GZ	21.666	2.681	2.361	0.131

## A.2.4 Case 4: IOM and quadratic registration

Table A.5: Results of the 2EF considering the PSNR and the reduced  $\chi^2$  as performance metrics, for the case 4 where simulations were obtained using the IOM and quadratic registration was employed.

SNR	Algorithm	PSNR	PSNR Error	Reduced $\chi^2$	Reduced $\chi^2$ Error
1.43	LA	5.911	2.525	1.895	0.016
	LZ	7.868	2.252	1.886	0.016
	GA	1.667	2.590	1.958	0.016
	GZ	5.544	2.332	2.006	0.016
2.68	LA	9.846	2.371	2.017	0.014
	LZ	9.976	1.992	1.911	0.014
	GA	5.630	2.753	1.857	0.015
	GZ	9.237	2.412	1.875	0.014
5.37	LA	13.295	1.952	1.982	0.016
	LZ	13.754	1.685	1.896	0.018
	GA	9.639	2.750	1.958	0.014
	GZ	12.843	2.062	1.923	0.014
10.32	LA	18.171	1.809	1.928	0.038
	LZ	17.834	1.839	2.028	0.046
	GA	14.292	2.643	1.990	0.016
	GZ	15.521	2.026	2.056	0.023
25.87	LA	19.703	2.213	2.113	0.138
	LZ	19.516	2.263	2.089	0.164
	GA	18.140	2.417	1.886	0.015
	GZ	19.844	2.276	2.051	0.024
52.12	LA	22.923	2.598	2.295	0.343
	LZ	22.139	2.525	2.480	0.394
	GA	22.853	2.809	1.851	0.022
	GZ	21.807	2.600	2.140	0.066
96.56	LA	23.129	2.616	2.736	1.760
	LZ	22.149	2.562	4.352	2.114
	GA	24.403	3.251	1.957	0.083
	GZ	23.284	2.890	2.180	0.128

## A.3 Detailed results of the comparison between both frameworks

### A.3.1 Comparison between the 1EF and case 1 of the 2EF

Table A.6: Results obtained from computing the ratio between the performances achieved by the algorithms in the 1EF and in case 1 of the 2EF. This ratio is presented as a percentage for the PSNR and the (Reduced  $\chi^2 - 1$ ).

SNR	Algorithm	PSNR Ratio (%)	(Reduced $\chi^2 - 1$ ) Ratio (%)
1.22	LA	48.464	220.878
	LZ	51.626	209.591
	GA	52.582	201.621
	GZ	49.570	192.320
2.42	LA	52.087	214.138
	LZ	53.385	213.612
	GA	50.215	198.430
	GZ	55.109	207.214
5.01	LA	58.348	199.839
	LZ	57.729	188.772
	GA	59.045	223.748
	GZ	58.959	221.443
10.16	LA	57.108	199.715
	LZ	58.873	200.184
	GA	61.965	205.206
	GZ	59.098	186.717
23.71	LA	61.894	203.308
	LZ	61.562	198.155
	GA	61.700	206.665
	GZ	64.722	222.147
49.27	LA	69.587	195.707
	LZ	71.069	206.624
	GA	68.716	202.193
	GZ	67.175	200.812
98.28	LA	71.477	143.112
	LZ	71.484	144.738
	GA	70.614	217.488
	GZ	71.624	193.978

### A.3.2 Comparison between the 1EF and case 2 of the 2EF

Table A.7: Results obtained from computing the ratio between the performances achieved by the algorithms in the 1EF and in case 2 of the 2EF. This ratio is presented as a percentage for the PSNR and the (Reduced  $\chi^2 - 1$ ).

SNR	Algorithm	PSNR Ratio (%)	(Reduced $\chi^2 - 1$ ) Ratio (%)
1.22	LA	53.218	177.228
	LZ	54.918	159.877
	GA	50.890	156.572
	GZ	55.298	160.013
2.42	LA	53.428	173.270
	LZ	52.764	177.165
	GA	50.899	174.507
	GZ	55.227	175.254
5.01	LA	60.686	148.144
	LZ	61.272	155.501
	GA	59.607	168.916
	GZ	58.814	148.428
10.16	LA	70.035	160.222
	LZ	68.910	156.643
	GA	68.132	162.546
	GZ	64.974	165.609
23.71	LA	74.037	152.463
	LZ	70.862	170.161
	GA	71.622	153.804
	GZ	75.066	169.422
49.27	LA	75.309	173.534
	LZ	72.182	176.495
	GA	76.402	164.563
	GZ	72.396	156.223
98.28	LA	78.812	137.479
	LZ	75.981	134.773
	GA	74.034	151.958
	GZ	75.673	178.396

### A.3.3 Comparison between the 1EF and case 3 of the 2EF

Table A.8: Results obtained from computing the ratio between the performances achieved by the algorithms in the 1EF and in case 3 of the 2EF. This ratio is presented as a percentage for the PSNR and the (Reduced  $\chi^2 - 1$ ).

SNR	Algorithm	PSNR Ratio (%)	(Reduced $\chi^2 - 1$ ) Ratio (%)
1.22	LA	51.799	186.042
	LZ	47.728	194.580
	GA	48.964	211.489
	GZ	51.952	207.488
2.42	LA	50.716	189.279
	LZ	52.012	200.499
	GA	54.148	203.516
	GZ	55.263	215.403
5.01	LA	56.629	185.253
	LZ	57.150	194.217
	GA	56.017	223.685
	GZ	55.935	199.409
10.16	LA	57.254	208.988
	LZ	62.565	209.440
	GA	60.148	221.366
	GZ	58.856	210.199
23.71	LA	60.919	208.976
	LZ	61.799	213.093
	GA	60.362	191.969
	GZ	65.560	189.616
49.27	LA	70.519	202.150
	LZ	69.473	220.499
	GA	71.189	209.009
	GZ	71.059	224.569
98.28	LA	70.445	157.520
	LZ	69.703	142.553
	GA	70.006	208.617
	GZ	70.461	196.548

### A.3.4 Comparison between the 1EF and case 4 of the 2EF

Table A.9: Results obtained from computing the ratio between the performances achieved by the algorithms in the 1EF and in case 4 of the 2EF. This ratio is presented as a percentage for the PSNR and the (Reduced  $\chi^2 - 1$ ).

SNR	Algorithm	PSNR Ratio (%)	(Reduced $\chi^2 - 1$ ) Ratio (%)
1.22	LA	52.323	157.028
	LZ	54.735	150.505
	GA	48.881	173.168
	GZ	49.993	171.061
2.42	LA	55.944	177.306
	LZ	50.441	153.467
	GA	54.381	154.049
	GZ	55.862	148.020
5.01	LA	59.505	170.064
	LZ	58.233	149.688
	GA	59.885	171.774
	GZ	60.068	155.152
10.16	LA	69.484	159.148
	LZ	67.522	168.757
	GA	65.141	178.877
	GZ	62.347	176.760
23.71	LA	69.518	178.839
	LZ	69.502	165.325
	GA	67.970	159.963
	GZ	71.186	173.826
49.27	LA	78.677	164.727
	LZ	76.882	174.589
	GA	75.850	150.689
	GZ	74.030	177.432
98.28	LA	78.557	119.093
	LZ	76.012	145.965
	GA	75.999	161.455
	GZ	75.724	170.435

# Bibliography

- [1] JE Baldwin, PJ Warner, and CD Mackay. The point spread function in lucky imaging and variations in seeing on short timescales. *Astronomy & Astrophysics*, 480(2):589–597, 2008.
- [2] S.P. Belekos, N.P. Galatsanos, and A.K. Katsaggelos. Maximum a Posteriori Video Super-Resolution Using a New Multichannel Image Prior. In *IEEE Transactions on Image Processing*, volume 19(6), pages 1451 – 1464, 2010.
- [3] K.P. Bennet and M.J. Embrechts. An optimization perspective on kernel partial least squares regression. In *Nato Science Series sub series III computer and systems sciences*, volume 190, pages 227 – 250, 2003.
- [4] E. Bertin. Automated Morphometry with SExtractor and PSFEx. In I. N. Evans, A. Accomazzi, D. J. Mink, and A. H. Rots, editors, *Astronomical Data Analysis Software and Systems XX*, volume 442 of *Astronomical Society of the Pacific Conference Series*, page 435, July 2011.
- [5] Emmanuel Bertin and S Arnouts. SExtractor: Software for source extraction. *Astronomy and Astrophysics Supplement Series*, 117(2):393–404, 1996.
- [6] Sean Borman and Robert L Stevenson. Super-resolution from image sequences-a review. In *mwsacas*, page 374. IEEE, 1998.
- [7] N.K. Bose, S.P. Kim, and H.M. Valenzuela. Recursive implementation of total least squares algorithm for image reconstruction from noisy, undersampled multiframes. In *Proceedings of the IEEE Conference on Acoustics, Speech and Signal Processing*, volume 5, pages 269 – 272, 1993.
- [8] N.K. Bose, S. Lertrattanapanich, and M.B. Chappalli. Superresolution with second generation wavelets. In *Signal Processing: Image Communication*, volume 19(5), pages 387 – 391, 2004.
- [9] Emmanuel J Candès and Carlos Fernandez-Granda. Towards a mathematical theory of super-resolution. *Communications on Pure and Applied Mathematics*, 67(6):906–956, 2014.
- [10] Tony F Chan, Stanley Osher, and Jianhong Shen. The digital tv filter and nonlinear

- denoising. *Image Processing, IEEE Transactions on*, 10(2):231–241, 2001.
- [11] G.K. Chantas, N.P. Galatsanos, and N.A. Woods. Super-Resolution Based on Fast Registration and Maximum a Posteriori Reconstruction. In *IEEE Transactions on Image Processing*, volume 16(7), pages 1821 – 1830, 2007.
- [12] P. Cheeseman, R. Kanefsky, R. Kraft, J. Stutz, and R. Hanson. Super-resolved surface reconstruction from multiple images. In *Maximum Entropy and Bayesian Methods*, pages 293 – 308, 1996.
- [13] M.G. Choi, Y. Yang, and N.P. Galatsanos. Multichannel regularized recovery of compressed video sequences. In *IEEE Trans. Circuits Syst. II: Analog and Digital Signal Processing*, volume 48(4), pages 376 – 387, 2001.
- [14] Chao Dong, Chen Change Loy, Kaiming He, and Xiaoou Tang. Learning a deep convolutional network for image super-resolution. In *Computer Vision–ECCV 2014*, pages 184–199. Springer, 2014.
- [15] Weisheng Dong, Lei Zhang, Guangming Shi, and Xiaolin Wu. Image deblurring and super-resolution by adaptive sparse domain selection and adaptive regularization. *Image Processing, IEEE Transactions on*, 20(7):1838–1857, 2011.
- [16] D.L. Donoho. De-noising by soft thresholding. In *IEEE Trans. Information Theory*, volume 41, pages 613 – 627, 1995.
- [17] Daniel J Eisenstein, David H Weinberg, Eric Agol, Hiroaki Aihara, Carlos Allende Prieto, Scott F Anderson, James A Arns, Éric Aubourg, Stephen Bailey, Eduardo Balbinot, et al. Sdss-iii: Massive spectroscopic surveys of the distant universe, the milky way, and extra-solar planetary systems. *The Astronomical Journal*, 142(3):72, 2011.
- [18] M. Elad and A. Feuer. Restoration of a single superresolution image from several blurred, noisy, and undersampled measured images. In *Image Processing*, volume 6(12), pages 1646 – 1658, 1997.
- [19] M. Elad and A. Feuer. Super-resolution reconstruction of continuous image sequences. In *ICIP*, pages 817 – 834, 1999.
- [20] M. Elad and A. Hel-Or. A fast super-resolution reconstruction algorithm for pure translational motion and common space invariant blur. In *IEEE Transactions on Image Processing*, volume 10(8), pages 1187 – 1193, 2001.
- [21] P.E. Eren, M.I. Sezan, and M. Tekalp. Robust, object-based high- resolution image reconstruction from low-resolution video. In *IEEE Transactions on Image Processing*, volume 6(10), pages 1446 – 1451, 1997.
- [22] Sina Farsiu, M Dirk Robinson, Michael Elad, and Peyman Milanfar. Fast and robust multiframe super resolution. *Image processing, IEEE Transactions on*, 13(10):1327–1344, 2004.

- [23] Andrew Fruchter and Richard N Hook. Novel image-reconstruction method applied to deep hubble space telescope images. In *Optical Science, Engineering and Instrumentation'97*, pages 120–125. International Society for Optics and Photonics, 1997.
- [24] Vincent Garrel, Olivier Guyon, and Pierre Baudoz. A highly efficient lucky imaging algorithm: Image synthesis based on fourier amplitude selection. *Publications of the Astronomical Society of the Pacific*, 124(918):861–867, 2012.
- [25] Daniel Glasner, Shai Bagon, and Michal Irani. Super-resolution from a single image. In *Computer Vision, 2009 IEEE 12th International Conference on*, pages 349–356. IEEE, 2009.
- [26] A Ardeshir Goshtasby. *2-D and 3-D image registration: for medical, remote sensing, and industrial applications*. John Wiley & Sons, 2005.
- [27] F. Guichard and L. Rudin. Image frame fusion by velocity estimation using region merging. In *US Patent 5,909,251*, 1997.
- [28] Russell C Hardie, Kenneth J Barnard, and Ernest E Armstrong. Joint map registration and high-resolution image estimation using a sequence of undersampled images. *Image Processing, IEEE Transactions on*, 6(12):1621–1633, 1997.
- [29] Derek LG Hill, Philipp G Batchelor, Mark Holden, and David J Hawkes. Medical image registration. *Physics in medicine and biology*, 46(3):R1, 2001.
- [30] Bo Huang, Hazen Babcock, and Xiaowei Zhuang. Breaking the diffraction barrier: super-resolution imaging of cells. *Cell*, 143(7):1047–1058, 2010.
- [31] M. Irani and S. Peleg. Super resolution from image sequences. In *Proceedings of the International Conference on Pattern Recognition*, volume 2, pages 115 – 120, 1990.
- [32] M. Irani and S. Peleg. Improving resolution by image registration. In *Graphical Models and Image Processing*, volume 53, pages 231 – 239, 1991.
- [33] M. Irani and S. Peleg. Motion analysis for image enhancement: resolution, occlusion, and transparency. In *Journal of Visual Communication and Image Representation*, volume 4, pages 324 – 335, 1993.
- [34] M. Islam, N. Islam, V.K. Asari, and M.A. Karim. Single image super-resolution in frequency domain. In *IEEE Southwest Symposium on Image Analysis and Interpretation*, pages 53 – 56, 2012.
- [35] Zeljko Ivezic, JA Tyson, B Abel, E Acosta, R Allsman, Y AlSayyad, SF Anderson, J Andrew, R Angel, G Angeli, et al. Lsst: from science drivers to reference design and anticipated data products. *arXiv preprint arXiv:0805.2366*, 2008.
- [36] CV Jiji, Manjunath V Joshi, and Subhasis Chaudhuri. Single-frame image super-resolution using learned wavelet coefficients. *International journal of Imaging systems and Technology*, 14(3):105–112, 2004.

- [37] Manjunath V Joshi, Subhasis Chaudhuri, and Rajkiran Panuganti. A learning-based method for image super-resolution from zoomed observations. *IEEE Transactions on Systems, Man, and Cybernetics Part B: Cybernetics*, 35(3):527–537, 2005.
- [38] J.P. Kahane. Variations on a theorem of Candès, Romberg and Tao. In *A paraître aux Annales de l’Institut Fourier en 2013*, 2013.
- [39] D. Keren, S. Peleg, and R. Brada. Image sequence enhancement using subpixel displacements. In *IEEE Conference on Computer Vision and Pattern Recognition*, pages 742 – 746, 1988.
- [40] S.P. Kim, N.K. Bose, and H.M. Valenzuela. Recursive reconstruction of high resolution image from noisy undersampled multiframe. In *IEEE Transactions on Acoustics, Speech and Signal Processing*, volume 38(6), pages 1013 – 1027, 1990.
- [41] Dilip Krishnan and Rob Fergus. Fast image deconvolution using hyper-laplacian priors. In *Advances in Neural Information Processing Systems*, pages 1033–1041, 2009.
- [42] Jacqueline Le Moigne, William J Campbell, and Robert F Crompt. An automated parallel image registration technique based on the correlation of wavelet features. *Geoscience and Remote Sensing, IEEE Transactions on*, 40(8):1849–1864, 2002.
- [43] T. Lukes, P. Krizek, Z. Svindrych, J. Benda, M. Ovesny, K. Fliegel, M. Klima, and G.M. Hagen. Three-dimensional super-resolution structured illumination microscopy with maximum a posteriori probability image estimation. In *Optics Express*, volume 22(24), pages 29805 – 29817, 2014.
- [44] Maria Teresa Merino and Jorge Nunez. Super-resolution of remotely sensed images with variable-pixel linear reconstruction. *Geoscience and Remote Sensing, IEEE Transactions on*, 45(5):1446–1457, 2007.
- [45] N. Nguyen, P. Milanfar, and G. Golub. Efficient generalized cross-validation with applications to parametric image restoration and resolution enhancement. In *IEEE Transactions on Image Processing*, volume 10(9), pages 1299 – 1308, 2001.
- [46] Nhat Nguyen, Peyman Milanfar, and Gene Golub. A computationally efficient super-resolution image reconstruction algorithm. *Image Processing, IEEE Transactions on*, 10(4):573–583, 2001.
- [47] S.S. Panda, M.R. Prasad, and G. Jena. POCS Based Super-Resolution Image Reconstruction Using an Adaptive Regularization Parameter. In *IJCSI International Journal of Computer Science*, volume 8(5), pages 155 – 158, 2011.
- [48] Sung Cheol Park, Min Kyu Park, and Moon Gi Kang. Super-resolution image reconstruction: a technical overview. *Signal Processing Magazine, IEEE*, 20(3):21–36, 2003.
- [49] A.J. Patti and Y. Altunbasak. Artifact reduction for set theoretic super resolution image reconstruction with edge adaptive constraints and higherorder interpolants. In *IEEE Transactions on Image Processing*, volume 10(1), pages 179 – 186, 2001.

- [50] A.J. Patti, M.I. Sezan, and A.M. Tekalp. Robust methods for high quality stills from interlaced video in the presence of dominant motion. In *IEEE Transactions on Circuits and Systems for Video Technology*, volume 7(2), pages 328 – 342, 1997.
- [51] A.J. Patti, M.I. Sezan, and A.M. Tekalp. Super resolution video reconstruction with arbitrary sampling lattices and nonzero aperture time. In *IEEE Transactions on Image Processing*, pages 1064 – 1078, 1997.
- [52] S. Peleg, D. Keren, and L. Schweitzer. Improving image resolution using subpixel motion. In *Pattern Recognition Letters*, volume 5(3), pages 223 – 226, 1987.
- [53] J. R. Peterson, J. G. Jernigan, S. M. Kahn, A. P. Rasmussen, E. Peng, Z. Ahmad, J. Bankert, C. Chang, C. Claver, D. K. Gilmore, E. Grace, M. Hannel, M. Hodge, S. Lorenz, A. Lupu, A. Meert, S. Nagarajan, N. Todd, A. Winans, and M. Young. Simulation of astronomical images from optical survey telescopes using a comprehensive photon monte carlo approach. *The Astrophysical Journal Supplement Series*, 218(1):14, 2015.
- [54] Michael JD Powell. An efficient method for finding the minimum of a function of several variables without calculating derivatives. *The computer journal*, 7(2):155–162, 1964.
- [55] AN Rajagopalan and Subhasis Chaudhuri. A variational approach to recovering depth from defocused images. *Pattern Analysis and Machine Intelligence, IEEE Transactions on*, 19(10):1158–1164, 1997.
- [56] L. Rudin and F. Guichard. Velocity estimation from images sequence and application to super-resolution. In *Proceedings of the IEEE International Conference on Image Processing*, volume 3, pages 527 – 531, 1999.
- [57] Leonid I Rudin, Stanley Osher, and Emad Fatemi. Nonlinear total variation based noise removal algorithms. *Physica D: Nonlinear Phenomena*, 60(1):259–268, 1992.
- [58] Richard R Schultz and Robert L Stevenson. Extraction of high-resolution frames from video sequences. *Image Processing, IEEE Transactions on*, 5(6):996–1011, 1996.
- [59] W. Shen, L. Fang, X. Chen, and H. Xu. Projection onto Convex Sets Method in Space frequency Domain for Super Resolution. In *Journal of Computers*, volume 9(8), pages 1959 – 1966, 2014.
- [60] Andrew Smith, Jeremy Bailey, JH Hough, and Steven Lee. An investigation of lucky imaging techniques. *Monthly Notices of the Royal Astronomical Society*, 398(4):2069–2073, 2009.
- [61] H. Stark and P. Oskoui. High resolution image recovery from image-plane arrays, using convex projections. In *J. Opt. Soc. Am. A.*, volume 6(11), pages 1715 – 1726, 1989.
- [62] Jian Sun, Jian Sun, Zongben Xu, and Heung-Yeung Shum. Image super-resolution using gradient profile prior. In *Computer Vision and Pattern Recognition, 2008. CVPR 2008. IEEE Conference on*, pages 1–8. IEEE, 2008.

- [63] Will Sutherland, Jim Emerson, Gavin Dalton, Eli Atad-Ettinger, Steven Beard, Richard Bennett, Naidu Bezawada, Andrew Born, Martin Caldwell, Paul Clark, et al. The visible and infrared survey telescope for astronomy (vista): Design, technical overview, and performance. *Astronomy & Astrophysics*, 575:A25, 2015.
- [64] H. Takeda, S. Farsiu, J. Christou, and P. Milanfar. Super-Drizzle: Applications of Adaptive Kernel Regression in Astronomical Imaging. In *The Advanced Maui Optical and Space Surveillance Technologies Conference*, page 27, 2006.
- [65] A.N. Tikhonov and V.A. Arsenin. *Solution of ill-posed problems*. Winston & Sons, Washington, 1997.
- [66] M.E. Tipping and C.M. Bishop. Bayesian image super-resolution. In *Advances in Neural Information Processing Systems*, volume 15, pages 1279 – 1286, 2003.
- [67] Doug Tody. The iraf data reduction and analysis system. In *1986 Astronomy Conferences*, pages 733–748. International Society for Optics and Photonics, 1986.
- [68] Doug Tody. Iraf in the nineties. In *Astronomical Data Analysis Software and Systems II*, volume 52, page 173, 1993.
- [69] B.C. Tom and A.K. Katsaggelos. Reconstruction of a high-resolution image by simultaneous registration, restoration, and interpolation of low-resolution images. In *Proceedings of the IEEE International Conference on Image Processing*, pages 2539 – 2542, 1995.
- [70] B.C. Tom, A.K. Katsaggelos, and N.P. Galatsanos. Reconstruction of a high resolution image from registration and restoration of low resolution images. In *Proceedings of the IEEE International Conference on Image Processing*, pages 553 – 557, 1994.
- [71] RY Tsai and Thomas S Huang. Multiframe image restoration and registration. *Advances in computer vision and Image Processing*, 1(2):317–339, 1984.
- [72] H. Ur and D. Gross. Improved resolution from sub-pixel shifted pictures. In *Graphical Models and Image Processing*, volume 52, pages 181 – 186, 1992.
- [73] Patrick Vandewalle, Sabine Süsstrunk, and Martin Vetterli. A frequency domain approach to registration of aliased images with application to super-resolution. *EURASIP Journal on applied signal processing*, 2006:233–233, 2006.
- [74] N.A. Woods, N.P. Galatsanos, and A.K. Katsaggelos. Em-based simultaneous registration, restoration, and interpolation of super-resolved images. In *Proceedings of the IEEE International Conference on Image Processing*, 2003.
- [75] Nathan Woods, Nikolas P Galatsanos, Aggelos K Katsaggelos, et al. Stochastic methods for joint registration, restoration, and interpolation of multiple undersampled images. *Image Processing, IEEE Transactions on*, 15(1):201–213, 2006.
- [76] Wei Wu, Zheng Liu, and Xiaohai He. Learning-based super resolution using kernel partial least squares. *Image and Vision Computing*, 29(6):394–406, 2011.

- [77] A.Y. Yang, S.S. Sastry, A. Ganesh, and M. Yi. Fast  $\ell_1$ -minimization algorithms and an application in robust face recognition: A review. In *17th IEEE International Conference on Image Processing (ICIP)*, pages 1849 – 1852, 2010.
- [78] Jianchao Yang, Zhaowen Wang, Zhe Lin, Scott Cohen, and Tingwen Huang. Coupled dictionary training for image super-resolution. *Image Processing, IEEE Transactions on*, 21(8):3467–3478, 2012.
- [79] Jianchao Yang, John Wright, Thomas Huang, and Yi Ma. Image super-resolution as sparse representation of raw image patches. In *Computer Vision and Pattern Recognition, 2008. CVPR 2008. IEEE Conference on*, pages 1–8. IEEE, 2008.
- [80] Jianchao Yang, John Wright, Thomas S Huang, and Yi Ma. Image super-resolution via sparse representation. *Image Processing, IEEE Transactions on*, 19(11):2861–2873, 2010.
- [81] Yoshiaki Yasuno, Jun-ichiro Sugisaka, Yusuke Sando, Yoshifumi Nakamura, Shuichi Makita, Masahide Itoh, and Toyohiko Yatagai. Non-iterative numerical method for laterally superresolving fourier domain optical coherence tomography. *Optics express*, 14(3):1006–1020, 2006.
- [82] Barbara Zitova and Jan Flusser. Image registration methods: a survey. *Image and vision computing*, 21(11):977–1000, 2003.
- [83] Assaf Zomet and Shmuel Peleg. Efficient super-resolution and applications to mosaics. In *Pattern Recognition, 2000. Proceedings. 15th International Conference on*, volume 1, pages 579–583. IEEE, 2000.
- [84] Assaf Zomet, Alex Rav-Acha, and Shmuel Peleg. Robust super-resolution. In *Computer Vision and Pattern Recognition, 2001. CVPR 2001. Proceedings of the 2001 IEEE Computer Society Conference on*, volume 1, pages I–645. IEEE, 2001.